A COLLOIDAL APPROACH TO EYE LENS PROTEIN MIXTURES: RELEVANCE FOR CATARACT FORMATION

THÈSE N^{O} 4375 (2009)

PRÉSENTÉE LE 15 MAI 2009
À LA FACULTE SCIENCES DE BASE
IRRMA
PROGRAMME DOCTORAL EN PHYSIQUE

ÉCOLE POLYTECHNIQUE FÉDÉRALE DE LAUSANNE

POUR L'OBTENTION DU GRADE DE DOCTEUR ÈS SCIENCES

PAR

Nicolas DORSAZ

acceptée sur proposition du jury:

Prof. G. Gremaud, président du jury
Prof. A. Baldereschi, Prof. G. Foffi, directeurs de thèse
Prof. K. Dawson, rapporteur
Prof. G. Dietler, rapporteur
Prof. G. Franzese, rapporteur

ÉCOLE POLYTECHNIQUE
FÉDÉRALE DE LAUSANNE
Suisse
2009

Abstract

A broad and constantly growing class of diseases, such as Alzheimer's disease, sickle-cell or cataract, involve protein association phenomena as an essential aspect. The common denominator of all the members of this class of `molecular condensation diseases` is an attractive energy of interaction between specific biologic molecules which produces condensation into dense, frequently insoluble mesoscopic phases. Understanding interprotein interactions is essential since it is the subtle interplay between interprotein attraction, repulsion and solution entropy that leads to the condensed protein phases. Among these diseases, cataract is the world's leading cause of blindness and effective prevention or non-surgical cure are still lacking. The loss of transparency of the eye lens found in cataract originates from the alteration of the spatial distribution of the lens `crystallin` proteins. Biological studies of the chaperone properties of crystallins have given valuable information about their aggregation in diluted environment. However, since the crystallins are present at high concentration in the eye lens cells, it is crucial to complement these studies with investigations at physiological concentrations where emergent mixture properties, like phase transitions, are expected.

The eye lens cytoplasm contains a solution of mainly three classes of water soluble proteins, called $\alpha-$, $\beta-$ and $\gamma-$crystallin. In this thesis we develop a coarse-grained model for binary mixtures of α- and γ-crystallin proteins. By analyzing our numerical results in conjunction with experimental neutron scattering data, the interactions between the proteins are modeled. We demonstrate that transparency of the eye lens is greatly enhanced by a weak, short-range attraction between α and γ-crystallin. Provided it is not too strong, such mutual attraction considerably decreases the critical temperature and the corresponding opacity due to light scattering, and it is consequently essential for eye lens transparency.

The phase diagram of the binary α-γ model mixture is then investigated via thermodynamic perturbation theory. The instability boundary of the crystallin mixtures is found to depend on the α-γ attraction in a manner that is both extremely sensitive and non-monotonic, in excellent agreement with the experimental and numerical results. Moreover, the composition of the coexisting phases depends strongly on the strength of the α-γ interaction. In light of the tie lines determination it appears that a decrease of the binding affinity of α and γ-crystallins with ageing involves small energy changes in the attraction between the crystallins and can produce sufficient inhomogeneities to lead to the opacification of the lens.

The colloidal approach developed in this thesis could be applied in the future to study other mixtures of crystallin proteins and provide new insights into their interactions and thermodynamic stability when combined with scattering experiments and cloud point measurements.

Keywords:

Phase transitions, thermodynamics, binary mixtures, crystallin proteins, soft condensed matter, molecular dynamics, coarse-grained models, colloidal systems, proteins condensation.

Résumé

Une importante classe de maladies, telles que la maladie d'Alzheimer, l'anémie à hématies falciformes ou la cataracte, sont liées à des phénomènes d'associations de protéines. Le dénominateur commun de ces maladies de `condensation moléculaire` est la présence d'une énergie d'interaction attractive entre certaines molécules biologiques qui produit une condensation en phases mésoscopiques denses et souvent insolubles. La compréhension des interactions entre les protéines est essentielle puisque c'est le jeu subtil entre attraction, répulsion et entropie qui conduit à ces phases condensées. Parmi ces maladies, la cataracte est la principale cause de cécité dans le monde et sa prévention ainsi que son traitement non chirurgical font encore défaut. La perte de transparence du cristallin est due à l'altération de la distribution spatiale des protéines cristallines. L'étude des propriétés de chaperones des cristallines a fourni de précieuses informations sur leur agrégation en milieu dilué. Cependant, puisque les protéines cristallines sont présentes à haute concentration dans les cellules du cristallin, il est crucial de compléter ces études par des investigations en conditions physiologiques où l'on peut s'attendre à l'apparition de propriétés nouvelles telles que des transitions de phase.

Le cristallin est constitué d'une solution de trois classes de protéines solubles appelées cristalline α, β et γ. Dans ce travail nous avons développé un modèle à `grain grossier` (*coarse-grained*) de mélanges binaires de protéines cristallines α et γ en combinant des simulations de dynamique moléculaire et des résultats de diffusion de neutrons à petit angle. Nous avons montré que la transparence de la solution est augmentée si on introduit une faible attraction à courte portée entre les cristallines α et γ. Si cette attraction mutuelle n'est pas trop grande, elle abaisse la température critique et l'opacité due à la diffusion de la lumière et est donc essentielle pour la transparence du cristallin.

Nous avons étudié le diagramme de phase de solutions binaires α-γ dans le cadre d'une théorie thermodynamique de perturbation. Les limites de stabilité des solutions cristallines apparaissent dépendre de l'attraction entre les α et les γ d'une manière très sensible et non monotone, en excellent accord avec les résultats numériques et expérimentaux. De plus, la composition des phases coexistantes dépend fortement de l'intensité de l'interaction α-γ. La détermination des `tie-lines` montre qu'une diminution de l'affinité de liaison entre les α et les γ due au vieillissement implique de faibles changements de l'énergie d'interaction entre les cristallines et peut produire des inhomogénéités suffisantes pour provoquer une opacification du cristallin.

L'approche colloïdale développée dans ce travail pourrait être appliquée à l'avenir à l'étude d'autres solutions de protéines cristallines et aider à la compréhension de leurs interactions et de leur stabilité thermodynamique, en la combinant aux résultats d'expériences de diffusion et aux mesures de `cloud point`.

Mots-Clés

Transitions de phase, thermodynamique, solutions binaires, protéines crystallines, physique de la matière molle, dynamique moléculaire, modèles *coarse-grained*, systèmes colloidaux, agrégation de protéines.

Contents

Abstract i

Résumé iii

1 Introduction 1

1.1 Eye lens and transparency 2

1.1.1 α crystallin and cataract as a protein folding disease 4

1.1.2 γ crystallin and cold cataract 6

2 Colloidal model for eye lens protein mixtures 9

2.1 Introduction 10

2.2 Eye lens crystallin proteins 11

2.3 Experiments 14

2.4 Simulations and model validation 16

2.4.1 Model 16

2.4.2 Simulations 17
2.4.3 Derivation of the model 21
2.4.4 Structural properties 34
2.4.5 Mixture stability tuning the α-γ attraction 40
2.5 Conclusions 42

3 Phase behaviour of binary mixtures **45**
3.1 Introduction 46
3.2 Thermodynamic perturbation theory 48
3.2.1 Perturbation theory and the λ expansion 50
3.2.2 Stability criteria: the spinodal 54
3.2.3 Main fluctuations driving the instability 58
3.2.4 Phase coexistence: the binodal 59
3.3 The symmetric binary mixtures 61
3.3.1 Model 63
3.3.2 Phase behaviour at x = 1/2 64
3.3.3 Phase behaviour in the $x-\rho$ plane 70
3.3.4 Asymmetric binary mixtures with $d_1 \neq d_2$ 75
3.4 Conclusions 81

4 Phase behaviour of the binary α-γ mixture of eye lens proteins **83**
4.1 Introduction 84
4.2 Spinodal surface 85
4.2.1 3D spinodal surfaces 86
4.2.2 Spinodals on the experimental plane 90
4.3 Coexistence surfaces and tie-lines 95
4.4 Conclusions 111

5 Conclusions 113

Appendix A: Resolution function 117

Appendix B: Partial radial distribution function of hard spheres 121

List of Figures 127

Bibliography 137

Acknowledgements 153

Curriculum Vitae 155

CHAPTER 1

Introduction

Cataract is the leading cause of blindness and among its different forms, age-related cataract is responsible for 48% of blindness worldwide [WHO, 2007]. Despite considerable efforts, effective prevention of cataract development or non surgical cures are still lacking [D. Pitts et al., 1986]. Cataract is a loss of visual acuity and of contrast sensitivity due to the opacification of the crystallin lens of the eye. It has been shown that the fraction of the incident light that is back scattered by the crystallin lens increases exponentially with age [Benedek, 1997; Thurston et al., 1997]. Thus, cataractogenesis is a continual process of opacification that starts already at birth and in which the fraction of the light scattered by the lens continuously increases with ageing until clinically distinguishable opacification can be detected. The exponential time constant ΔT is believed to differ from one subject to another but, by the age of 80, the percentage of the population requiring a cataract treatment is around 60% [Ferris and Tielsch, 2004].

The process that causes cataract seems therefore natural and unavoidable. However, in the last decades, researchers have started to uncover the molecular basis for both transparency and opacification [Benedek, 1971], and strategies to inhibit cataract or, equivalently, to slow down the rate of progression of turbidity have emerged [Benedek, 1997].

1.1 Eye lens and transparency

The eye is the organ of vision and the light is conveyed from the outside to the retina. The retina senses the light and creates impulses that transit through the optic nerve to the brain where they are processed. The role of the eye lens consists in focussing the light on the retina. The lens has a complex architecture and a unique protein composition that ensure its transparency. It is composed of elongated concentric shells made of fibre cells that can be up to 10 mm long in human [Bloemendal et al., 2004]. The shape of these long cells is maintained by an extensive cytoskeleton. The concentration of proteins is unusually high in the fibre cells with an important gradient of concentration (from 200 mg/ml in the outer shells up to 500 mg/ml in the nucleus). The abundant water-soluble proteins of the eye lens are known as crystallins and account for most of the fibre cell proteins. All mammalian lenses contain three families of crystallins proteins named α-, β- and γ-crystallins, following their decreasing molecular weight and increasing isoelectric point.

Crystallins synthesized during the early stages of development are located in the nucleus of the mature lens, while the outer cortex is rich in crystallins expressed later on. As a last step in their differentiation process, the fibre cells lose their cellular organelles (mitochondria, ribosomes and nuclei) [Bassnett, 2008] so that they can no longer synthesize or degrade proteins. Thus, the cell composition at the center of the lens is already definitive after foetal development, and the crystallin proteins cannot be replaced. The last step of differentiation is essential to provide an homogeneous environment that ensures lens transparency. The mature lens is thus like a very dense *jellylike* bag of crystallins proteins [Benedek, 1997]. As the main function of the eye lens is to focus the light on the retina, transparency and high refractive index are essential characteristics. It is therefore important to understand how transparency in a dense medium like the lens can be achieved.

Maurice, in his pioneering study of the corneal stroma, came to the conclusion that transparency can be explained by the phase correlation of the waves scattered by the different fibers [Maurice, 1957]. Indeed, if the fibers were acting independently, the cornea would scatter more than 90% of the incident light. The most striking example of phase correlation is given by X-ray or light diffraction from perfectly regular lattices in solid state physics. A perfect lattice scatters the light only in few directions corresponding to Bragg reflections. Thus the arrangement of the fibers in a regular array was thought to be essential for the transparency of any tissue. However, experiments on the shark cornea revealed, a decade later, that the collagen fibres exhibit a totally disordered arrangement [Goldman and Benedek, 1967]. So even in this case, the phase correlation seems to reduce the light scattered by the fibres. Indeed, Benedek and Goldman showed that the fibers in both human and shark stroma are separated by small distances compared to the light wavelength, ensuring an important correlation between the phases of the waves scattered by neighbouring fibers. The scattering is thus reduced and the stroma is transparent. However, when fluctuations of the refractive index, due to irregularities in the density of the collagen fibers, emerge on lengthscale comparable or larger than the light wavelength, the cornea stroma becomes opaque.

This *theory of transparency* [Benedek, 1971] was then applied to the eye lens to understand the conditions of transparency and to relate microscopic alterations in the structure of the lens to its opacification. Disruption of the local homogeneity in the eye lens can be produced by the aggregation of the lens proteins into high molecular weight clusters. This induces sufficient fluctuations to increase the turbidity and cause cataract, the turbidity of the lens being directly proportional to the molecular weight of the aggregates [Benedek, 1971]. Indeed, experimental studies confirmed the presence of high molecular weight aggregates in aging lenses [Spector et al., 1971]. Therefore, in order to understand cataract formation, it is essential to investigate the biological function of the protein content of the lens and to search for possible chemical modifications of these proteins that could lead to their uncontrolled aggregation. In this context, the biological properties of a first family of proteins, the α-crystallins, attracted considerable attention in the following decades.

1.1.1 α crystallin and cataract as a protein folding disease

The α crystallins are polydisperse oligomers, comprising more than 40 subunits with a molecular weight between 800 and 900 kDa. They are large, almost spherical and non-compact acidic proteins. They are continuously synthesized during lens development and homogeneously distributed throughout the lens. They account for up to 40% of the soluble lens proteins [Bloemendal et al., 2004]. To date, the structure of the α-crystallin is still unknown. These proteins are highly polydispersed (20%) since they result from the assembly of α-A and α-B proteins and the arrangement of these smaller subunits is different for every α. This tendency to form polydispersed assembly is probably responsible for the difficulty to crystallize them. Because of the lack of knowledge of the exact structure of the αs, the model for α-crystallins has been continuously modified to incorporate new experimental results. Given the large size and molecular weight of αs, it was thought first that they were solely lens-specific proteins which deserves the structural stability of the lens. However, the subunits of this proteins were then found in other organs as well.

Experiments on the binding of hydrophobic reactants have revealed that an area of hydrophobicity is present in the α-crystallin, allowing these proteins to bind to unfolded proteins. It was in particular shown that a denatured γ can bind to the center of a multi-subunit α [Boyle et al., 1993]. Moreover, the α subunits were shown to belong to the family of heat shocks proteins (HSPs) [Bloemendal et al., 2004]. HSPs are a group of stress proteins that are synthesized to protect the cell against stress induced damages, like heat, oxydation or contact with toxic compounds. Sometimes HSPs can also work as *chaperones* and bind to other proteins to stabilize them when they are at intermediate stages of folding, assembling or degradation. Chaperones can also transport damaged proteins within the cell towards areas where they won't interfere with its normal functioning. The chaperone activity of the α crystallin is believed to be essential for the function of the lens. Indeed, it has been found that the α prevent thermal aggregation of β and γ crystallins and of several other enzymes [Liang and Li, 1991]. Moreover α crystallins can bind to unfolded γ and stabilize them against important stresses, like for instance UV light which can damage lens proteins.

The recognized HSP and chaperone characters of α crystallins are at the origin of viewing cataract formation as a protein folding disease occurring when non native proteins accumulate faster than the rate at which chaperones can prevent their aggregation [Csermely, 2001]. The mature lens starts with a high concentration of chaperone α crystallins and can face, in a first time, the unfolding of other proteins, like for instance the γs [Horwitz, 1992]. However, because of the impossibility for the mature cells to synthesize new proteins, the chaperone capability of the cell cannot be increased when, with aging, more an more non native proteins unfold and aggregate. Thus, the absence of cellular organelles in the mature lens, which is essential for its transparency in the early age of the lens, is very likely also responsible for the aggregation of the crystallins on longer terms, when the cell has used all of its chaperone capability.

Beside the α-crystallins, there is another family of eye lens proteins, the γ-crystallins, that could play a role in cataract formation.

1.1.2 γ crystallin and cold cataract

The γ-crystallins are small monomeric proteins, with a molecular weight of about 21 kDa. In contrast to the α-crystallins, the γs have been crystallized and their structure has been resolved [Blundell et al., 1981; Najmudin et al., 1993; Bettelheim et al., 1999; Kumaraswamy et al., 1996]. An interesting property of γ crystallin is that when an aqueous solution of γs is cooled below a certain temperature T^*, the solution becomes opaque due to its spontaneous segregation into protein-rich and protein-poor fluid phases. This reversible liquid-liquid phase separation is caused by a net short range attractive interaction between the γs and is analogous to the phase transition of specific atomic fluids. Moreover, this coexistence is metastable with respect to solid-liquid phase boundary that is found at higher temperature [Berland et al., 1992], in analogy with short range attractive colloidal systems.

The discovery of phase transitions in solutions of γ proteins increased considerably the interest for this family of crystallin and their behaviour was investigated with particular attention in the region near their critical point. The liquid-liquid coexistence curve of the four members of the bovine γ crystallin family has been measured experimentally [Thomson et al., 1987; Broide et al., 1991]. Interestingly, these protein solutions were found to have the same critical exponents and, thus, to belong to the same universality class of atomic fluids. The coexistence boundaries of the four different families of crystallins obey the same critical relation that accounts for the coexistence curve of the analogous phase transition in atomic fluids:

$$|\frac{\phi_c - \phi}{\phi_c}| \quad = \quad A(\frac{T_c - T}{T_c})^{\beta}$$

where ϕ_c is the critical packing fraction of the protein solution and $\beta = 0.325$ is the coexistence critical exponent. The four members of γ crystallin family have approximately the same parameter A characterizing the width of the coexistence curve ($A = 2.6 \pm 0.1$) and the same critical packing fraction ($\phi_c = 0.2 \pm 0.02$). In contrast, the proteins divide into two categories for what concerns their critical temperature T_c: high T_c γ-crystallins with $T_c \simeq 38°C$ and low T_c γ-crystallins with $T_c \simeq 5°C$. The critical temperature is a direct measure of the strength of the non covalent attraction energy between proteins, while the critical density is known to be determined by the range. Since the high T_c and low T_c γ-crystallins have almost the same secondary and tertiary structures, their different critical temperature values might be due to differences in only a few amino acid residues in their respective sequences. Thus, apparently, minor chemical modifications can reduce, or increase dramatically the critical temperature of solutions of crystallin proteins and lead to eye lens opacification at completely different temperatures.

Furthermore, opacification due to liquid-liquid phase separation is not only found for in vitro solutions of γ-crystallins extracted from the lens, but it is also observed when cooling an intact young bovine lens below $15°C$ as the consequence of reversible phase separation [Tanaka and Benedek, 1975]. This somewhat artificial form of cataract, named *cold cataract*, is nevertheless a proof of the principle that liquid-liquid phase separation can lead to a separation of the concentrated cytoplasmic proteins solution into coexisting phases of different density and/or concentration.

The study of phase separation in crystallin protein solutions concentrated until now essentially on pure solutions of γ crystallins. In the last year, however, important progress in the scattering techniques have made possible the study of binary mixtures of crystallin proteins [Thurston, 2006]. The phase behaviour of these binary mixtures is certainly much more complex than that of the pure solution and nothing is known about the interactions between the different crystallin proteins. In the present work we will study binary mixtures of both α- and γ-crystallins at high concentrations comparable to those found in the eye lens. Using molecular dynamic simulations we will derive a colloidal model for these protein mixtures which can account for their experimental small angle neutron scattering data. The phase behaviour of this coarse-grained model will then be studied using a perturbation theory approach. The present work is a first step towards an understanding of the thermodynamic stability of the full α-β-γ mixture contained in the eye lens and of the relevance of phase separations in cataract formation.

CHAPTER 2

Colloidal model for eye lens protein mixtures

Summary

In this chapter, a colloidal model for binary mixtures of α and γ crystallin proteins is derived. Combining molecular dynamics (MD) simulations of a coarse-grained model of proteins with experimental small angle neutron scattering (SANS) data, the interactions between the proteins is modeled. We demonstrate that transparency of the eye lens is greatly enhanced by a weak, short-range attraction between α and γ-crystallins. Provided it is not too strong, such mutual attraction considerably decreases the critical temperature and the corresponding opacity due to light scattering, and it is consequently essential for eye lens transparency. We then discuss possible origins of these interactions and present further details of the model, in particular, the structural properties of the mixtures as obtained from the simulations.

2.1 Introduction

Proteins are attracting growing attention within the colloid physics community due to their suitability as model colloids, and this possibility of exploiting proteins as ideal colloids has already given promising results. Solutions of lysozyme, the *physicist's* protein, were found to exhibit a metastable liquid-liquid phase separation and posses a cluster phase at low ionic strength, and evidence for a glass line was also discovered [Dawson et al., 2001; Stradner et al., 2004b; Cardinaux et al., 2007]. The advantages of proteins are clear. In terms of structure, the often perfect monodispersity of single-chain proteins is a property currently out of reach for synthesis of organic and inorganic colloidal particles. Interprotein interactions also encompass richer and more interesting scenarios than are usually encountered in atomic systems. In fact, since proteins carry pH-dependent surface charges, their electrostatic interaction can be easily tuned by modifying the solvent properties (pH, ionic strength). Moreover, several proteins exhibit short-range attractive interactions whose strength can be modulated by simply varying the temperature [Piazza, 2004]. All these features make proteins an essential playground for understanding the equilibrium and non equilibrium phase behaviour of colloidal systems in general. As a matter of fact, the reverse is also true, and both colloidal and statistical physics are giving important contributions to the understanding of protein behaviour, especially in phenomena like aggregation, phase transition or dynamical arrest. These are all phenomena that involve a large number of proteins and for which atomistic approaches are clearly not feasible.

In analyzing colloidal systems, a coarse-graining procedure, which consists in integrating out a subset of the degrees of freedom, is usually the first and unavoidable step. This procedure is required to reduce the complexity of the interactions between components (electrostatic, hydrophobic, steric, entropic etc.) to an effective potential [Likos, 2001; Louis, 2001]. Once a suitable coarse-grained interaction has been devised, one can use the tools of statistical mechanics for simple liquids [Hansen and McDonald, 1986] to study the system. In practice, colloidal particles are treated as “big atoms” [Frenkel, 2002; Poon, 2004] with specific interaction potentials. In this way, insights have been obtained in a variety of contexts, including colloids, colloids-polymers systems, gels, glasses and aggregation kinetics (for recent reviews see for example Ref. [Likos, 2001; Anderson and Lekkerkerker, 2002; Zaccarelli, 2007]). Moreover, this approach has been successfully extended to protein solutions and has proven to be extremely valuable also for these more complicated systems [Foffi et al., 2002a; G Pellicane and Caccamo, 2004].

The colloidal models emerging from this interdisciplinary research are also giving new insights into numerous questions of biological and medical relevance. A broad and constantly growing class of diseases, such as Alzheimer’s disease, sickle-cell disease and cataract disease, to name only a few, involve protein association phenomena as an essential aspect. The basic element common to all members of this class of Molecular Condensation Diseases [Benedek, 1997], is an attractive energy of interaction between specific biologic molecules which produces condensation into dense, frequently insoluble mesoscopic phases. It appears that it is the subtle interplay between interprotein attraction and repulsion that leads to the condensed protein phase. Among this class of diseases, cataract is particularly important because it is the world’s leading cause of blindness and effective prevention or non-surgical cure is still lacking [D. Pitts et al., 1986]. Cataract is most often the consequence of an uncontrolled aggregation (or phase separation) of the proteins in the eye lens that results in a loss of its transparency.

2.2 Eye lens crystallin proteins

The cells of mammalian eye lenses contain an aqueous solution of highly concentrated lens-specific proteins, and are normally sufficiently transparent for vision. To understand the origin of normal lens transparency, it is essential to recognize that each of the proteins in the lens does not scatter light independently of its neighbors. Instead, the scattering in the eye lens is reduced by the correlation in the position of pairs of proteins [Benedek, 1971]. In a normal lens the local fluctuations of the concentration of proteins, on length scales comparable to the light wavelength, are small.

One of the principal ways of disrupting the needed local homogeneity in the eye lens is by the aggregation of lens proteins into high molecular weight clusters, that produce sufficient fluctuations to increase the turbidity and cause cataract. The needed homogeneous packing of lens proteins has indeed long been recognized to be fundamental for eye lens transparency, and has been characterized at molecular length scales using small-angle X-ray scattering [Delaye and Tardieu, 1983]. Many studies of this nature make cataract an example of a protein condensation disease where concepts from colloid science have already been successfully applied.

The highly packed proteins in the eye lens fiber cells are named “crystallins,” and the most common mammalian crystallins belong to the α, β and γ families. In this study we have focused on the α and γ crystallins. The former are globular, polydisperse, multi-subunit, 800 kDa proteins, whose interactions can be described to a good approximation with a simple hard-sphere colloid model [Finet and Tardieu, 2001]. The γ-crystallins are monomeric, with a molecular weight of about 21 kDa. The discovery of a metastable liquid-liquid phase separation provided the evidence for a short-range attraction between γ-crystallins and the use of the corresponding colloid model has led to a quantitative description of the phase behaviour [Thomson et al., 1987; Broide et al., 1991; Malfois et al., 1996; Fine et al., 1996; Lomakin et al., 1996; Asherie et al., 1998].

Crystallin aggregation and liquid-liquid phase separation can both produce density inhomogeneities that are the main sources of increased light scatter in cataract, and therefore continue to be major themes of lens protein research. Liquid-liquid phase separation not only gives rise to the so called *cold cataract* [Zigman and Lerman, 1964], but also dramatically enhances light scattering at body temperature, well above the critical point [Schurtenberger et al., 1989, 1993; Fine et al., 1996; Thurston, 2006]. The proximity of liquid-liquid phase separation also substantially affects the thermodynamic properties of lens protein mixtures [Vérétout and Tardieu, 1989; Liu et al., 1996, 1998; Thurston, 2006] and is therefore an important aspect to be taken into account for understanding the driving forces for chemical changes in the lens cytoplasm, including protein aggregation. The present work continues a process of extending the initial work on liquid-liquid phase separation and related properties of aqueous γ-crystallin solutions to successively more realistic mixtures of eye lens crystallins [Liu et al., 1996, 1998; Thurston, 2006; Stradner et al., 2007].

It is important to discuss the relationship of this work to investigations of eye lens proteins that are most commonly carried out at relatively dilute concentrations in comparison with those studied here. For example, the recognition of chaperone properties of the lens crystallins, and numerous subsequent biophysical, chemical and genetic studies, have considerably enhanced our understanding of lens protein aggregation [Horwitz, 1992; Putilina et al., 2003; Pigaga and Quinlan, 2006]. In both equilibrium and kinetic contexts, dilute and semi-dilute solution investigations are critical for determining key structural aspects of proteins, for identifying specific interactions between proteins, and for quantifying their strength. More specifically, it is clearly critical to determine the free energies and kinetics of formation of prevalent complexes of lens proteins, including their dependence on protein sequence, chemical modifications and solution conditions, and such investigations are most readily carried out without the added complexities of highly concentrated mixtures.

However, at the same time it has long been very clear that the high crystallin concentrations in eye lens cells produce emergent mixture properties, including phase transitions, that are at present very difficult to predict solely from knowing dilute solution properties. Therefore, both dilute and concentrated solution investigations are essential and indeed complementary for understanding the molecular driving forces that underly lens protein aggregation, phase separation and ultimately, cataract.

2.3 Experiments

Small angle neutron scattering experiments were performed on solutions of α and γB crystallins obtained by mixing different ratios C_α of a 230 mg/ml α-crystallin and a 260 mg/ml γB-crystallin stock solution, in 0.1 molar sodium phosphate buffer in D_2O at pH 7.1, with 20 millimolar dithiothreitol to inhibit protein oxidation and oligomerization. We define C_α as the relative volume of the α-solution according to :

$$C_{(\alpha)} = \frac{V_{(\alpha)}}{V_{(\alpha)} + V_{(\gamma B)}} \tag{2.1}$$

with $V_{(i)}$ denoting the volume of the protein solution of type i. In the following, γB crystallins will be simply denoted as γ.

The concentration of the γ-crystallins corresponds closely to their critical concentration C_c and all experiments were performed at a temperature of $25°C$ ($10°C$ above the critical temperature T_c of the γ's in the present buffer). The SANS spectra of the pure-α and pure-γ solutions together with the binary $C_\alpha = 0.125$, $C_\alpha = 0.25$ and $C_\alpha = 0.5$ mixtures are plotted in Fig. 2.1 and cover the wavevector magnitude q-range of 0.002-3 nm^{-1}. The pure γ solution is already highly critical, due to the proximity of the critical point of the gamma solution. T is indeed just above the critical temperature T_c^γ of the γs and the density of the solution is near to the critical one. Adding α-crystallins to the γ solution first slightly increases the forward scattering ($C_\alpha = 0.125$). The intensity at low q reaches a maximum for a mixing ratio of $C_\alpha = 0.25$ while the peak due to the hard-core of the α-crystallins appears at $q^*_\alpha \approx 2\pi/d_\alpha$. Thus, a first estimate of the α's diameter can be

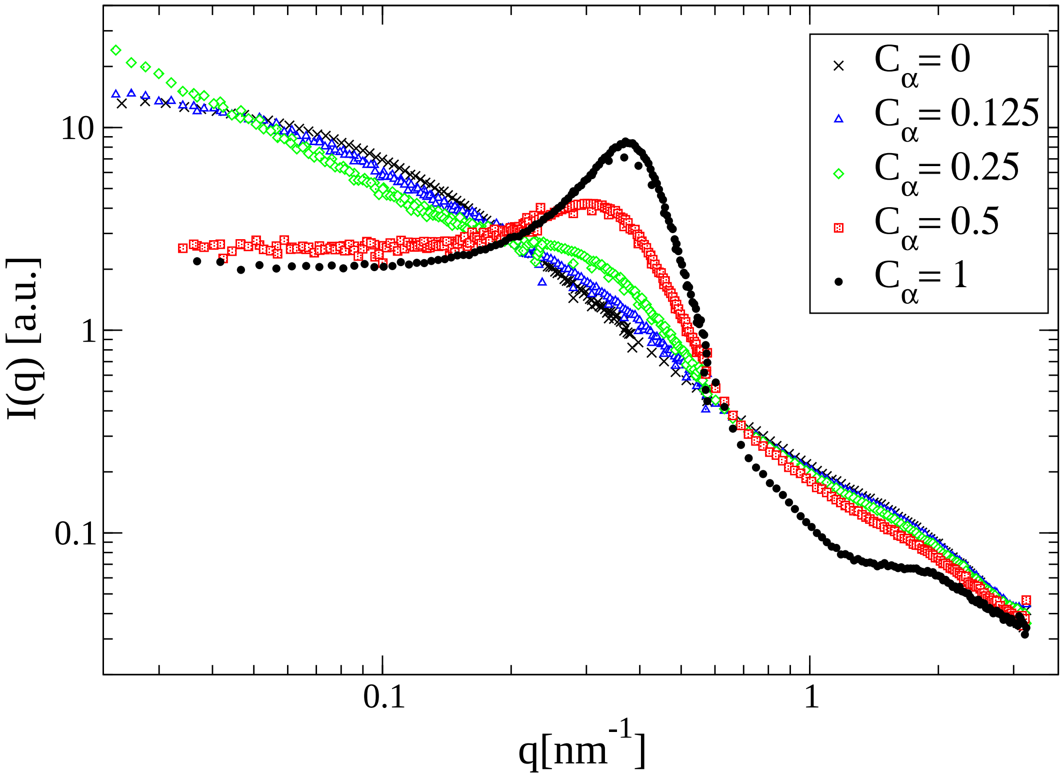

Figure 2.1: *Small-angle neutron scattering intensity $I(q)$ vs. wavevector magnitude q for high concentration bovine γB and α crystallin mixtures, showing evolution from pure γB to α. Mixing ratios C_α of a 230 mg/ml α-crystallin ($C_\alpha = 1$) and a 260 mg/ml γ-crystallin stock solution are shown as follows: pure α-crystallin, i.e. $C_\alpha = 1$ (dots), $C_\alpha = 0.5$ (squares), $C_\alpha = 0.25$ (diamonds), $C_\alpha = 0.125$ (triangles) and pure γ-crystallins, i.e. $C_\alpha = 0$ (crosses).*

inferred from the experimental spectra and the $d_\alpha \sim 160$ Å we measure is consistent with previous studies [Finet and Tardieu, 2001].

For $C_\alpha = 0.5$, the large scale fluctuations are already highly suppressed and the pronounced structure factor peak of the α-crystallins is found.

Qualitatively, as we have described, these measurements on high concentration mixtures show a combination of the key features of hard-core repulsion and short-range attraction that are relevant in the pure solutions. However, since quantitative models of interactions between proteins within mixtures cannot be inferred directly from the SANS experiments, especially for the interactions between unlike components, the next section is dedicated to building a quantitative, testable model for the relevant lens protein interactions with the aid of computer simulations.

2.4 Simulations and model validation

2.4.1 Model

The proteins are modeled as particles that have a simple short range interaction. Each protein is treated as an additive hard sphere with square-well (SW) interaction. Consequently, the interaction potential is defined as:

$$U_{ij}(x) = \begin{cases} \infty & \text{if } x < d_{ij}, \\ -u_{ij} & \text{if } d_{ij} < x < d_{ij} + \lambda_{ij} \\ 0 & \text{if } x > d_{ij} + \lambda_{ij}. \end{cases} \tag{2.2}$$

with $d_{ij} = (d_i + d_j)/2$ and d_i, the diameter of the i-species. The parameters u_{ij} and λ_{ij}, defining the energy scale and the range of the interactions respectively, are the key quantities of our model and will be fixed using the experimental spectra.

The interaction potential defined by Eq. 2.2 clearly represents a strong idealization of the true interaction between the proteins. All the internal degrees of freedom of the proteins and the directionality of their interaction are ignored.

In principle, an atomistic model that takes into account the internal structure of the two proteins could be studied by simulations. This approach, however, would be limited by the computational overhead to just a few proteins. Since we are interested in capturing the experimental phenomenology in a semi-quantitative manner, which requires considering collective properties on length scales much larger than the single proteins, the atomistic simulation route is not feasible. An atomistic model is also not an option since, while the structure of the γ-crystallins is known, the same is not yet true for the structure of the α [Blundell et al., 1981; Bettelheim et al., 1999].

A second advantage of our model is that it comprises a minimal set of parameters necessary to account for the key phase equilibrium and scattering properties observed to date in aqueous solutions of pure α, pure γ and their binary mixtures. Moreover, each model parameter has a specific physical interpretation. The SW potential, in particular, has already been successfully used to model the phase behaviour of γ-crystallins [Lomakin et al., 1996]. The choice of SW potential is certainly not unique and other shapes of the potential could also be considered. However, when the range of a spherically symmetric model attraction is smaller than the diameter of the particles, the phase diagram, liquid structure, and dynamics of the system is scarcely dependent on the exact shape of the potential; the second virial coefficient being the relevant parameter for both statics and dynamics [Foffi et al., 2002b; Noro and Frenkel, 2000]. Finally, SW potentials permit fast simulations and simplify significantly the calculations within the perturbative approach that will be discussed in the last section.

2.4.2 Simulations

We performed standard molecular-dynamics (MD) simulations in a cubic box with periodic boundary conditions for N=32000 particles (64000 for the pure γ case). The algorithm follows the usual event-driven scheme for particles interacting via stepwise potentials, in which the trajectories of the different components are propagated from one interaction to the next [Rapaport, 1995]. For each state point, up to 6 initial configurations were carefully equilibrated to the desired temperature by coupling the system to a thermostat. Once the system equilibrated, the production runs were performed by constant energy simulations. The scattering intensities were then computed from the configurations stored during these runs. To improve the statistics, the results of different independent runs were averaged, reducing significantly the error in the calculation of the scattering intensities, especially at low q-vectors. During the production runs the temperature and pressure were monitored to check that no phase separation or crystallization was occurring. In some cases, equilibration was not possible, the system being intrinsically out of equilibrium as we will see. This was an indication that a spinodal line/surface had been crossed. In this case, the measured scattering intensities were taken while the system was still coupled to the thermostat.

Partial structure factors and scattering intensities

Scattering techniques are one of the most important approaches to study the properties of soft matter. Depending on the length scales to be resolved and the contrast between suspended particles and solvent, the scattering of neutrons, X-rays or light is used. Experiments performed in the infinite dilute limit, i.e. at very low concentration, give access to quantities directly related to the size and shape of the suspended particles while, at higher concentration, we can gain information about particle arrangements and interactions. In the latter case, the relevant quantity is the static structure factor $S(q)$ that is defined as the equal time density-density correlation and reads for homogeneous systems:

$$S(q) \quad = \quad \frac{1}{N}\langle\sum_{i,j} e^{i\mathbf{q}\cdot(\mathbf{r}_i(t)-\mathbf{r}_j(t))}\rangle \tag{2.3}$$

where the sum runs over the N particles of the system and the density variables in the q-space are $\rho_q(t) = \sum_i e^{i\mathbf{q}\cdot\mathbf{r_i(t)}}$. This quantity is directly related by Fourier transform to the radial distribution function $g(r)$. By measuring first the form factor $I_0(q)$, the scattering intensity of a dilute sample of N_0 particles for which all correlations between the particles have been minimized, S(q) can be easily evaluated from the scattering intensity I(q) by computing the ratio [Klein, 2002]:

$$\frac{I(q)}{I_0(q)} = \frac{N}{N_0}S(q) \tag{2.4}$$

For a mixture of different components, the scattering experiments provide the total intensity scattered by the mixture, without distinguishing the contributions of the different components. In other words, the partial structure factors and the related partial radial distribution functions cannot be measured straightforwardly.

These quantities, however, can be directly accessed by numerical simulations and integral equations calculations [Caccamo, 1996] and they are related to the total scattered intensity measured in the experiments. The scattered intensity, versus scattering vector q, for a mixture of m components can be expressed as [Klein, 2002]:

$$I(q) = N \sum_{\mu,\nu=1}^{m} f_\mu(q) f_\nu(q) S_{\mu\nu}(q) \tag{2.5}$$

in which $f_\mu(q)$ denotes the form factor of particles of species μ and $S_{\mu,\nu}(q)$ the partial static structure factor:

$$S_{\mu\nu}(q) = \frac{1}{N}\langle \sum_{i=1}^{N_\mu} \sum_{j=i}^{N_\mu} e^{i\mathbf{q}\cdot(\mathbf{r}_{i\mu}(t)-\mathbf{r}_{j\nu}(t))}\rangle \tag{2.6}$$

For a binary α-γ mixture the scattering intensity reads:

$$\begin{aligned} \frac{I(q)}{N} &= f_\alpha^2(q)S_{\alpha\alpha}(q) + f_\gamma^2(q)S_{\gamma\gamma}(q) \\ &\quad +2f_\alpha(q)f_\gamma(q)S_{\alpha\gamma}(q). \end{aligned} \tag{2.7}$$

In this work, the total scattering intensity has been calculated by Eq. 2.7 with the partial static structure factors $S_{\mu\nu}(q)$ obtained from the simulations and the form factors $f_\mu(q)$ of the two species measured experimentally.

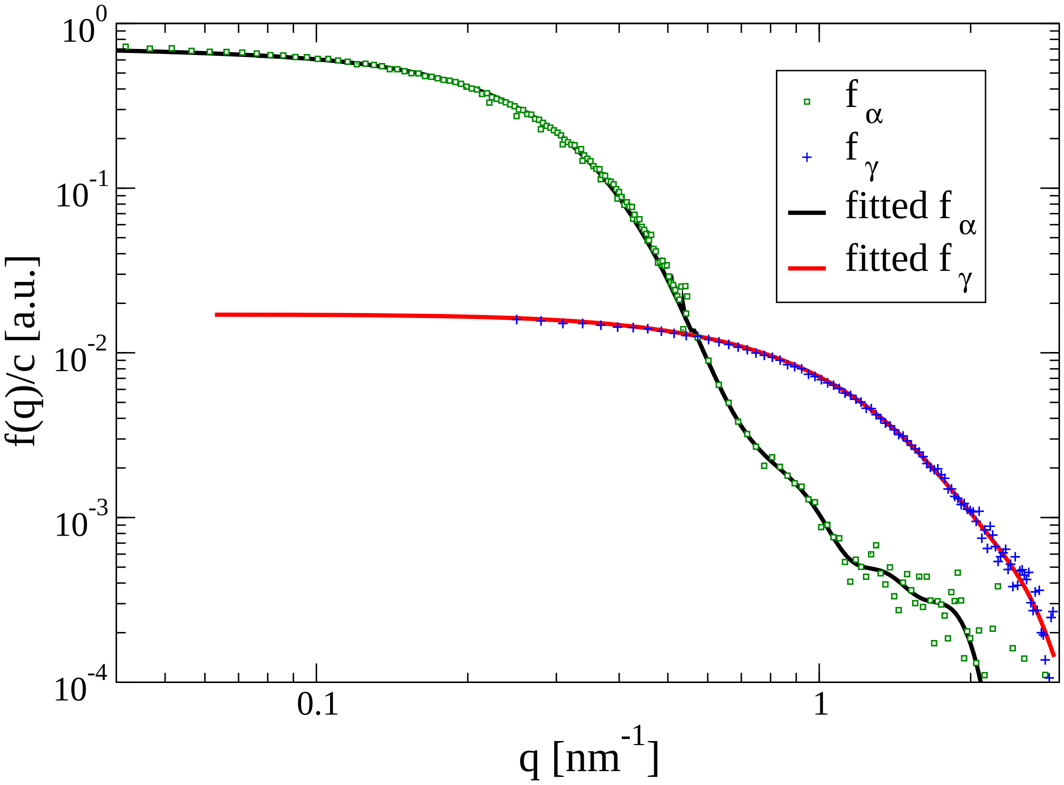

Figure 2.2: *Concentration-normalized scattered intensities of diluted* α*-crystallin (squares) and* γ*-crystallin (plus) solutions (4 mg/ml and 8 mg/ml) that were used as the experimental form factors. Also shown are the IFT fits (solid lines).*

The static structure factors $S_{\mu\nu}$ were calculated by averaging over several independent configurations and runs. To improve the statistics, averages over 300 different wave vectors $\mathbf{q}$ of the same modulus q were also performed. The experimental form factors were fitted using Indirect Fourier Transformation [Glatter, 1977] (IFT) to get rid of the experimental noise at high q and Guinier fit to have access to low q vectors [Guinier A., 1955]. The results are shown in Fig. 2.2. In order to account for the experimental smearing, we derived a general resolution function resulting from the combined effect of wavelength spread, finite collimation and detector resolution [Pedersen et al., 1990] (see Appendix A). The simulated scattering intensities were convoluted using this resolution function before comparing them with the SANS data.

2.4.3 Derivation of the model

In this section we shall describe the steps that we have followed to derive the parameters of the model introduced by Eq. 2.2. We will start by studying the pure solution of the two proteins. In this way, we will derive the parameters of the pure components, i.e. the attractive square-well depths ($u_{\alpha\alpha}$ and $u_{\gamma\gamma}$) and the ranges ($\lambda_{\alpha\alpha}$ and $\lambda_{\gamma\gamma}$). The second more challenging step will be towards modeling the binary mixtures. In this case, no prior studies were available, the interactions between unlike components were unknown and could not be inferred from the single component behaviour.

Pure component mixture

The experimental scattering intensity $I(q)$ as a function of the scattering vector q for the α-pure case is shown in Fig. 2.3. The main features are a low forward scattering $I(q \to 0)$ and a peak at around $q \sim 0.038$ Å^{-1}. In agreement with previous studies [Finet and Tardieu, 2001; Stradner et al., 2004a], we assume the interactions between α crystallins as purely repulsive, and so we model them as hard spheres. Taking for α-crystallins a molecular weight of 8×10^5 $g/mole$ and a radius of 81.5 Å, consistent with our observations, the volume occupied per unit weight of α crystallins is found to be 1.7 ml/g, in agreement with the value reported in previous studies [Veretout et al., 1989] for bovine α-crystallin. We finally obtained a value of 0.39 for the volume fraction ϕ_α corresponding to the pure 230 mg/ml stock solution. The effective diameter $d_\alpha = 163$Å derived by the comparison of the SANS results and the MD simulations is compatible with the values found in the literature [Finet and Tardieu, 2001].

A satisfactory agreement between the experimental and simulated intensities $I(q)$ is obtained as shown in Fig. 2.3. In terms of structure, the peak can be interpreted as the enhanced correlations at the contact distance between the particles. The location of the peak q^* varies with the diameter as $q^* \sim 2\pi/d_\alpha$. Even though the α-crystallins are globular proteins composed of many subunits and the solution is expected to be slightly polydisperse (15%) [Stradner et al., 2004a], the assumption of monodispersity used in this study is sufficient to recover the form of the experimental α-α correlation peak at this intermediate density. The polydispersity is expected to improve the agreement in the shape of the contact peak and it could be considered in future developments of the model.

Now we turn our attention to the γ solutions. Aqueous solutions of γ crystallins have attracted considerable interest in the past years as model system for the study of phase transition and critical phenomena [Thomson et al., 1987]. These solutions become turbid when cooled below a certain critical temperature which depends on the experimental buffer. Strong density fluctuations that occur near a critical point are responsible for a fluid-fluid phase separation of the solution. More specifically, a coexistence curve divides the density-temperature plane into a high temperature region, where a single homogeneous phase exists, and a low temperature one where two liquid phases of different density and concentration are in equilibrium. Due to the different refractive index of the phases at high and low concentrations, the solution appears opaque. Previous experiments led to the determination of the coexistence curve and critical point (ϕ_c, T_c) of the γ solutions demonstrating the presence of a second order liquid-liquid phase transition [Thomson et al., 1987]. While the exact location of the coexistence curve depends on the solvent and on the particular gamma crystallin being investigated, the solution properties have been found to scale with the reduced density and the reduced temperature $(T - T_c)/T_c$ [Thomson et al., 1987; Schurtenberger et al., 1989, 1993; Broide et al., 1991].

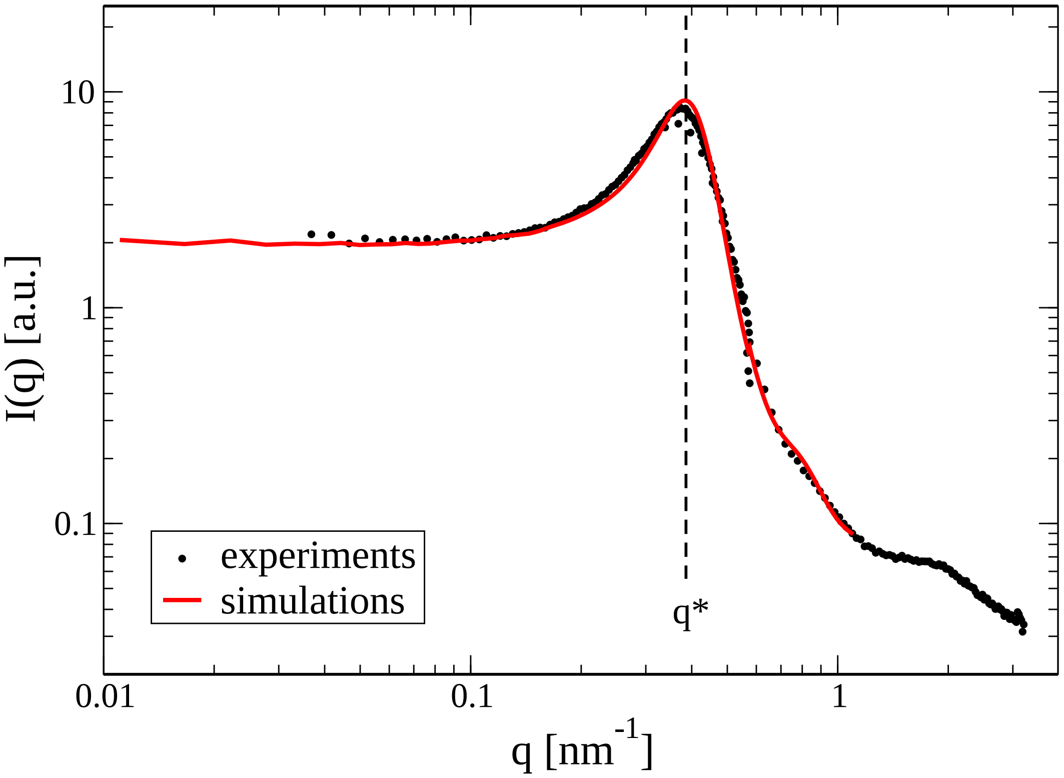

Figure 2.3: *Neutron scattering intensities for the concentrated, pure α crystallin solution in the present buffer are well-modeled with use of a hard-sphere potential in molecular dynamics simulations. SANS intensities (dots) and MD results (line) for hard-spheres at packing fraction $\phi_\alpha = 0.39$ are shown. The location of the peak $q^* \sim 2\pi/d_\alpha = 0.385\, nm^{-1}$ is also drawn.*

The first parameter that we shall set is the range for the $\gamma - \gamma$ interaction. This is fixed to reproduce the critical density obtained by the experiments. Square well systems have been intensively studied by means of Monte Carlo (MC) simulations and their coexistence curve computed for a large spectrum of attraction ranges [Vega et al., 1992]. In our case, a range $\lambda_{\gamma\gamma} = 0.25 d_\gamma$ produces the correct critical density. Indeed, MC simulations with this value of the short range attraction gave good agreement with the experimental coexistence curve [Lomakin et al., 1996].

In order to enhance the fluctuations, the experiments were performed at 25° C, close to $T_c = 15°$ C, the critical temperature of γ in the present buffer. The concentration of the γ-pure solution used here is close to the critical one, i.e. $c_c = 260\, mg/ml$, and corresponds to a packing fraction $\phi_\gamma = \phi_\gamma^c = 0.184$, given a specific volume for the γ-crystallins of $\nu = 0.71\, cm^3/g$ [Liu et al., 1996].

We performed the numerical simulations at this packing fraction using the $\lambda_{\gamma\gamma} = 0.25 d_\gamma$ for the square well potential, with $d_\gamma = 36$Å, the effective sphere diameter that reproduces the volume per molecule of the γ. Setting the energy parameter to $u_{\gamma\gamma} = 1$, in units of $k_B = 1$, leaves the temperature T as the only free parameter. For $\overline{T} = 0.7875$ good agreement between the experimental and numerical $I(q)$ is found, see Fig 2.4. The intensities show a strong forward scattering at large length scales (low q vectors) which is a direct consequence of the strong density fluctuations in the proximity of the critical point. Indeed, the structure factor $S(q)$ (proportional to $I(q)$ at low q) is defined as the density-density correlation function in Fourier space and the strong scattering is the result of long wavelength density fluctuations in the sample. These strong fluctuations are particularly important for the physiological function of the eye lens proteins which is to ensure the eye lens transparency. Benedek in his seminal paper – *Theory of Transparency of the Eye* – demonstrated that the turbidity of the cataractous eye-lens is related to microscopic spatial fluctuations in its index of refraction [Benedek, 1971]. In particular, the scattering of light is produced primarily by those fluctuations whose Fourier components have a wavelength equal or larger than half the wavelength of light in the medium. The low q-regime relevant for eye lens transparency is thus defined as $q \lesssim 0.047 nm^{-1}$ and particular care has been taken to reproduce the intensity in this region.

Not surprisingly, the agreement at high q-values is less satisfactory due essentially to the appearance of a nearest neighbor peak at $q^* \sim 2\pi/d_\gamma$ in the simulation data. Contrary to the α-crystallins, γ has been crystallized and its structure has been resolved [Blundell

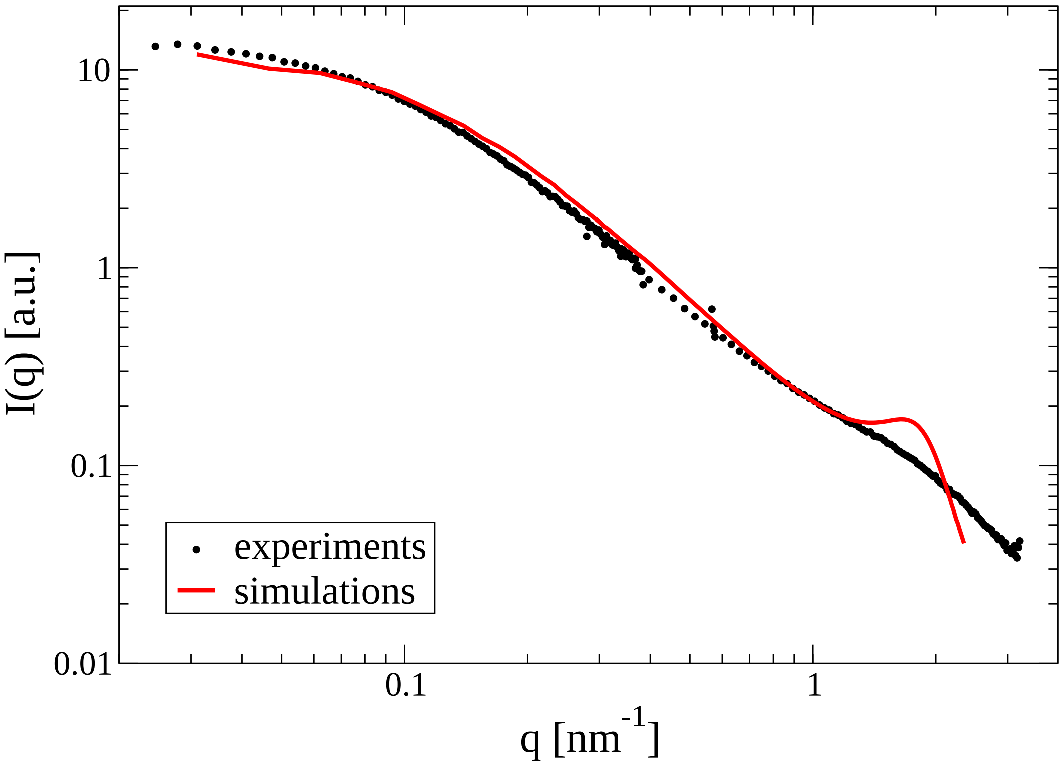

Figure 2.4: *Neutron scattering intensities for the concentrated, pure* γ *crystallin solutions in the present buffer can be approximated, for wave-vector magnitudes below 1 nm*$^{-1}$*, with use of a spherical square-well potential in molecular dynamics simulations. SANS measurements (dots) and results from molecular-dynamics simulations (line) for square-well particles (*$\lambda_\gamma = 0.25 d_\gamma$*,* $u_{\gamma\gamma} = 1$*,* $\overline{T} = 0.7875$ *) at packing fraction* $\phi_\gamma = 0.18$ *are shown.*

et al., 1981; Najmudin et al., 1993; Bettelheim et al., 1999; Kumaraswamy et al., 1996]. It consists of two distinct domains that form a slightly elongated ellipsoid. The discrepancy between simulation and experiment at high q might arise from the simplifying assumption of a spherical shape. In particular, the contact peak for ellipsoidal particles would be less pronounced due to the broadened distribution of the contact lengths.

Another essential feature of globular proteins, that is not considered in the present model and which may well affect the high-q scattering, is the strong directionality of the interactions. Proteins are characterized by patchy surfaces that are indeed essential for their biological roles. This has motivated the introduction of non isotropic models of protein phase behaviour. Patchy – or *aeolotopic* – models, that consider protein directional interactions, have been able to address phenomena such as protein aggregation, crystallization and self-assembly [Lomakin et al., 1999; Sear, 1999; DeMichele et al., 2006].

In this work, however, we shall show that even if an isotropic model of attraction represents a strong simplification, it is certainly adequate for our purpose since it reproduces the key features on the longer length scales of interest for transparency. The introduction of anisotropy, both in shape and interactions, might be an interesting refinement for further studies.

Binary α-γ mixtures

Inferring the microscopic interactions between proteins from scattering experiments becomes more complicated when dealing with systems composed of more than one component. The factorization of the scattering intensity $I(q)$ into a one-particle property and a genuine statistical mechanical quantity (see Eq. 2.4), like the structure factor $S(q)$, is no longer possible. As expressed by Eq. 2.7, the measured intensity is a result of a combination of the form factors and partial structure factors $S_{\mu,\nu}(q)$ of each component. The latter cannot be isolated by simply knowing $I(q)$. The MD simulations now become essential in the present context for understanding the microscopic interactions between the components that lead to the observed experimental scattering intensities of the mixtures.

Among the three different mixing ratios ($C_\alpha = 0.5, 0.25, 0.125$), $C_\alpha = 0.5$ closely resembles the natural α-γ crystallin concentration found in the eye lens nucleus [Veretout et al., 1989]. Therefore the model parameters for the mixtures are derived on this sample and then tested and confirmed also for the remaining mixing ratios. The temperature $\overline{T}$ at which the simulations on the mixtures are performed is fixed by the pure γ-case. The

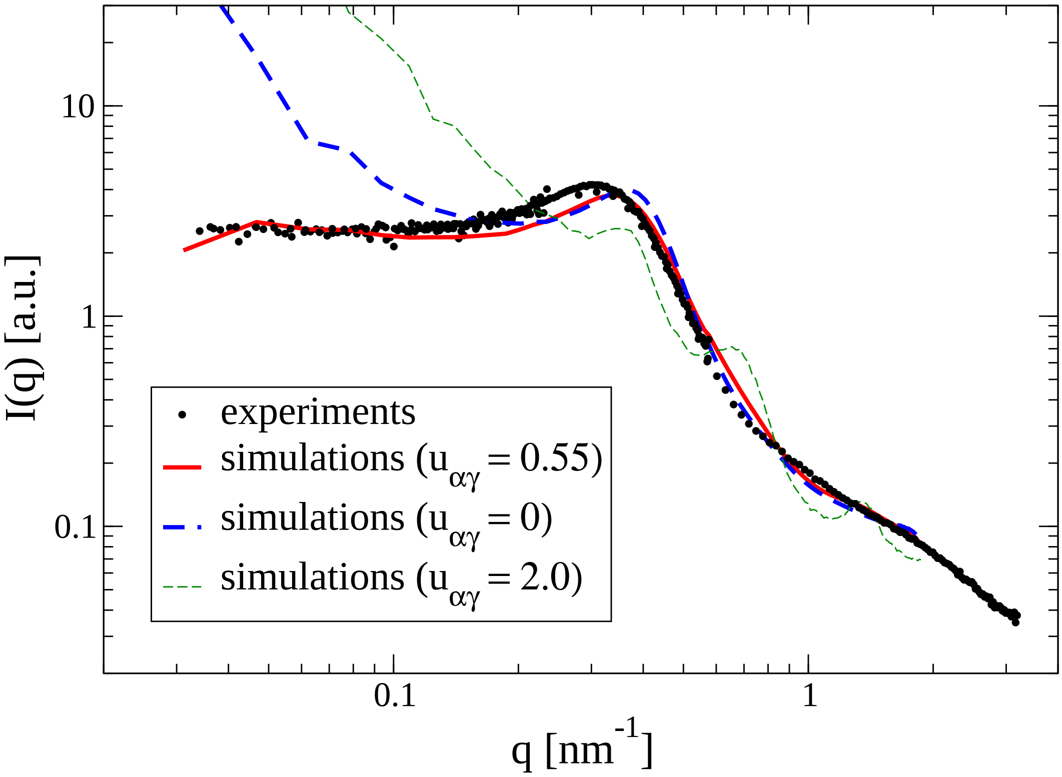

Figure 2.5: *Attraction between* α *and* γ *crystallins is essential for modeling neutron scattering intensities of their high concentration mixtures [Stradner et al., 2007]. SANS intensities for the* $C_\alpha = 0.5$ *mixture: (dots) and results from molecular-dynamics simulations at* $\overline{T} = 0.7875$ *are shown for three different values of the interspecies interaction (*$u_{\alpha\gamma} = 0$*,* $u_{\alpha\gamma} = 0.55$ $u_{\alpha\gamma} = 2$ *denoted by the dashed, the full and the dotted line respectively).*

remaining free parameter is the interaction between unlike proteins $u_{\alpha\gamma}$ that will turn out to be essential for understanding the stability of the binary mixture.

Since no previous studies of the present type for the interaction between the two crystallin proteins are available, we start with the assumption of a purely repulsive additive hard-sphere interaction between the two components, i.e. $u_{\alpha\gamma} = 0$. The striking disagreement between the forward scattering of the numerical results and the experimental data for $C_\alpha = 0.5$ is evident in Fig. 2.5. The experimental $I(q)$ resembles closely the pure α case with a peak at intermediate q range and a highly suppressed forward scattering [Fig. 2.1]. Considering hard-sphere repulsion among the two species only results in an enormous increase of the scattering intensity at low q which can be understood as an enhancement of the unstable region of the mixture. Indeed, we were not able to properly equilibrate the mixture during molecular dynamics simulations. The system began to phase separate, forming large domains of α-crystallin-rich and γ-crystallin-rich regions as clearly indicated from the snapshots presented later. In the real system, these effects usually start to emerge in $\alpha - \gamma$ mixtures at temperatures above the γ critical temperature that are somewhat lower than those investigated here [Thurston, 2006]. As a consequence of the high forward scattering, the transparency of the mixture would be lost, in contrast with the visual appearance of the sample and the SANS data which indicate that under the present conditions fluctuations at low q are highly suppressed.

It is clear that some elements that stabilize the mixtures have not been considered in this first model. Consequently, we speculate that a mutual attraction between unlike proteins might be present to circumvent these long-wavelength fluctuations and to stabilize the mixtures. We assume this attraction to have the same range as the one used for the attraction between γ-crystallins ($\lambda_{\alpha\gamma} = \lambda_{\gamma\gamma} = 0.25 d_\gamma$).

To pin down an effective well depth for this mutual attraction, we performed several simulations varying $u_{\alpha\gamma}$ from the hard sphere limit up to 2. The stability of the binary mixtures appears to depend on $u_{\alpha\gamma}$ in an extremely sensitive and non-monotonic way. To illustrate this point we plot in Fig. 2.6 the scattering intensity for a q vector in the region relevant for transparency ($q^* = 0.0467\, nm^{-1}$) as a function of the α-γ attraction for $C_\alpha = 0.5$. The system can be equilibrated for $0.5 < u_{\alpha\gamma} < 1$ and a low forward scattering, compatible with the experiments, is obtained for these values of $u_{\alpha\gamma}$. Outside this interval, the simulations show a clear sign of phase separation which indicates the

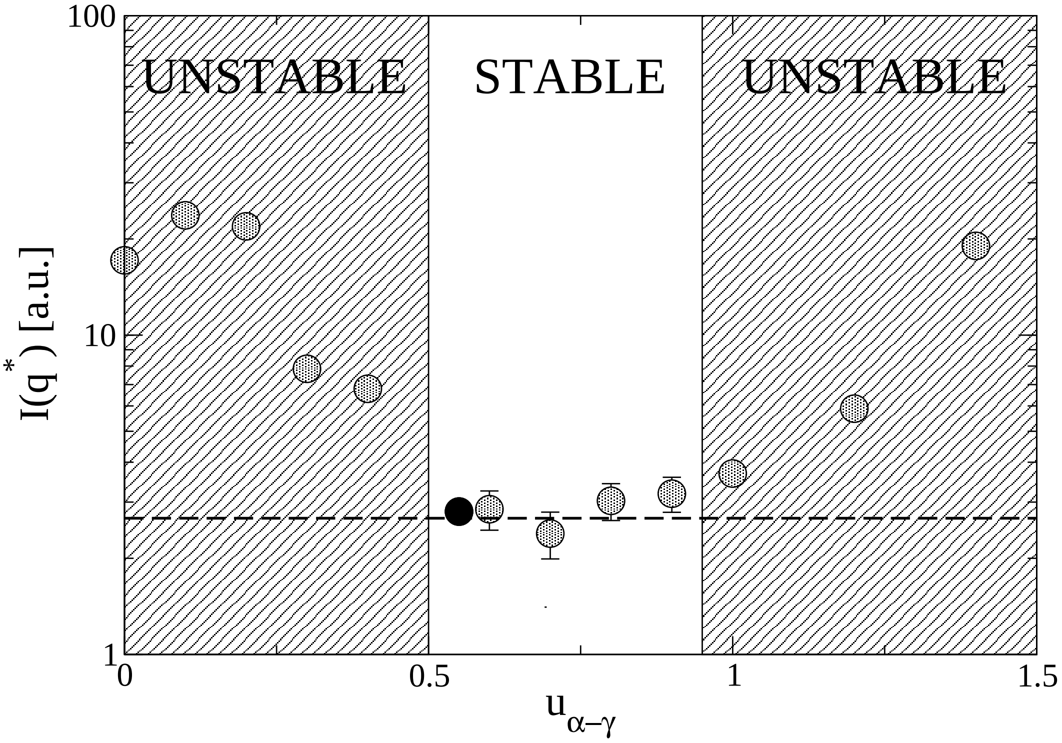

Figure 2.6: *A narrow range of the attraction strength between α and γ crystallins is compatible with avoiding high concentration phase separation instability. Dots show calculated neutron scattering intensities for $q^* = 0.0467\, nm^{-1}$, from analysis of molecular dynamics simulations, versus the α-γ attraction square well depth $u_{\alpha\gamma}$ for the $C_\alpha = 0.5$ mixture (see text). The attraction range in which the mixture remains stable against phase separation and can be equilibrated is also drawn. The dark point indicates the value of $u_{\alpha\gamma}$ we used to model the α-γ mixture and the dashed line represents the experimental $I(q^*)$*

crossing of an unstable region. The strong fluctuations at low q, that take place when an instability boundary is reached, are responsible for the enhancement of $I(q^*)$. The origin of these fluctuations and the nature of the phase separation will be investigated in the next sections.

We found that an interspecies attraction half of $u_{\gamma\gamma}$ ($u_{\alpha\gamma} = 0.55 u_{\gamma\gamma}$) is sufficient to

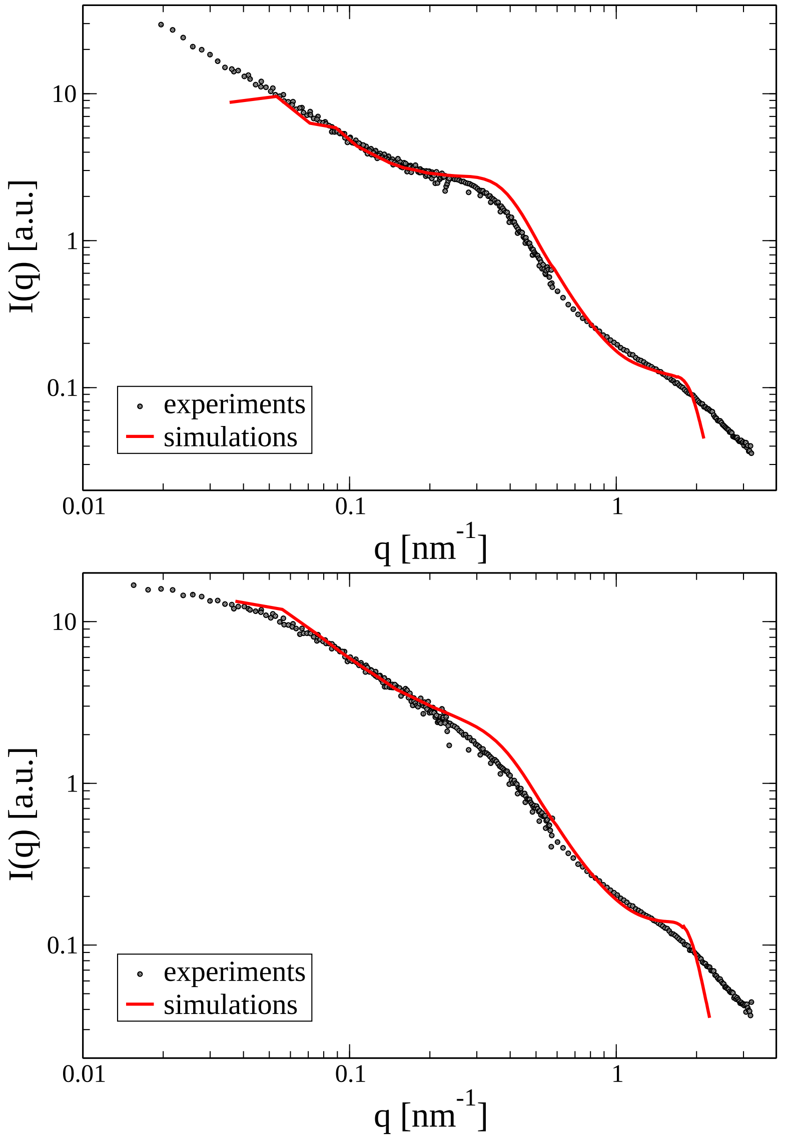

Figure 2.7: *The neutron scattering intensities for the* $C_\alpha = 0.25$ *(top) and* $C_\alpha = 0.125$ *(bottom) mixtures are compatible with the* α-γ *square-well depth determined by comparison of MD simulations with the* $C_\alpha = 0.5$ *SANS measurements. SANS measurements are represented by dots and results from molecular-dynamics simulations by full lines. The parameters of the simulated model are presented in Tables 2.1 and 2.2*

account for the SANS measurements and accurately reproduces the scattering intensities at low q. The parameters of our model of the α-γ mixtures are summarized in Table 2.1. For this choice, a simulated scattering intensity in good agreement with the experiments is obtained for $C_\alpha = 0.5$, see Fig. 2.5. Use of this attraction leads to a good description of the experimental $I(q)$ also for the remaining mixing ratios ($C_\alpha = 0.25, 0.125$) as reported in Fig. 2.7. The agreement for moderate q-vectors is less satisfactory. As for the pure mixtures case, this could be due to both polydispersity and anisotropy. In the q-region relevant for transparency, however, our simplified model gives a good account of the experimental results.

We have shown that this mutual attraction improves drastically the agreement with the experimental results. Its origin, however, remains unclear. In general, the exact origin of short range attraction in globular protein systems including γ crystallins and lysozyme [Muschol and Rosenberger, 1997] is still a challenging and open question. Three-dimensional protein structures often display large exposed hydrophobic regions, which are likely to play a prominent role in the interparticle interactions [Piazza, 2000, 2004]. Beside hydrophobicity, which is still far from being understood and whose contribution is difficult to evaluate, electrostatics might be important [Stradner et al., 2004b]. At $pH = 7$, where the experiments have been performed, α and γ crystallins are oppositely charged.

d_γ	1.0	λ_γ	0.25 d_γ	$u_{\gamma\gamma}$	1.0
d_α	4.53	λ_α	0.0	$u_{\alpha\alpha}$	0.0
$d_{\alpha\gamma}$	2.765	$\lambda_{\alpha\gamma}$	0.25 d_γ	$u_{\alpha\gamma}$	0.55

Table 2.1: *Parameters of the square well potential used for modeling the α-γ mixtures. The diameters d and ranges of the interaction λ are given in unit of $d_\gamma = 36$ $\mathring{A}$ and the depth of the potential u in units of $k_B = 1$. The temperature of the simulations was set to $T^* = 0.7875$.*

C_α	ϕ_α	ϕ_γ	N_α
0	-	0.184	-
0.125	0.049	0.163	104
0.25	0.098	0.140	240
0.5	0.195	0.093	704
1	0.391	-	32000

Table 2.2: *Parameters of the molecular dynamics simulations for the different* C_α*mixtures: the packing fraction of each component* ϕ_α *and* ϕ_γ *and the number of* α *components* N_α *are given (with* $N_\alpha + N_\gamma$*=32000).*

More specifically, α-crystallins are expected to carry $Z_\alpha = -180$ electronic charges per molecule at the experimental pH [Bera and Ghosh, 1998] while, for γ-crystallins, Z_γ is close to $+2e$ [Shand-Kovach, 1992]. This suggests that electrostatic interactions could be considered as one possible origin of the mutual interaction we have introduced in the model to reproduce the experimental data.

To further investigate this possibility, if we treat the proteins as charged colloids, we can use as interaction model a pair-wise screened Coulomb potential where the range of the electrostatic interactions is characterized by the Debye screening length κ^{-1} [Verwey and Overbeek, 1949; Leunissen et al., 2005]. This approach has often been used in the study of protein solutions [Chan et al., 1976; Leunissen et al., 2005; Zoetekouw and van Roij, 2006]. In order to estimate the electrostatic contribution to the expected $\alpha - \gamma$ attraction, we evaluated this pair-wise screened Coulomb potential with the experimental screening length $\kappa^{-1} \sim 6$ Å and compared it with the square-well potential we used for the simulations. We found that this screened Coulomb potential could not account for the magnitude of the interaction derived from the simulations; in order to recover the same second virial coefficient, a Z_α of $-450e$ would have been needed.

However, it should be mentionned that this approach is simply a starting point towards investigating the electrostatic contribution to α-γ interactions. It is in fact based on the hypothesis of a uniform charge distribution on the surface of a sphere, and on the use of dilute solution approximations to the nature of electrolyte solutions, long recognized to give inaccurate thermodynamic predictions at higher electrolyte concentrations unless they are considerably modified [Verwey and Overbeek, 1949; McQuarrie, 1976; Lee and Fisher, 1996; Bostrom et al., 2002]. For proteins, charged groups are far from being uniformly distributed on the surface, but rather assembled in patches that form a complex mosaic. Since the Debye length is smaller than the proteins, and, in particular, smaller than the distance between charge patches on the proteins, the rotationally averaged electrostatic screened potential would tend to underestimate the attractions. In order to investigate the origin of the attraction and how it might be influenced by electrostatics, one should therefore consider anisotropic interprotein potentials [Lomakin et al., 1999; Sear, 1999], as well as charge regulation [Kirkwood and Shumaker, 1952; Chan et al., 1976]

The ability of the γ-crystallins to fit into spaces between α subunits, which are about the same size as the γ's, could also lower the potential. In this context, taking into account the multi-subunit character of the α, or introducing some negative additivity ($2\, d_{\alpha\gamma} < d_\alpha + d_\gamma$) could also be interesting refinements of the model. Clearly these are all speculations and the quantitative molecular origins of the mutual attraction remain unknown and are worthy of further experimental and theoretical investigation.

Before moving to the description of the structural properties, we want to stress that the intrinsic anisotropic nature of the interactions does not significantly affect our results at low q, where the fluctuations that disrupt eye lens transparency occur. Indeed in this region, we can obtain a satisfactory agreement with the experiments by the simple isotropic potential defined by Eq. 2.2. For q vectors around the α-peak, angular-dependent interactions might be considered to improve the results. Moreover, the intrinsic polydispersity of α crystallins, which has to play a role in the properties of the pure α solution at higher packing, might also sensibly broaden the peak according to similar intuitive arguments to those given above in the case of the possible influence of the ellipsoidal shape of the γ crystallins.

2.4.4 Structural properties

One of the benefits of computer simulations for the study of binary mixtures is that the partial structure factors and partial radial distribution functions can be predicted. The partial structure factors quantify Fourier-transformed spatial arrangements of the individual protein components in the solution, with respect to each pair of species. Partial structure factor predictions both augment small-angle neutron scattering data and help the design of experiments that use selective species labeling or contrast variation to enable measurement of the partial structure factors.

Partial structure factors $S_{ij}(q)$

Since our model has been validated by comparison with the experiments, the structural properties obtained from the simulations can now give important predictions on the spatial organization of the different species. In Fig. 2.8, we reproduce the three partial structure factors obtained for the choice of parameters used to model the α-γ mixture (Table 2.1). From the structure factors, it is evident that an increase of the γ crystallin concentration fluctuations at large scale, indicated by the enhancement of $S_{\gamma\gamma}(q)$ at low q, is responsible for the mixture high criticality not only in the pure γ case, but also for the binary mixtures. Compared to the monodisperse γ solution, the presence of the larger size α's enhances the criticality of the γ-crystallin fluctuations. As observed for the experimental $I(q)$, the dependence of the critical behaviour on the relative composition of α and γ crystallins

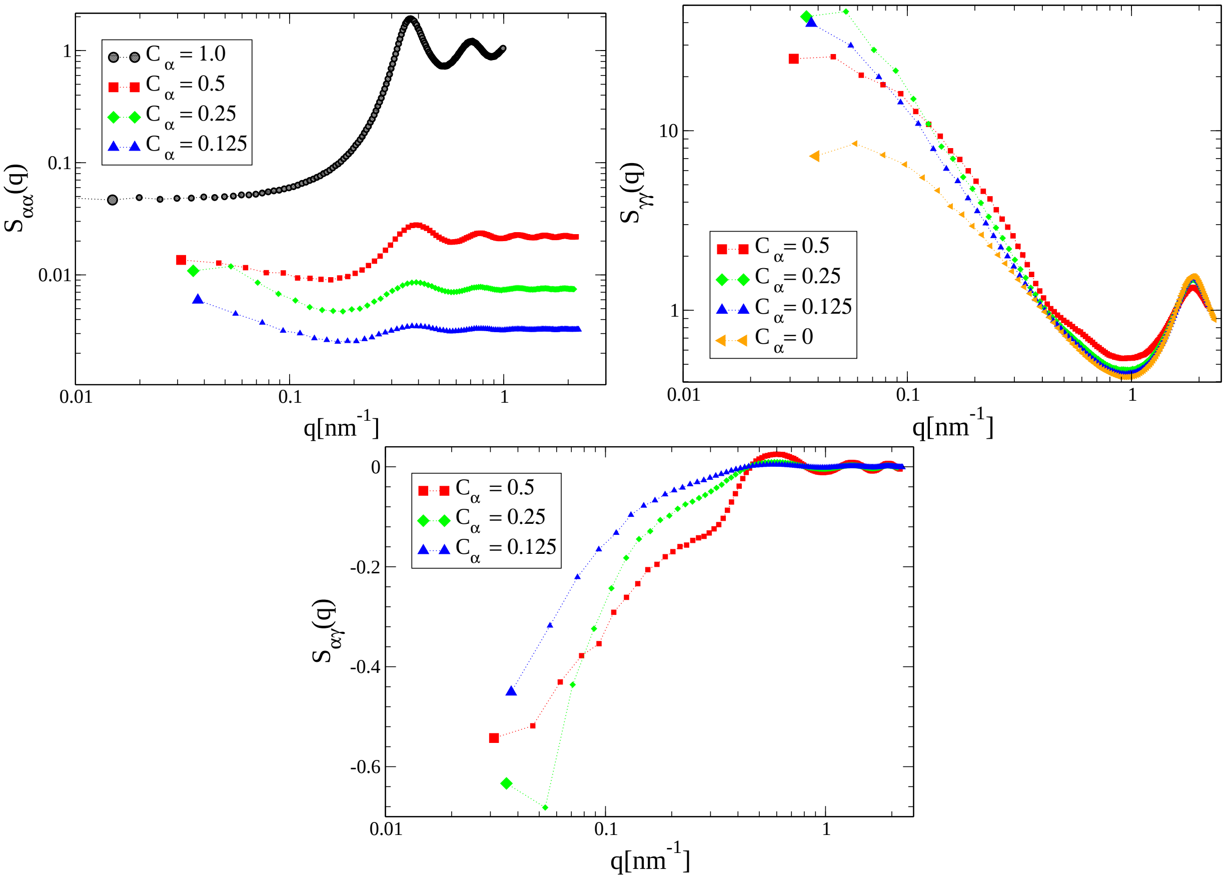

Figure 2.8: *Predicted partial structure factors obtained from the MD simulations of the various C_α mixtures. (upper left panel) $S_{\alpha\alpha}$; (upper right panel) $S_{\gamma\gamma}$; (lower panel) $S_{\alpha\gamma}$.*

is not monotonic. Indeed, for $C_\alpha = 0.25$ $S_{\gamma\gamma}(q)$ presents the strongest enhancement of large length scale fluctuations. This non-monotonic dependence of criticality on $\gamma - \alpha$ composition is consistent with the non-monotonic dependence of cloud temperature on α-γ composition found previously [Thurston, 2006].

$S_{\alpha\alpha}(q)$ also shows enhancement of large length scale fluctuations when increasing the amount of γ-crystallins in the solution, but in a less dramatic way. We also calculated the partial structure factors for other values of the mutual attraction. Outside the narrow interval of attraction strength shown in Fig. 2.6, all the structure factors present a strong increase at low q that is ultimately responsible for the strong forward scattering in the $I(q)$ spectra. This is illustrated in Fig. 2.5 for the case of weak ($u_{\alpha\gamma} = 0$) and strong attraction ($u_{\alpha\gamma} = 2$).

If we could experimentally modify the α-γ attraction without concomitantly changing other key interactions, the transparency of the sample in these high and low regimes would be lost. We anticipate that the nature of long wave-length fluctuations is different in the two extreme cases of primarily compositional and primarily protein density phase separation, as will be apparent later by visual inspection of the simulation box.

Partial radial distribution functions $g_{ij}(r)$

The structure in real space can give better insight into the local composition of the solutions, in particular for the spatial distribution of each species with respect to the other. For this reason, the partial radial distribution functions (RDF) for the different C_α are presented in Figs. 2.9, 2.10 and 2.11. For the RDF of α crystallins, the pure case exhibits the usual oscillations of a dense hard sphere system: the spatial arrangement of the components alternates between regions of enhanced and reduced probability of finding a particle at a certain distance r from another, compared to that for a uniform distribution.

The range of the spatial correlation between αs increases when γ's are added to the solution, as shown by the longer decay of the initial peak in $g_{\alpha\alpha}(r)$ (Fig. 2.9). This more collective behaviour is a clear sign that the mixtures are becoming closer to criticality. For the case $C_\alpha = 0.5$, however, the scattering intensity does not show such a long decay indicating strong fluctuations yet. This is due to the glue effect of the small attractive proteins that form complexes with the large ones, as indicated by the cartoon in Fig. 2.9, and, so, prevent demixing. This effect appears more clearly when increasing $u_{\alpha\gamma}$ up to the limit of the stability region (see inset of Fig. 2.9): the α-α contact peak is suppressed

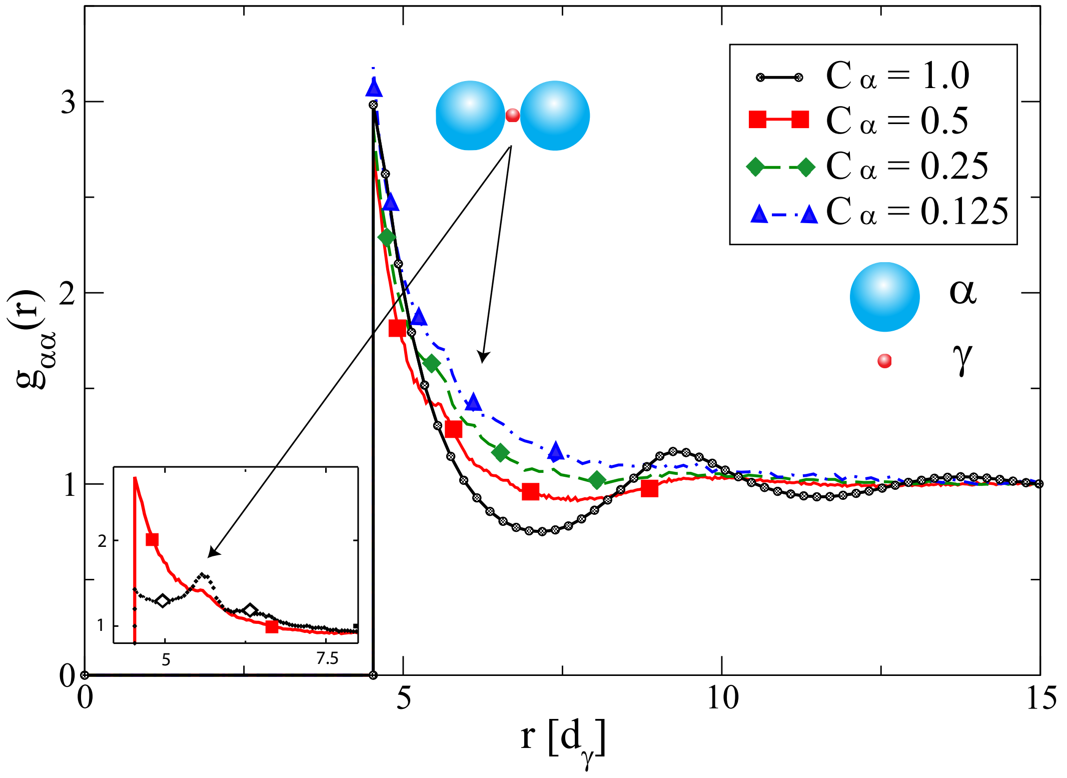

Figure 2.9: *Partial radial distribution functions $g_{\alpha\alpha}(r)$ from MD simulations of concentrated α-γ crystallin mixtures, showing neighboring α-α protein distributions as a function of mixing ratio, C_{α}. Key structural arrangements of the proteins that contribute to different peaks are also depicted (see text). The $g_{\alpha\alpha}(r)$ of the $C_{\alpha} = 0.5$ mixture for $u_{\alpha\gamma} = 0.55$ (line) and $u_{\alpha\gamma} = 0.9$ (dark diamonds) are compared in the inset.*

while there is a strong enhancement of α-γ-α configurations, as depicted in the cartoon of Fig. 2.9. A similar effect has been observed recently [Liu et al., 2006] in asymmetric binary Yukawa fluids, where a weak attraction between small and big components leads to the formation of a shell of small particles around the large particles, which weakens the effective attraction between the large components and, thus, decreases the critical temperature of the mixture.

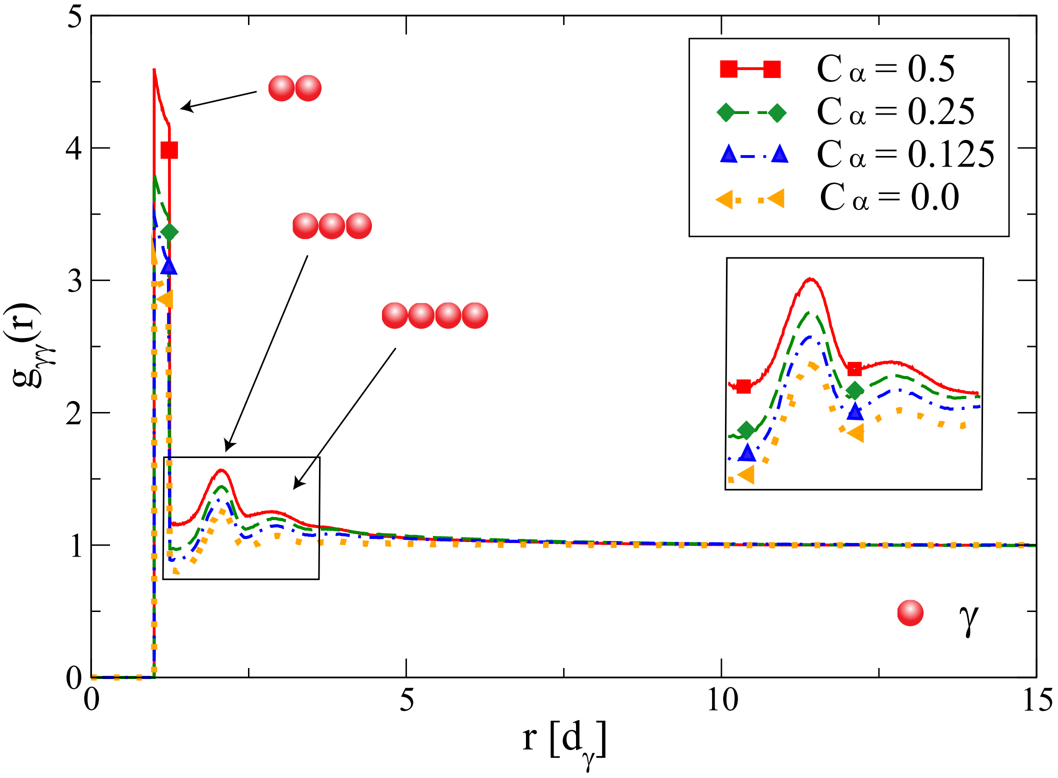

Figure 2.10: *Partial radial distribution functions* $g_{\gamma\gamma}(r)$ *from MD simulations of concentrated* α*-*γ *crystallin mixtures, showing neighboring* γ*-*γ *protein distributions as a function of mixing ratio,* C_α*. Key structural arrangements of the proteins that contribute to different peaks are also depicted (see text).*

For the γ crystallin RDFs (Fig. 2.10), the attractive wells give rise to a pronounced enhancement of the probability of finding proteins close to each other: the proteins are likely to stay closer than the outer range of their attractive well. Moreover, the contact value of $g_{\gamma\gamma}(r)$ grows with increasing α's due to the confinement of the small crystallins in the presence of the bigger α's. The structural arrangements of the proteins that contribute to the different peaks are also represented by cartoons in Fig. 2.10. Arrangements of two, three and four small particles become more probable with increasing concentration of the

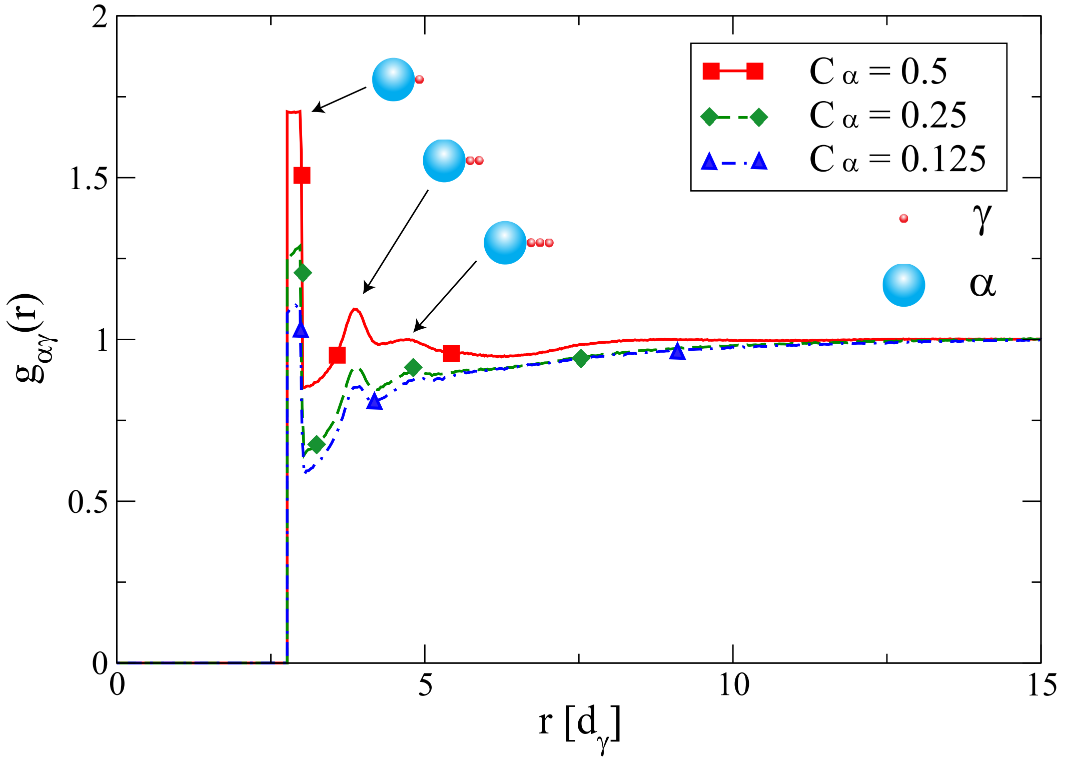

Figure 2.11: *Partial radial distribution functions $g_{\alpha\gamma}(r)$ from MD simulations of concentrated α-γ crystallin mixtures, showing neighboring α-γ protein distributions as a function of mixing ratio, C_α. Key structural arrangements of the proteins that contribute to different peaks are also depicted (see text).*

large component. In particular, for the interspecies $g_{\alpha\gamma}(r)$ RDFs presented in Fig. 2.11 there is a sensible increase in the coordination for the case $C_\alpha = 0.5$ with respect to the other more critical solutions. This enforces the idea that the small proteins act as glue between the large ones and thereby inhibit demixing. With too much α-γ attraction, however, larger α-γ *complexes* become too stable and strong density fluctuations start to dominate. In summary, a fine balance of the mutual attraction stabilizes the system against the two pathological situations.

2.4.5 Mixture stability tuning the α-γ attraction

For a precise study of the nature of the instabilities that are driving the phase separation of the different protein mixtures, one should really consider their thermodynamics and investigate their phase diagram. This will be done in details in Chapter 4. However, a visual inspection of the simulation box can provide already some very interesting informations. In Fig. 2.12, snapshots taken from simulations of the $C_\alpha = 0.5$ mixture with different values of the mutual attraction are presented. Since the full simulation box is extremely crowded, we present only slabs of thickness equal to the diameter of the large particles. For strong and weak $u_{\alpha\gamma}$ attraction, the system is out of equilibrium (see Fig. 2.6) and the configurations were taken while the system was still coupled to a thermostat, at the end of a long MD run.

For weak attractions, the snapshots reveal the coexistence of two different phases, one composed essentially of the smallest proteins and another where mainly the α are present: this is a demixing transition. Introducing an attraction between unlike proteins first counterbalances and efficiently suppresses segregation of the two proteins into large domains. An homogeneous and stable mixture is obtained for intermediate values of the mutual attraction. As discussed before, if the attraction is further increased, the mixture becomes again unstable. Contrary to the weak attraction regime, where concentration fluctuations seemed to dominate, the density inhomogeneities are now responsible for the instability. This is evident in the snapshots for strong attractions where large regions of high and low density dominate. Thus, upon increasing the $u_{\alpha\gamma}$ parameter one passes from a de-mixed state where α-rich and γ-rich phases coexist, to a stable one-phase region, and finally to another de-mixed state where a solvent-rich phase coexists with a higher density, protein-rich phase.

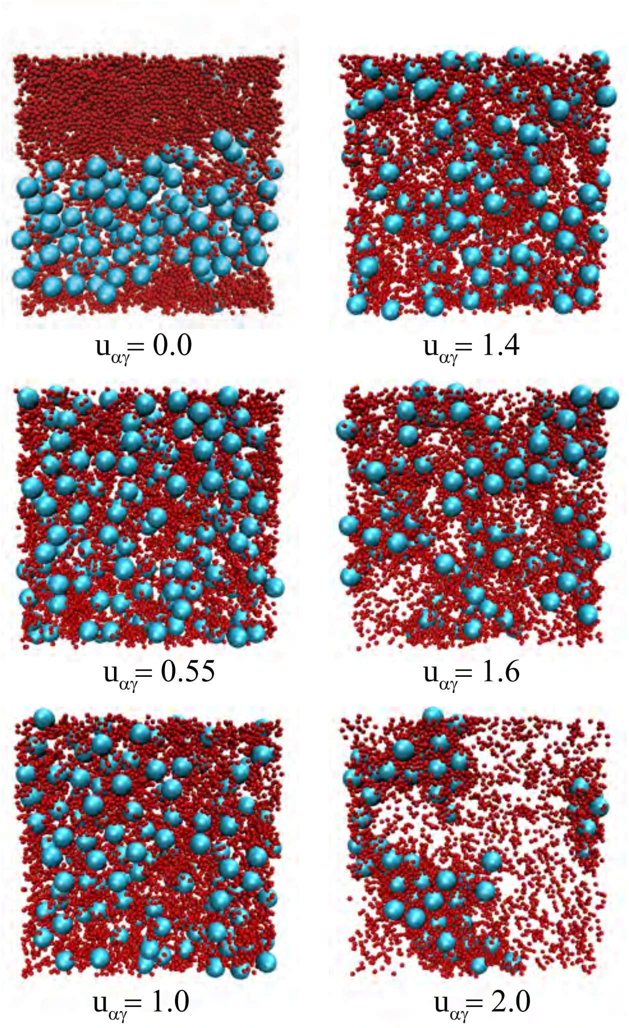

$u_{\alpha\gamma} = 0.0$ $u_{\alpha\gamma} = 1.4$

$u_{\alpha\gamma} = 0.55$ $u_{\alpha\gamma} = 1.6$

$u_{\alpha\gamma} = 1.0$ $u_{\alpha\gamma} = 2.0$

Figure 2.12: *Molecular dynamics snapshots showing the progression from segregation of* α-*crystallin and* γ-*crystallin by type* ($u_{\alpha\gamma} = 0$, *Upper Left), through one phase, stable mixing* ($u_{\alpha\gamma} = 0.55$, *Middle Left), to separation of a dense phase of both proteins* ($u_{\alpha\gamma} = 2.0$, *Lower Right). Simulations performed at* $\overline{T} = 0.7875$.

2.5 Conclusions

In this chapter, we have derived a colloidal model of α and γ crystallin proteins that is able to account for the experimental scattering intensities of both pure solutions and mixtures of these proteins. Very good agreement on the length scale important for the lens transparency was obtained. We found that the transparency of concentrated crystallin mixtures is maintained by introducing a weak, short-range attraction between α and γ crystallins. This attraction considerably decreases the critical fluctuations due to the attraction between γ crystallins and the tendency of highly asymmetric mixture to demix. Due in part to its small magnitude, the molecular origin of the inferred net short range attraction between unlike crystallins remains a challenging and open question, as it is for short range attraction of many globular proteins including γ crystallins and lysozyme [Piazza, 2000, 2004]. Moreover, an increase or a decrease in the short range attraction between unlike crystallins could have pathological effects on the lens transparency.

In this context, it is interesting to note that the existence of a mutual non-covalent attraction between α and γ crystallins has been recently found by microequilibrium dialysis and plasmon resonance experiments performed at low concentrations [Takemoto and Ponce, 2006; Ponce et al., 2006]. Moreover, those authors found that this non-covalent attraction seems to decrease with aging of the lens. The present work confirms the existence of α- γ attraction at high densities typical of the eye-lens, and demonstrates molecular mechanisms by which either loss or gain of α-γ attraction could lead to phase separation and opacification in cataract disease. The former possibility is intriguing in light of the finding that α- γ attraction seems to decrease with aging. The present findings also suggest that it would now be of great interest to measure the strength of γ-α attraction in cases of known cataractogenic mutations that affect the sequence of either γ or α crystallin.

The derivation of a colloidal model of $\alpha - \gamma$ lens protein solutions, compatible with the available experimental data, opens up the possibility of performing a thermodynamic analysis of the stability of such mixtures in the full parameter space where experiments and simulations have not been performed. The thermodynamic stability and the phase behaviour of the α-γ mixture will be studied in Chapter 4 using thermodynamic perturbation theory (PT). However, before applying to the crystallins mixture the PT formalism which is known to account correctly for the phase behaviour of one component solutions, we will first test in Chapter 3 the ability of perturbation theory to describe the phase diagram of mixtures of two components as well.

CHAPTER 3

Phase behaviour of binary mixtures

Summary

In this chapter we will use thermodynamic perturbation theory (PT) to study the stability of binary mixtures of simple interacting particles made of an hard core plus an attractive potential. The idea consists in deriving the equation of state of the interacting system by treating the attractive potential $u_{ij}(r)$ as a perturbation of the hard-sphere potential $u^0_{ij}(r)$. This leads to an expression for the Helmholtz free energy, which can then be analyzed to find the instability boundary and the phase diagram. In a first part, the expression for the free energy will be derived in the framework of the perturbation theory. The conditions of thermodynamic stability will be explicited. Within PT the determination of the instability surface (the spinodal) is straightforward and it gives already important insights into the coexistence boundaries (the binodal). The later, which is computationally more involved,

can be determined as well. As a first application of PT to the calculation of binary mixtures phase diagrams, the phase behaviour of the binary symmetric mixture of hard core Yukawa (HCY) particles will be determined. This model mixture has been widely investigated in the last years and our calculations will assess the validity of PT to describe the phase diagram of such mixtures. In a second step, binary mixtures with a slight asymmetry in the size of the two components will be studied. PT will prove to be really suitable to evaluate their instability and phase behaviour. This preliminary study will open the way to study the phase diagram of the eye lens protein model mixtures derived in Chapter 2 and its implications for cataract disease.

3.1 Introduction

Moving from one component fluid to binary mixtures considerably enhances the complexity of the phase behaviour. In addition to the liquid-vapor phase separation observed in one component systems, binary mixtures can also undergo a demixing transition. The phase diagram is thus determinated by the competition between liquid-vapor and mixing-demixing phase separation [Pini et al., 2003]. The presence of an additional degree of freedom, the concentration of the two species, considerably widens the spectrum of critical behaviours: tricritical points, critical end points, four phase points and critical lines replace the simple critical point and triple point found in one component fluids.

The first attempt to classify the rich variety of phase diagrams of binary mixtures was performed by van Konynenburg and Scott [van Konynenburg and Scott, 1980]. Their qualitative study, based on the van der Waals mean field expression for the equation of state is still the only systematic work on the phase behaviour of binary mixtures. Their work shows that the phase diagram topology is very sensitive to the precise combination of the parameters that characterize the interactions between the components. For interactions between particles of different species i and j modelled as the sum of a spherical repulsive hard core and a longer-range attractive tail, the relevant parameters are given by the hard-sphere diameters d_{ij}, the strength of the attractive interaction u_{ij} and the range of the attraction λ_{ij} $(i, j = 1, 2)$.

The application of reliable liquid state methods to determine the phase diagram of general binary mixture is certainly more involved than the simple van der Waals analysis and the number of free parameters definitely larger. Thus, more quantitative investigations of the phase diagram of *general* binary mixtures, and, eventually comparison with Monte-Carlo simulations, are still lacking. A first attempt to study the phase behaviour of binary mixtures on a quantitative level has been to reduce drastically the parameter space and consider the so-called symmetric mixture. In this class of systems, the two components have the same radius ($d_{11} = d_{22} = d_{12} = d$), the interaction strengths between like particles are equal ($u_{11} = u_{22} = u$), but a ratio of the interaction strengths between unlike species $\delta = u_{12}/u$ is introduced. Important results have been obtained for these particular mixtures from the Self-Consistent Ornstein Zernike (SCOZA) approximation and the Hierarchical Reference Theory (HRT) for Yukawa fluid [Scholl-Paschinger and Kahl, 2003; Pini et al., 2003]. However, the drawback of these methods is certainly their difficult generalization to more sophisticated mixtures.

In colloidal systems, important results have also been obtained by thermodynamic perturbation theory. Applying this theory to monodisperse short-range fluids, Gast, Hall and Russel were able to describe the phase diagram of colloidal particles interacting by depletion interactions [Gast et al., 1983]. More recently thermodynamic perturbation theory was used to understand the interplay between phase coexistence and the glass line [Foffi et al., 2002b]. If the perturbative approach is known to give quantitatively imprecise results near phase boundaries and near criticality, the method can be in principle applied to very general mixtures for which the convergence of integral equation based methods is still out of reach. Perturbation theory is thus well suited to study the stability of the modeled asymmetric crystallins mixtures.

In a first part, we will describe the first order thermodynamic perturbation theory that we used to determine the free energy of two components mixtures. The conditions under which these mixtures might become unstable will be explicited. The instability boundary (or spinodal surface), which is a local quantity, can be easily determined within this approach, while the binodal surface, which is the set of coexisting states, can also be computed.

As a validation of the perturbative approach to describe the phase diagram of binary mixtures, we will consider the symmetric mixtures of Yukawa particles. We shall show that the main topologies obtained from HRT, Mean Spherical Approximation (MSA) or Grand Canonical Monte Carlo (GCMC) approaches [Pini et al., 2003; Köfinger et al., 2006; Wilding et al., 1998] can be reproduced within perturbation theory. In a second step we will consider symmetric mixtures of Yukawa particles which belong to the different classes of phase diagram and introduce a slight asymmetry in the diameters of the two components. This size asymmetry, which suppresses some artificial topologies of the symmetric cases, lead to an interesting variety of phase diagrams that are, at the moment, very difficult to assess from other liquid states methods or computer simulations techniques.

3.2 Thermodynamic perturbation theory

The traditional descriptions of liquids or colloidal systems take advantage of the fact that the intermolecular pair potential can be naturally split into two parts: a steep, short range repulsion and a smoothly varying longer range attraction. It is now well accepted that the way in which the molecular hard cores pack determines the structure of most simple liquids, at least at high density, while the attractive interactions give rise to a uniform background potential which provides the cohesive energy of the liquid, but has little effect on its structure [Hansen and McDonald, 1986]. A further simplification consists in modeling the steep repulsion present when the distance between the particles is small by effective hard sphere interactions. In this way, the liquid properties can be related to those of the hard sphere fluid, whose structural properties and thermodynamics are well known, and the attractive part of the interaction is treated as a perturbation of the reference system. The representation of a liquid as hard spheres moving into an uniform attractive background provides the basis of the famous Van der Waals equation of state. However, at that time, little was known about the reference hard sphere fluid at high density and the excluded volume was taken into account only approximately, giving rise to the following equation of state that diverges at $\phi \rightarrow 0.25$, well below the fluid solid transition ($\phi \simeq 0.49$):

$$\frac{\beta P_0}{\rho} = \frac{1}{1-4\phi} \tag{3.1}$$

where P_0 is the pressure of the hard sphere fluid, ρ the density and ϕ the packing fraction ($\phi = \pi/6 \, d \, \rho$ for a sphere of diameter d). In the sixties, Widom showed that an equation of state thermodynamically consistent and compatible with the uniform attractive background is necessarily of the form:

$$\frac{\beta P}{\rho} = \frac{\beta P_0}{\rho} - \beta \rho a \tag{3.2}$$

where a is a positive constant which accounts for the fact that, when the density increases, the space available for inserting a new particle (i.e. the chemical potential) is lowered by an amount that is proportional to the density [Widom, 1963]. A first improvement of the Van der Waal's expression consisted in replacing the equation of state by a more accurate expression for hard spheres, like the Carnahan-Starling equation of state [Carnahan and

Starling, 1969]. The next step toward a substantial improvement of Van der Waals's theory was the derivation of the so called perturbation methods that we will describe now.

3.2.1 Perturbation theory and the λ expansion

Perturbation theory is based on the division of the pair potential into:

$$u(1,2) = u_0(1,2) + w(1,2) \tag{3.3}$$

where $u_0(1,2)$ is the pair potential of the reference system, and $w(1,2)$ the perturbation. We assume that the interactions between particles are pair-wise additive and that the system is homogeneous. Perturbation theory consists in computing the effect of the perturbation on the thermodynamics and the pair distribution function of the reference system via an expansion in power of the inverse temperature (the so called λ expansion) [Hansen and McDonald, 1986].

Consider a pair potential of the form:

$$u_\lambda(1,2) = u_0(1,2) + \lambda w(1,2) \tag{3.4}$$

where λ is a parameter that varies between 0 and 1 and gives the degree of perturbation: for $\lambda = 0$ the potential reduces to that of the reference system, whereas for $\lambda = 1$ the potential of the system of interest is obtained. Let $U_N(\lambda)$ be the total potential energy of a system interacting through 3.4:

$$U_N(\lambda) = \sum_{i=1}^{N} \sum_{j>i}^{N} u_\lambda(i,j) \tag{3.5}$$

The corresponding excess free energy, which gives the contribution to the free energy arising from the interactions between the particles is by definition:

$$F(\lambda) \;=\; -k_B T \ln \frac{Z_N(\lambda)}{V^N} \tag{3.6}$$

where Z_N is the configuration integral defined as:

$$Z_N(\lambda) \;=\; \int exp(-\beta U_N(\lambda)) d\mathbf{r}^N \tag{3.7}$$

Z_N simplifies to V^N in absence of interaction between the components ($U_N(\lambda) = 0$). The derivation of the Helmoltz excess free energy with respect to the coupling parameter λ yields:

$$\begin{aligned} \beta \frac{\partial}{\partial \lambda} F(\lambda) &= \frac{1}{Z_N(\lambda)} \int exp(-\beta U_N(\lambda)) \beta U'_N(\lambda) d\mathbf{r}^N \\ &= \beta \langle U'_N(\lambda) \rangle_\lambda \end{aligned} \tag{3.8}$$

where $U'_N(\lambda) \equiv \partial U_N(\lambda)/\partial \lambda$ and the bracket denotes a canonical ensemble average for the system characterized by $u_\lambda(1,2)$. For the potential defined in 3.5, $U'_N(\lambda) = \sum_{i=1}^{N} \sum_{j>i}^{N} w(i,j) \equiv W_N$. Integrating 3.8 yields:

$$\beta F(\lambda) \;=\; \beta F_0 + \beta \int_0^\lambda \langle W_N \rangle_\lambda d\lambda \tag{3.9}$$

with the excess free energy of the reference system $F_0 \equiv F_{\lambda=0}$. If we expand the ensemble average $\langle U'_N(\lambda) \rangle_\lambda$ around $\lambda = 0$ we obtain:

$$\langle W_N \rangle_\lambda \;=\; \langle W_N \rangle_{\lambda=0} + \lambda \frac{\partial}{\partial \lambda} \langle W_N \rangle_\lambda |_{\lambda=0} \tag{3.10}$$

with:

$$\frac{\partial}{\partial \lambda}\langle W_N\rangle_\lambda = -\beta(\langle [W_N]^2\rangle_\lambda - \langle W_N\rangle_\lambda^2) \tag{3.11}$$

which gives, by insertion into 3.9 :

$$\beta F = \beta F_0 + \beta\langle W_N\rangle_0 - \frac{1}{2}\beta^2(\langle W_N^2\rangle_0 - \langle W_N\rangle_0^2) + O(\beta^3) \tag{3.12}$$

This series was first derived by Zwanzig [Zwanzig, 1954] and is a true *high temperature expansion* when the system of reference is a hard sphere fluid and the canonical ensemble average depends only on density. For other reference systems, the averages are in general also functions of temperature and the λ expansion can not be reduced to a Taylor series in T^{-1}. The assumption of pairwise additivity of the potential including the perturbation leads to an expression for the free energy of the form:

$$\frac{\beta F}{N} = \frac{\beta F_0}{N} + \frac{\beta}{2N}\int_0^1 d\lambda \int\int \rho_\lambda^{(2)}(1,2)w(1,2)d1d2 \tag{3.13}$$

where $\rho_\lambda^{(2)}(1,2)$ is the pair density for the system with potential $u_\lambda(1,2)$ that can be expanded in powers of λ:

$$\rho_\lambda^{(2)}(1,2) = \rho_0^{(2)}(1,2) + \lambda\frac{\partial}{\partial\lambda}\rho_\lambda^{(2)}(1,2)|_{\lambda=0} + O(\lambda^2) \tag{3.14}$$

The first order term in the high-temperature expansion of the free energy is obtained by inserting the term of zeroth order in λ of the expansion of the pair density in 3.13:

$$\begin{aligned}\frac{\beta(F-F_0)}{N} &= \frac{\beta}{2N}\int\int \rho_0^{(2)}(1,2)w(1,2)d1d2 \\ &= \frac{\beta\rho}{2}\int g_0(\mathbf{r})w(\mathbf{r})d\mathbf{r}\end{aligned} \tag{3.15}$$

where $g_0(r)$ is the radial distribution function of the reference system. It is clear from this expression that the structure of the fluid is not influenced by the perturbation and that perturbation theory is indeed a mean field like theory.

Perturbation theory has been generalized to multi-components mixtures following the same arguments [Barker and Henderson, 1967]. The expression for the Helmholtz free energy F in terms of the averages of $\beta u_{ij}(r)$ and its powers taken over the unperturbed binary hard-sphere fluid ensemble reads for the first order case:

$$\frac{F - F_0}{Nk_bT} = \frac{1}{2}\rho\beta \sum_{i,j=1}^{2} x_i x_j \int u_{ij}(\mathbf{r}) g^0_{ij}(\mathbf{r}) d\mathbf{r} + O(\beta^2) \tag{3.16}$$

where F_0 and $g^0_{ij}(r)$ are the free energy and the partial radial distribution function of the unperturbed system. A binary mixture of spherical particles of radius d_1 and d_2 is unequivocally defined by giving the number of particles of each kind, N_i $(i = 1, 2)$ and the volume V occupied by the system. The overall number density is then defined by $\rho = (N_1 + N_2)/V$ and the mole fraction, which gives the relative concentration of the two species, by $x = N_1/N$.

We used the Boublik-Mansoori-Carnahan-Starling-Leland $(BMCSL)$ equation of state for the free energy of the binary hard-sphere reference mixture F_0 [Carnahan and Starling, 1969; Boublík, 1970; Mansoori et al., 1971] and the partial radial distribution $g^0_{ij}(r)$ functions were computed solving the Ornstein-Zernike equations with the partial direct correlation functions $c_{ij}(r)$ of the binary mixture obtained by Lebowitz within the Percus-Yevick (PY) approximation [Lebowitz, 1964]. In order to correct the shortcomings of the PY hard sphere distribution functions (the values at contact $g^0_{ij}(d_{ij})$ and the slopes $g^0_{ij}{}'(d_{ij})$ are both too small in magnitude) we used the Grundke-Henderson procedure, a generalization to mixtures of the Verlet-Weis modifications [Verlet and Weis, 1972; Henderson and

Grundke, 1975]. Details of the calculation of the $g_{ij}^{0}(r)$s are presented in Appendix B.

Approximations for the second and higher order terms have also been proposed [Barker and Henderson, 1967; Gil-Villegas et al., 1997; Paricaud, 2006]. For one component systems, this perturbative approach gives qualitatively good results even if, for short ranges of the attraction, it overestimates the liquid-vapor critical temperature T_c and underestimate the critical number density ρ_c. Taking into account the second order correction gives slight improvements in (ρ_c, T_c) with respect to MC simulation results, but a quantitative discrepancy remains [Vega et al., 1992]. Thus the general stability picture of the binary mixture is expected not to depend on the approximations used and a first order approximation is certainly sufficient for the purpose of the present study.

3.2.2 Stability criteria: the spinodal

The condition of thermodynamic stability of the binary mixtures is obtained by considering the Helmholtz free energy F and its minima. It is convenient to scale F and the other extensive variables, V and N_i $(i = 1, 2)$, by the total number of particles $N = N_1 + N_2$. The reduced free energy f is then a function of the volume per particle $v = \rho^{-1}$ and the mole fraction x, as in Eq. 3.16. The conditions of equilibrium and stability will be derived in terms of these scaled quantities.

For equilibrium at a point on the $f-x-v$ surface, at a given temperature, it is necessary that the tangent plane lies below the surface at that point. In other words, any fluctuation in mole fraction or volume per particle from an equilibrium state should not lead the system out of this equilibrium. This condition of local stability of an equilibrium state is fulfilled if the second order differential of the thermodynamic potential (the Helmholtz free energy f for the choice of the v and x variables) at constant T is a positive definite quadratic form at that state:

$$
\begin{aligned}
\delta f^2 &= \frac{1}{2}[\left(\frac{\partial^2 f}{\partial v^2}\right)_{T,x} \delta v^2 + 2\left(\frac{\partial^2 f}{\partial v \partial x}\right)_T \delta v \delta x \\
&+ \left(\frac{\partial^2 f}{\partial x^2}\right)_{T,v} \delta x^2] \;>\; 0
\end{aligned} \tag{3.17}
$$

This condition of stability might be rewritten introducing $[f]$, the $stiffness\ matrix$ [Tisza, 1966] of the Helmholtz free energy f:

$$
\begin{aligned}
\delta f^2 &= f_{vv}\delta v^2 + 2f_{vx}\delta v\delta x + f_{xx}\delta x^2 \qquad (3.18)\\
&= \begin{pmatrix} \delta v & \delta x \end{pmatrix} \begin{pmatrix} f_{vv} & f_{vx} \\ f_{vx} & f_{xx} \end{pmatrix} \begin{pmatrix} \delta v \\ \delta x \end{pmatrix} \;>\; 0
\end{aligned}
$$

where $f_{\mu\nu} \equiv \frac{1}{2}\left(\frac{\partial^2 f}{\partial \mu \partial \nu}\right)_T$ and $f_{\mu\mu} \equiv \frac{1}{2}\left(\frac{\partial^2 f}{\partial \mu^2}\right)_{T,\nu}$ $(\mu, \nu = v, x)$. Such a quadratic form is most conveniently discussed by reduction to the diagonal form :

$$
\delta f^2 = \frac{1}{2}\sum_{k=1}^{2} \lambda_k \delta\xi_k^2 \tag{3.19}
$$

This is achieved by a non-unique singular linear transformation of the variables which, thus, gives different set of diagonal elements λ_μ. Usually an orthogonal transformation is used for the diagonalization of a quadratic form but the eigenvalues obtained in this way are not directly related to physical quantities. Thus, it is preferable to consider a different, non-orthogonal transformation which allows one to relate the eigenvalues of the quadratic form to physically meaningful quantities [Tisza, 1966; Ursenbach and Patey, 1994].

Factorizing with respect to f_{xx} and completing the square in Eq. (3.17) yields:

$$
\begin{aligned}
\delta f^2 &= (f_{vv} - \frac{f_{vx}^2}{f_{xx}})\delta v^2 + f_{xx}(\delta x + \frac{f_{vx}}{f_{xx}}\delta v)^2 \\
&= (f_{vv} - \frac{f_{vx}^2}{f_{xx}})\delta \xi_2^2 + f_{xx}\delta\xi_1^2
\end{aligned} \tag{3.20}
$$

where :

$$\begin{aligned} \delta\xi_1 &= (\delta x + \frac{f_{vx}}{f_{xx}}\delta v) \\ \delta\xi_2 &= \delta v \end{aligned} \tag{3.21}$$

The conditions for a system to be thermodynamically stable (or metastable) can thus be written either

$$f_{xx} > 0 \quad and \quad f_{vv} - \frac{f_{vx}^2}{f_{xx}} > 0 \tag{3.22}$$

or,

$$f_{vv} > 0 \quad and \quad f_{xx} - \frac{f_{vx}^2}{f_{vv}} > 0 \tag{3.23}$$

when computing the factorization with respect to f_{vv}.

The second-order derivatives of a scaled thermodynamic potential with respect to a scaled extensive variable must be positive for a system to be stable. Moreover, even if the considered transformations take place at constant mole fraction and volume per particle, it is possible to consider slightly different thermodynamic potentials and express the stability criteria in terms of their derivatives, in which all variables held constant are intensive variables [Ursenbach and Patey, 1994]. Indeed, instead of the Helmholtz free energy one might consider the Gibbs free energy g or the quantity $f' \equiv f - x(\mu_2 - \mu_1)$ (with μ_i, the chemical potential of species i) and express the condition of stability in terms of the partial derivatives of these potentials :

$$\begin{aligned}\left(\frac{\partial^2 f'}{\partial v^2}\right)_{T,\mu_2-\mu_1} &= \left(\frac{\partial^2 f}{\partial v^2}\right)_{T,x} - \left(\frac{\partial^2 f}{\partial v \partial x}\right)_T \left(\frac{\partial^2 f}{\partial x^2}\right)^{-1}_{T,v} \\ &\equiv f_{vv} - \frac{f_{vx}^2}{f_{xx}}\end{aligned}$$

$$\begin{aligned}\left(\frac{\partial^2 g}{\partial x^2}\right)_{T,P} &= \left(\frac{\partial^2 f}{\partial x^2}\right)_{T,v} - \left(\frac{\partial^2 f}{\partial v \partial x}\right)_T \left(\frac{\partial^2 f}{\partial v^2}\right)^{-1}_{T,x} \\ &\equiv f_{xx} - \frac{f_{vx}^2}{f_{vv}} \qquad (3.24)\end{aligned}$$

The stability criteria previously derived require these two quantities to be positive. An interesting point is that the derivatives in which all variables held constant are intensive, and which are usually named *primary* stability indicators, are always less than or equal to corresponding derivatives with some extensive variables held constant (*secondary* indicators). In one-component systems, the inverse of the isothermal compressibility $\chi_T^{-1} \equiv (\partial^2 f/\partial v^2)_T$ is a primary indicator and vanishes as the instability is reached. This instability, called *mechanical instability*, occurs when *density* fluctuations become infinite in the system and allows the nucleation of low and high density phases that then coexist. This instability is responsible for the usual liquid-vapor phase transition encountered in one component systems.

In binary mixtures, the system might become mechanically unstable without the inverse of the corresponding compressibility $\chi_{T,x}^{-1} \equiv (\partial^2 f/\partial v^2)_{T,x}$ vanishing since it follows from (3.24) that the only required condition is instead, that $\chi_{T,\mu_2-\mu_1}^{-1} \equiv (\partial^2 f'/\partial v^2)_{T,\mu_2-\mu_1}$ goes to zero. In other words the isothermal compressibility, the mechanical stability indicator in one component solution, is no longer a unique quantity in binary mixtures. Besides mechanical instability, strong *concentration* fluctuations can lead to demixing, i.e. a separation of the system into phases of different concentration. In this case $(\partial^2 f/\partial x^2)_{T,v}$ is a material stability indicator that diverges as the instability boundary is reached and the corresponding primary stability indicator is provided by $(\partial^2 g/\partial x^2)_{T,P}$. Except in special cases, both mechanical and material instabilities will in general appear simultaneously.

3.2.3 Main fluctuations driving the instability

In order to determine to which degree the instability is driven mainly by largest mechanical or material fluctuations (i.e. density-density or concentration-concentration fluctuations) it is useful to consider the diagonalization of the stability matrix f through, this time, an orthogonal change of basis [Chen and Forstmann, 1992]. In this case the eigenvalues are given by:

$$\lambda_\pm = \frac{1}{2}tr[f] \pm \frac{1}{2}\sqrt{tr[f]^2 - 4det[f]} \tag{3.25}$$

and the normalized eigenvectors can be written:

$$\mathbf{z}_\pm = \begin{pmatrix} x_\pm \\ y_\pm \end{pmatrix} \tag{3.26}$$

with:

$$\begin{aligned} x_\pm &= 1/\sqrt{1 + \left[\frac{f_{vv} - \lambda_\pm}{f_{vx}}\right]^2} \\ y_\pm &= -x_\pm \frac{f_{vv} - \lambda_\pm}{f_{vx}} \end{aligned} \tag{3.27}$$

In this orthogonal basis the quadratic forms can be expressed as:

$$\delta f^2 = \lambda_+ \delta\eta_1^2 + \lambda_- \delta\eta_2^2 \tag{3.28}$$

with the $\delta\eta_i$ obtained as linear combinations of the fluctuations in volume and concentration:

$$\begin{aligned} \delta\eta_1 &= x_+\delta v + y_+\delta x \\ \delta\eta_2 &= x_-\delta v + y_-\delta x \end{aligned} \tag{3.29}$$

The instability can be characterized defining the angle α

$$\alpha = arctan\left(\frac{x_-}{y_-}\right) \tag{3.30}$$

with the argument that simplify to

$$\frac{x_-}{y_-} = -\frac{f_{vx}}{f_{vv} - \lambda_-} \tag{3.31}$$

When an instability is reached, the stiffness matrix becomes singular (3.24) and the determinant $det[f] \equiv \lambda_-\lambda_+$ vanishes, condition that is independent of the basis chosen to diagonalize the quadratic form. The border of a stability region is thus indicated by the smaller eigenvalue λ_- going to zero:

$$\begin{aligned} \lim_{\lambda_- \to 0^+} \frac{x_-}{y_-} &= -\frac{f_{vx}}{f_{vv}} \\ &= -\frac{f_{xx}}{f_{vx}} \end{aligned} \tag{3.32}$$

These relations state for $[f]$ non diagonal ($f_{vx} \neq 0$). In the particular case where $f_{vx} = 0$, fluctuations in density and volume fraction will just be independent. With this definition of α, the instability will be predominantly of demixing type when α is close to 0 and of condensation type when α is close to $\pm\pi/2$.

3.2.4 Phase coexistence: the binodal

Within our approach we do not have access directly to the coexisting (binodal) surface. In order to build the whole coexisting surface we have to pass through the determination of (all) the coexisting phases and related tie lines in the system. Two phases (I and II) coexist if the pressure and the chemical potential of each species (1 and 2) are equal in both phases, i.e:

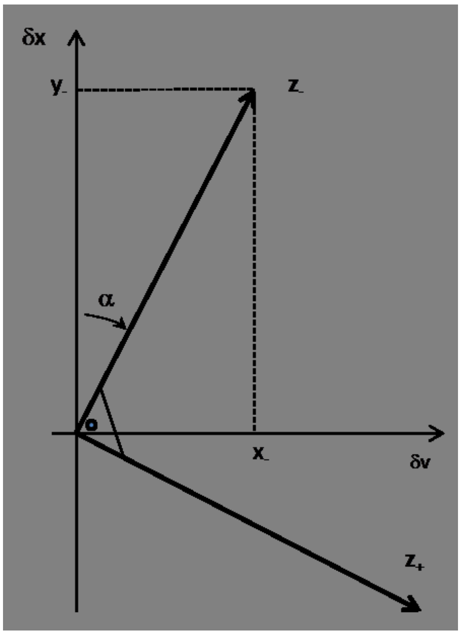

Figure 3.1: *Schematic view of the orthonormal vectors* $\boldsymbol{z}_{\pm}$ *and the stability indicator* α*. The instability will be predominantly of demixing type when* α *is close to* 0 *and of condensation type when* α *is close to* $\pm\pi/2$

$$
\begin{aligned}
P^{(I)} &= P^{(II)} \\
\mu_1^{(I)} &= \mu_1^{(II)} \\
\mu_2^{(I)} &= \mu_2^{(II)}
\end{aligned}
\tag{3.33}
$$

We use a Newton-Raphson algorithm to solve these equations and compute the binodal. At a critical point, the tie lines that join coexisting phases become the tangent to the curve bounding the instable region. This condition can be expressed as:

$$f_{xxx} - 3f_{xxv}(\frac{f_{xv}}{f_{vv}}) + 3f_{xvv}(\frac{f_{xv}}{f_{vv}})^2 - f_{vvv}(\frac{f_{xv}}{f_{vv}})^3 = 0 \tag{3.34}$$

The critical lines are then computed by determining on the spinodal surface the loci where this condition is satisfied.

3.3 The symmetric binary mixtures

In this section we will use the free energy obtained from first order thermodynamic perturbation theory to investigate the phase diagram of symmetric binary mixtures as a function of δ, the unlike to like interaction ratio. The microscopic interaction between the component consists in a hard core repulsion plus attractive Yukawa potential with a screening length $z = 1.8$. In the last years, numerous authors have studied the phase behaviour of symmetrical binary mixtures using liquid state theory or computer simulations, but their investigations have been limited to the equimolar plane of the phase diagram (x=1/2) [Wilding et al., 1998; Antonevych et al., 2002; Scholl-Paschinger and Kahl, 2003]. From these investigations, different topologies of phase behaviour have been obtained and they are in agreement with the mean field predictions. The values of δ marking the exact boundaries between the different topologies depend on the degree of accuracy of the theory considered. Indeed, the key issue is the capability to account for the long-range fluctuations that are important for the description of critical phenomena and phase separation.

Relatively few studies of the more general case of non equimolar concentrations can be found in the literature. Only recently, insights into the complexity of the entire phase diagram of the symmetric binary mixture have been obtained using the Hierarchical Reference Theory (HRT) [Pini et al., 2003]. This highly accurate theory introduces long range density and concentration fluctuations via a renormalization-group like procedure where the long wavelength Fourier components of the microscopic interaction are gradually introduced in the Hamiltonian of the mixture [Parola and Reatto, 1985, 1991]. Their study was complemented with mean field calculations. The inclusion of long range fluctuations preserves the correct convexity of the free energy in the whole thermodynamic space, which is of particular relevance when one tries to determine the binodal surface. Whenever phase separation takes place, no instability domains are found as in the mean field approximation. The conditions of thermodynamic equilibrium are enforced by the theory itself and there is no need to impose the conditions of coexistence afterwards using a Maxwell construction (as described above).

A systematic investigation of the full phase diagram for one of the archetype of the symmetric binary mixture phase diagram, based on the Mean Spherical Approximation (MSA) and complemented with Grand Canonical Monte Carlo (GCMC) simulations, has also been recently presented [Köfinger et al., 2006]. Even if MSA is less accurate than advanced liquid state theories, particularly in the critical regions, semiquantitative agreement with the MC simulations was obtained. Their study confirmed in a more detailed way the results obtained previously via HRT and MF.

The next challenging step in this field is certainly to extend the study of the symmetric binary mixture to encompass the more general case of asymmetric mixtures. HRT is already very laborious to implement for the symmetric mixture and is also computationnaly expensive. Moreover its generalization for non symmetric binary mixture is not straightforward. The convergency of the semi-analytical MSA is also not guaranteed when moving to binary mixtures highly asymmetric in size. For these reasons we calculated the free energy from first order perturbation theory to study the phase diagram of binary mixtures. As a first step, we validate the perturbative approach using the previous results on the symmetric binary mixtures. In this way the accuracy of PT, which is expected to be slightly inaccurate in the critical regions, can be tested also on binary mixtures whose phase diagrams have been already determined from advanced liquid state theory [Pini et al., 2003]. This step is certainly necessary since, up to now, PT has been only used to compute the phase diagram of one component systems. We will show that the main topologies of phase diagram are correctly reproduced within PT also for binary mixtures. This study is a first step towards the investigation of more sophisticated mixtures. Indeed, the final goal of this work is the determination of the phase diagram of the model crystallin proteins mixtures that we derived in Chapter 2. Beside the interparticle interactions, the peculiarity of the α-γ mixture is also the important size ratio between the two crystallin proteins ($d_\alpha/d_\gamma = 4.53$). Thus, among the numerous parameters that can be varied in a binary mixture (range, depth or strength of the different interactions, size of the components, kind of potential, ...) we choose to extend the study of the symmetric binary mixtures by considering mixtures with increasing diameter ratios $\Delta = d_2/d_1$. Starting from the different archetypes of phase diagrams known for the symmetric case, the effect on the phase behaviour when increasing Δ will also be studied.

3.3.1 Model

The particles interact via the Hard Core Yukawa (HCY) pair potential $u_{ij}(r)$. The interaction between like particles is the same ($u_{11} = u_{22}$), while unlike particles have a weaker energy of interaction $u_{12}(r) = \delta u_{ii}(r)$, with $\delta < 1$. The HCY potential has been adopted in several studies of the symmetric mixtures based on the Self-Consistent Ornstein Zernicke Approximation (SCOZA) [Scholl-Paschinger and Kahl, 2003], MSA [Köfinger et al., 2006] or HRT [Pini et al., 2003]. The particles are additive hard spheres and their attractive tail is given by an attractive Yukawa potential:

$$u_{ij}(r) = \begin{cases} \infty & \text{if } r \leqslant d_{ij}, \\ -\epsilon_{ij} d_{ij} e^{-z(r/d_{ij}-1)}/r & \text{if } r > d_{ij} \end{cases} \tag{3.35}$$

The parameters ϵ_{ij} and z, define the energy scale and the range of the interactions respectively. The inverse range of the interaction has been fixed to z=1.8 for both like and unlike species. This value of the screening length has been used by the authors in the aformentionned studies on HCY symmetric binary mixtures [Scholl-Paschinger and Kahl, 2003; Pini et al., 2003; Köfinger et al., 2006]. Indeed, it has been shown that HCY potential provides a reasonable description of simple fluid for $z = 1.8$, as well as colloidal suspensions, where typically $z \gg 1$. The symmetric binary mixture is composed of particles that have the same size $d_{11} = d_{22} = d_{12} = d = 1$. In a second step, mixtures of particles with size ratio $\Delta = d_2/d_1$ different from one will be considered. In that case $d_{11} = d = 1$ is kept fixed while the size of the second component is increased ($d_{22} > d$ and $d_{12} = 1/2(d + d_{22})$).

3.3.2 Phase behaviour at x = 1/2

The phase diagram of symmetric binary mixtures has been first studied focusing on the particular plane of equal species concentration (x=1/2) [Wilding et al., 1998; Scholl-Paschinger and Kahl, 2003]. In this simplified case, when the parameter δ varies from 0 to 1, three different topologies of phase diagrams, arising from the competition between gas and mixed-fluid (G-MF) transition and demixing transition, have been observed and classified. The mean field phase diagram at equal species concentration presents both a first-order coexistence boundary between a low density fluid and a high density one, and the so called λ line of mixing demixing critical points: when crossing the λ line, the fluid demixes into two phases of same density but with concentrations $\overline{x}$ and $1 - \overline{x}$. Depending on the loci where the λ line crosses the G-MF transition, three types of phase diagrams have been defined (archetypes I,II and III) [Wilding et al., 1998; Scholl-Paschinger and Kahl, 2003; Pini et al., 2003]. This classification is based on the projection of the phase diagram on the $x = 1/2$ plane. The calculation of the phase diagram on the whole $x - \rho$ plane reveals the presence of two subtypes for the archetype II of phase diagrams [Köfinger et al., 2006] as it will be shown.

We will present now the phase diagrams of symmetric binary mixtures we obtained from perturbation theory: we start with the description of the three different topologies of symmetric phase diagrams based on their projection on the $x = 1/2$ plane. These diagrams are presented in Fig. 3.2.

Type I at x=1/2

The first topology corresponds to high values of δ ($\delta_1 < \delta < 1$ with $\delta_1 = 0.708$ within mean field) and is depicted in the upper left panel of Fig. 3.2 for $\delta = 0.8$: at low temperature (T_1 on the figure) a gas at $x = 0.5$ coexists with two demixed fluids of same density but opposite relative composition ($\overline{x}$ and $1 - \overline{x}$). Indeed, when crossing the λ line, the system separates into a component 1-rich phase and a component 2-rich phase. The coexistence between a gas and a mixed fluid (that we will call now on a liquid-vapor LV coexistence) is also present, but metastable with respect to the previous one. At higher temperature (T_2) the gas and the homogeneous fluid ($x = 0.5$) coexist and their coexistence curve ends into a liquid-vapor critical point (CP). The λ line intersects the L-V coexistence curve well below the L-V critical point at T_{CEP}, in what appears to be a *critical end point* (CEP), i.e a point where a critical liquid coexists with a non critical gas. The presence of a CEP has been obtained by different authors within MF and SCOZA calculations [Pini et al., 2003; Scholl-Paschinger and Kahl, 2003]. However, the determination of the critical lines on the whole $\rho - x$ space will asses, as we will show in the next sections, that this is not a critical end point, in agreement with HRT and modified hypernetted chain (MHNC) calculations [Pini et al., 2003; Antonevych et al., 2002].

Type III at x=1/2

By decreasing δ, the propension of the mixture to demix is enhanced, and the L-V coexistence curve moves to lower temperature. At small δ ($0 < \delta < \delta_2$, with $\delta_2 = 0.605$

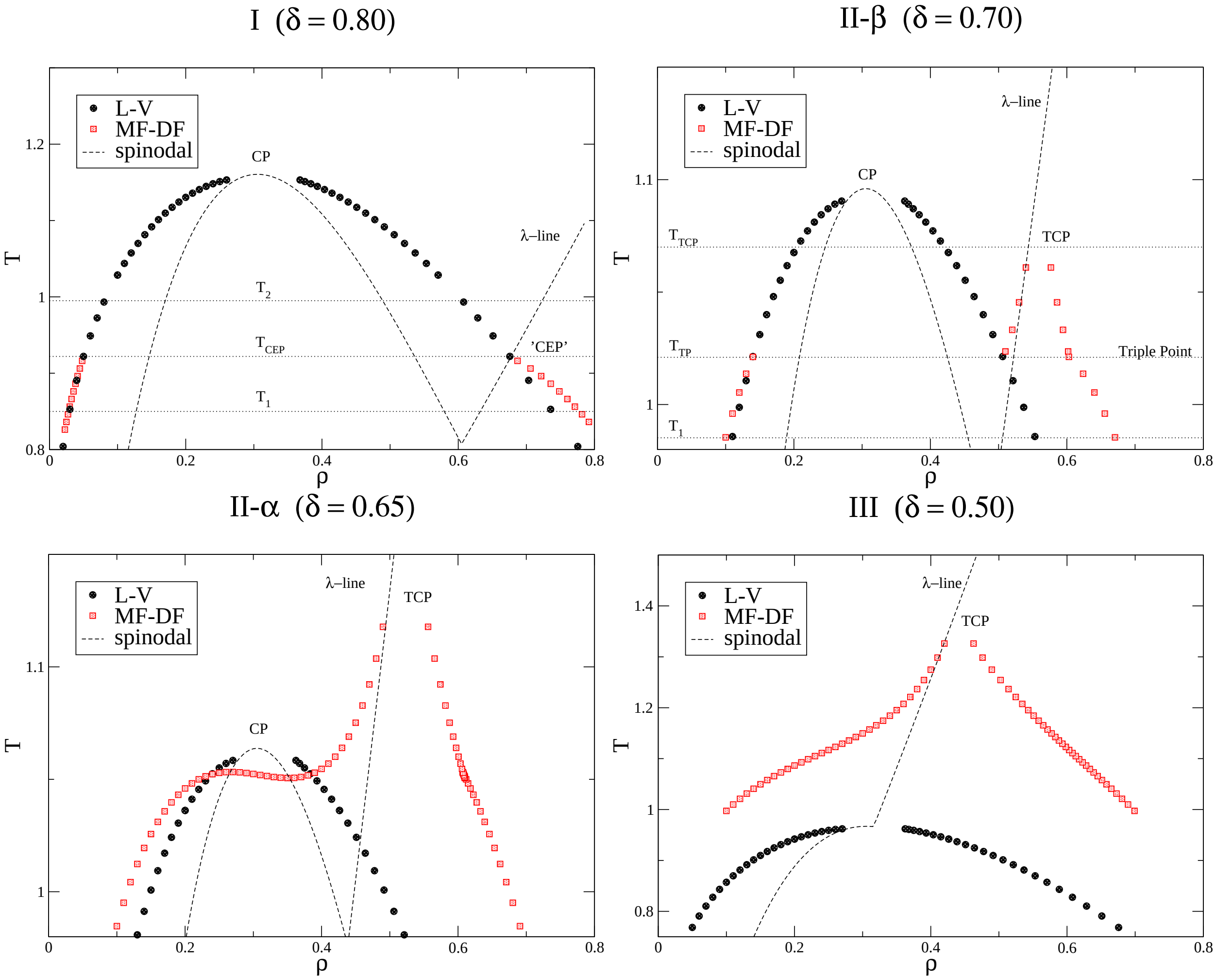
I (δ = 0.80)

II-β (δ = 0.70)

II-α (δ = 0.65)

III (δ = 0.50)

Figure 3.2: *PT phase diagram of the symmetric binary mixture at* $x = 0.5$ *representing the possible topologies of phase diagrams (I,II-*α*, II-*β *and III for* $\delta = 0.8, 0.65, 0.7$ *and* 0.5 *respectively). Beyond the* λ*-line, the fluid demixes in two phases of same density but with concentrations* $\overline{x}$ *and* $1 - \overline{x}$*. Depending on* δ*, critical points (CP), critical end points (CEP), tricritical points (TCP) and triple points (TP) can occur. The tendency for the solution to demix is enhanced when lowering* δ*.*

within MF) the point at which the coexistence curve intersect the λ line coincides with its critical point. Critical point means here: the locus where the homogeneous low density gas become critical. This point is called tricritical point (TCP): on approaching it from low temperature, the simultaneous coalescence of three phases is observed, namely a low density and homogeneous gas and two demixed high density fluids. There is now no first order L-V transition between the gas and the mixed fluid (the corresponding coexistence curve being metastable) and also no L-V critical point. This topology of phase diagram is shown in the lower right panel of Fig. 3.2 for $\delta = 0.5$.

Type II-α and II-β at x=1/2

Intermediate topology (type II) is found in a narrow interval ($\delta_2 < \delta < \delta_1$). An example is presented in the upper right panel of Fig. 3.2 (subtype II-β with $\delta = 0.7$). At low temperature, T_1, an homogeneous gas coexists with two demixed fluids, as in archetype I. The λ line intersects the L-V coexistence just below the critical point of the L-V transition, which is also present as in type I. At T_{TP}, we observe the occurrence of a triple point where a gas, a mixed liquid at intermediate density and a 1-rich and a 2-rich liquid at high density coexist. By increasing the temperature up to T_{TCP}, the homogeneous liquid and the two demixed fluid become critical at the same tricritical point (as in type III). A second subtype (II-α) is also found for slightly lower δ and the phase diagram is drawn on the lower left panel of Fig. 3.2 ($\delta = 0.65$). Except for the relative location of the TCP with respect to the CP, the distinction between the II-α and II-β subtypes is not possible from the x=1/2 cuts, but the difference will become clear when considering the phase diagram on the entire $x - \rho$ space and the connection between the different critical lines, as we will see in the next sections.

Accuracy of PT for the symmetric binary mixture

Before moving to the determination of the phase diagram on the whole $x - \rho$ plane we will test the accuracy of PT in predicting the critical loci of the symmetric binary mixture.

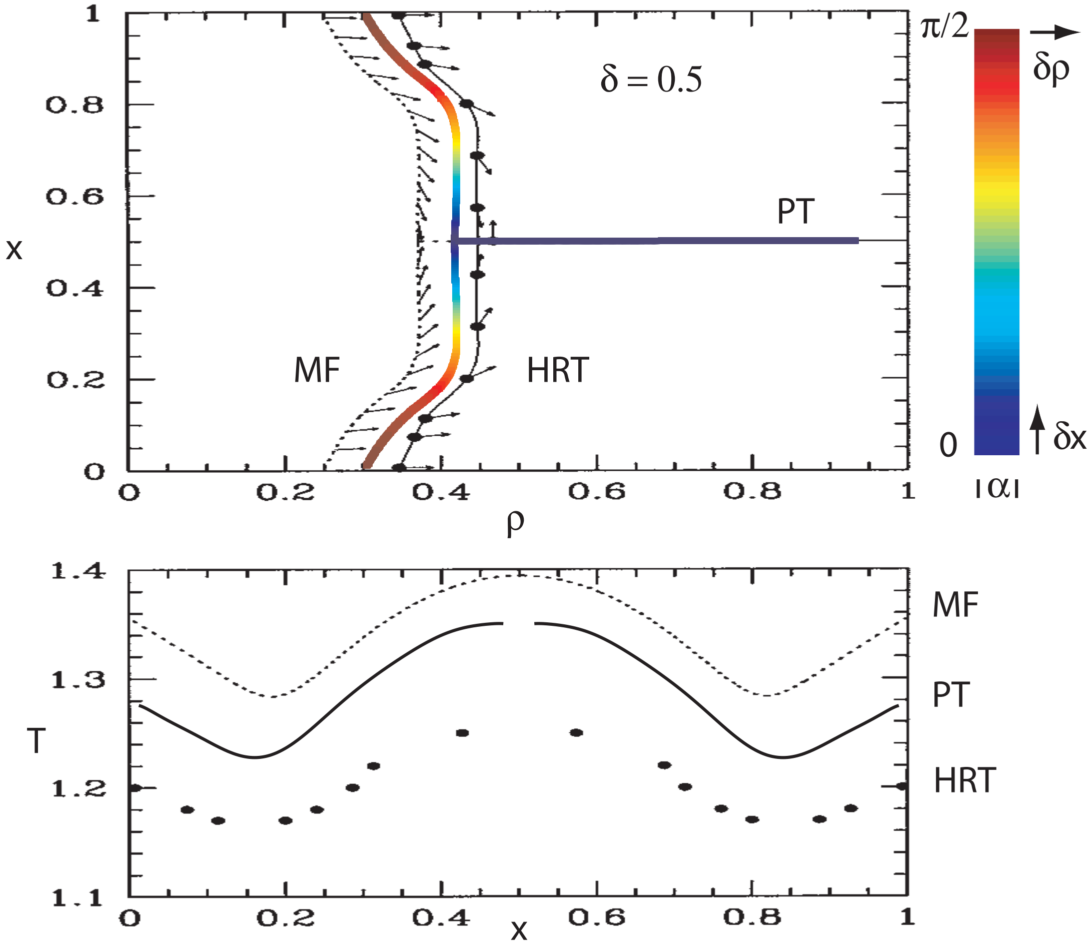

Figure 3.3: *Projection of the critical lines in the $\rho - x$ plane (upper panel) and $x - T$ plane (lower panel) for $\delta = 0.5$ as obtained from perturbation theory, HRT and MF calculations. The PT critical lines lay in between MF and the more accurate HRT results in both projections. The stability indicator α is also drawn on the PT critical line ($0 < |\alpha| < \pi/2$). For $\alpha = 0$, fluctuations in concentration x are driving the phase separation and demixing is found, as observed at x=1/2. When $|\alpha| = \pi/2$, the system becomes critical because of density fluctuations and L-V transition occurs, as found in the one component limits ($x = 0$ and $x = 1$).*

Fig. 3.3 shows the projections of the HRT, MF and PT critical lines on both the $\rho - x$ and the $x - T$ planes for type III phase diagram ($\delta = 0.5$). This value of δ is small enough to give the same topologies of the critical lines in HRT, mean-field theory and also PT. The PT critical lines are found to fall in between the results of HRT and MF. For the pure species, it is known, from the comparison with accurate simulation data for the critical point of the Yukawa fluid with the same $z = 1.8$ inverse range considered here [Pini et al., 1998b], that PT underestimates by about 10% the critical density and overestimates by about 5% the critical temperature. It has been shown that HRT provides a very good determination of the critical point for Lennard-Jones like fluids [Parola and Reatto, 1995] and we found for the critical loci of the binary system the same differences between PT and the accurate HRT, as for the pure fluid case. The relative long range of the attraction (z=1.8) is responsible, at least in part, for this accuracy: it is well known that the error within PT on the location of the critical density for one component systems become smaller and smaller when the range of the potential increases [Vega et al., 1992]. But our results provide an evident improvement with respect to others mean field theories and PT is certainly a valuable method to study the phase behaviour of binary mixtures.

The stability indicator α, defined in Fig. 3.1, which indicates the kind of fluctuations that are driving the phase separation process is also drawn on the critical line in Fig. 3.3. For the pure one component solutions, fluctuations in density ($|\alpha| = \pi/2$, red) are leading to $L - V$ phase separation, while at $x = 1/2$, along the λ-line, pure fluctuations in concentration ($\alpha = 0$, blue) are responsible for the demixing of the solution. The value of α, which gives the direction of the order parameter of the transition, will be drawn also in the next figures on the different critical lines, using the same definition for the colours associated with the possible values of α as presented in Fig. 3.3..

3.3.3 Phase behaviour in the $x - \rho$ plane

We will describe now the phase behaviour of symmetric binary mixtures on the whole $x - \rho$ plane. The critical lines and the phase behaviour of the different type of phase diagrams that were defined in the preceding section will be determined. We start the investigation by a careful study of subtype II, thus focusing on the set of interparticle strength for which the phase diagram at equal concentration exhibits both a liquid-vapor critical point and a tricritical point. MSA results for this topology of phase diagrams showed two possible subtypes [Köfinger et al., 2006]. Following the definitions introduced by these authors, we present now a detailed study of subtype II-β. The other phase diagrams will be then also presented, but more briefly.

Phase diagram of type II-β

The phase diagram of type II-β is depicted in Fig. 3.4. Four critical lines CL_i can be distinguished. Each critical line spans along a well defined coexistence surface S_i. CL_1 is the λ line, the critical line of the symmetrical demixing surface S_1 present at high density. At the tricritical point, CL_1 bifurcates and gives raise to two critical lines, CL_2 and CL_3, that cross the surfaces S_2 and S_3 (composed of the green small dots). These critical lines terminate in critical end points (CEP) when reaching the fourth coexistence surface S_4 which spans along the whole concentration range. CL_4, the critical line related to S_4, connects the pure component liquid-vapor critical points and is totally disconnected from the λ line. Some other aspects of the phase behaviour of the subtype II-β (cuts of the spinodal surface at different temperature and the stability indicator on the critical line) are also depicted in the upper right panel of Fig. 3.5.

The critical lines presented on Fig. 3.4 were obtained solving eq. 3.34 on the instability surface. Using this efficient method to compute the critical lines, we found two peculiar

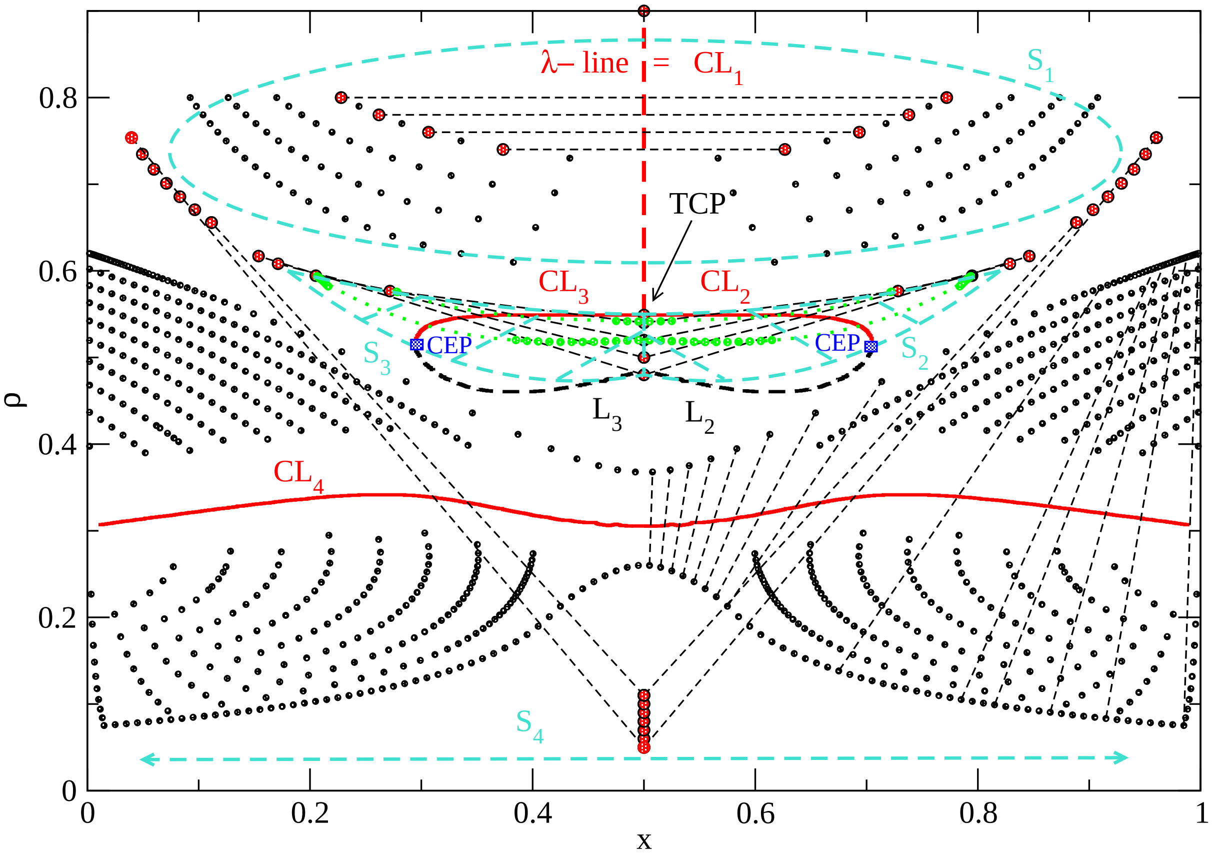

Figure 3.4: *Projection of the PT phase diagram of the $\delta = 0.7$ symmetric binary mixture onto the $x - \rho$ plane. The critical lines (CL_i) are drawn in red and the 4 coexistence surfaces (S_i) are represented schematically in light blue dashed lines. In order to obtain the coexistence surface, we calculated coexisting states (two or three phases can coexist). Some tie lines joining the coexisting phases are drawn (dash thin lines). The green dots (and green line) are coexisting phases that join at CL_2 and CL_3, and the critical end points (CEP) of CL_2 and CL_3 are also drawn (blue squares). The dashed red line is the mixing-demixing λ line (CL_1). The dashed lines (L_2 and L_3) are solution of Eq. 3.34 but located below the coexistence surface. The large red dots represent the triple line.*

critical loops at intermediate concentration and density, made of CL_2, CL_3 and of two low density branches (L_2 and L_3). In a second step, the coexistence surfaces were determined and, from the extrapolation of the coexistence points, we verify the location of the critical lines previously calculated. In this way, we found that CL_2 and CL_3 ends in CEP, while L_2 and L_3 are located below the coexistence surface S_4 and, thus, are metastable. It is still not clear to us why L_2 and L_3 appear like critical lines, but we note a very good correspondence between these lines and the location in the $x - \rho$ plane of two *triple lines* in MSA calculations [Köfinger et al., 2006]. These triple lines were defined by the intersection of coexisting surfaces (in this case where S_4 intersect S_2 and S_3). The triple lines are not critical lines, but they are located on the binodal surface. A possible explanation could be that the condition of tangency of the tie lines to the unstable region, which is explicited in Eq. 3.34, is fullfilled at the intersection of two coexistence regions when, in addition, the instability surface is located very close in temperature to the binodal surface, as it is the case here.

Phase behaviour of the remaining type (II-α, I and III)

A second subtype of phase diagram II has been also defined and is depicted in the lower left panel of Fig. 3.5 for $\delta = 0.65$: for this subtype II-α, the λ line bifurcates at the tricritical point into two critical lines which pass through minima and connect to the liquid-vapor critical points of the pure phases. This, indeed, is in contrast with subtype β where CL_4, the critical line arising from the pure component critical points, is totally disconnected from the λ line, and it leads to the distinction between the two subtypes. Within PT the transition between the two topologies is found around $\delta = 0.6694$.

A peculiar solution for the loci of critical points is obtained for subtype α as well. In that case, a loop of points, solution of Eq. 3.34, is found around $x = 0.5$, but, from the analysis of the coexistence points, only the lower part corresponds to a critical line, in

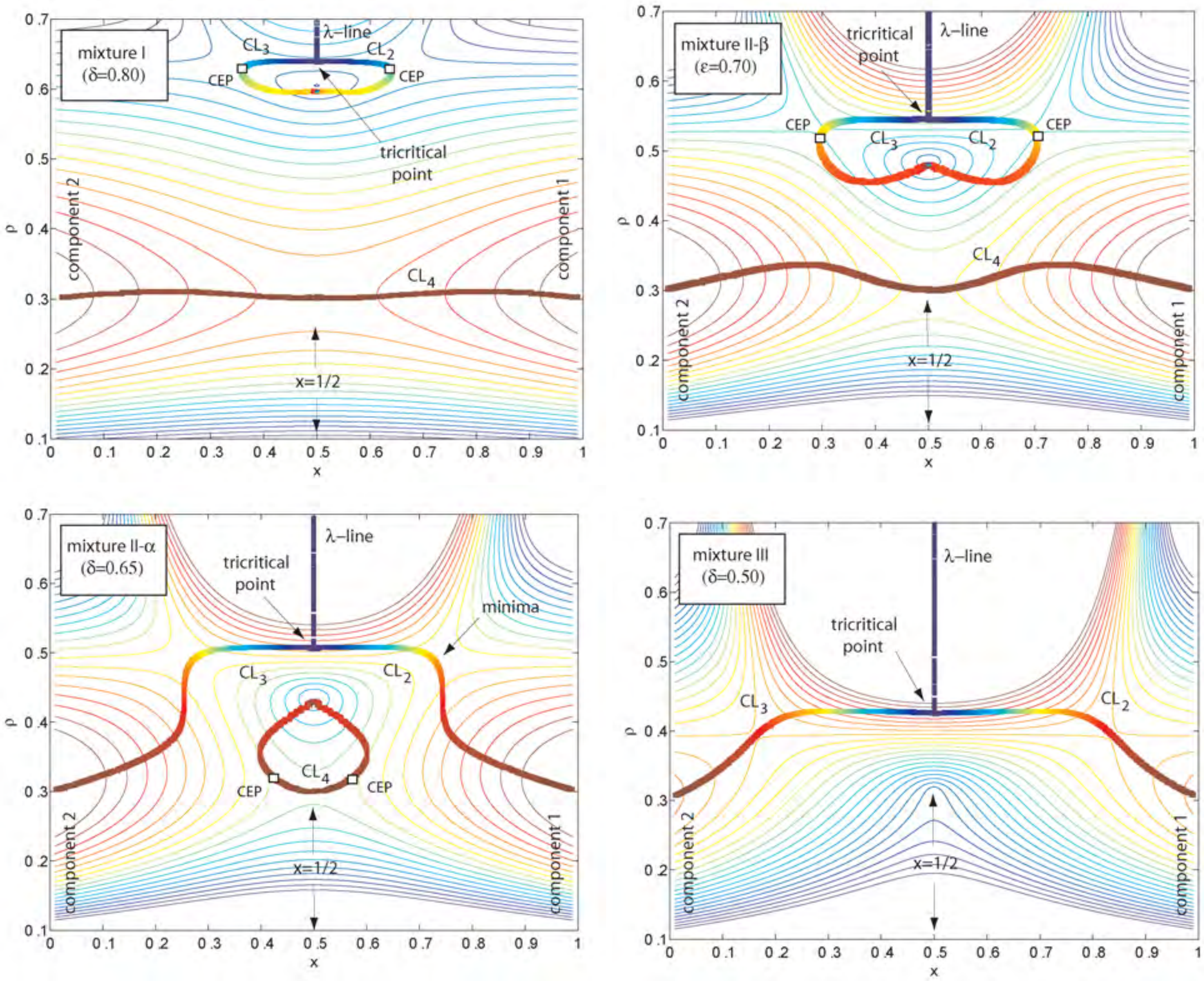

Figure 3.5: *The four different archetypes of phase diagrams for the symmetric binary mixture are depicted ($\delta = 0.8, 0.7, 0.65, 0.5$). The projection of the critical lines onto the $x - \rho$ plane and cuts of the instability surface for different temperatures (0.8 to 1.24 by steps of 0.02) are shown. The transition between the two subtypes of topology II ($\delta = 0.70$ and $\delta = 0.65$) is found around $\delta = 0.6694$. The critical end points are represented by small squares. The value of the stability indicator α on the critical lines is also shown (according to the scale introduced on Fig. 3.3).*

agreement with the MSA study [Köfinger et al., 2006]. Thus, the determination of the spinodal and the critical loci from Eq. 3.34 is certainly a very efficient tool to map the topology of the phase diagram but it should be complemented by the computationally more involved determination of the coexisting points. The necessity of computing also the set of coexisting points and tie lines will become crucial when dealing with more complex binary mixtures. We will show that for the α-γ crystallin mixture a slight change in the mutual attraction between the two components lead to a completely different composition of the coexisting phase, while the spinodal instability and even the coexistence surface have almost the same shape. Thus, if the location of the instability boundary (a high/low temperature) depends strongly on the mutual attraction, the composition of the coexisting phases will be even more sensible to $u_{\alpha\gamma}$.

Phase behaviours corresponding to the remaining topologies (type I and III) are also depicted in Fig. 3.5. Interestingly, from the calculations of the critical lines for the $\delta = 0.8$ case, it appears that the λ-line does not end in a CEP at x=1/2, contrary to what the analysis at $x = 1/2$ tends to show. The mixture is still in the intermediate regime (II-β), with the occurrence of a tricritical point and the presence of very tiny coexistence surfaces (S_2 and S_3) and their connected critical lines. We do not observed the clear occurrence of a CEP at x=1/2 up to $\delta = 0.9$, the central loops made of CL_2, L_2 and CL_3,L_3 becoming just narrower. These results are in qualitative agreement with studies based on HRT and MHNC which did not find the presence of critical end point at equimolar species up to at least $\delta = 0.8$ [Pini et al., 2003; Antonevych et al., 2002]. For higher δ, the intermediate coexistence surfaces become so small that their presence is very difficult to assess. Instead, simulations performed on square well potentials found the CEP characteristic of topology I already at around $\delta = 0.7$ [Wilding et al., 1998]. Thus, the specific interaction used in the model might play a role on the phase behaviour of the symmetric mixture, at least when sophisticated liquid state theories like HRT are considered.

The important conclusion we can draw at this point, is that the phase diagrams of the binary symmetric mixtures are well reproduced by perturbation theory and we can rely on it to investigate the phase diagrams of more realistic mixtures, as it will be done in the next chapter for the α-γ protein mixture. The space of parameters of binary mixtures is extremely wide and a systematic investigation is certainly not within the scope of this thesis. Nevertheless we have discussed the qualitative and quantitative predictive power of PT and demonstrated that this method provides a clear improvement with respect to standard MF approaches. Our final goal is to describe the phase behaviours of a few specific mixtures of simple interacting components, in the framework of the mixtures derived for the α and γ crystallin proteins. One particularity of this system is certainly the important asymmetry between the diameter of the two components. As a first step in this direction, we will study the effect, on the phase diagram, of introducing an asymmetry $\Delta = d_2/d_1$ into the binary mixtures.

3.3.4 Asymmetric binary mixtures with $d_1 \neq d_2$

In this section, we present an overview of the phase behaviour of the different phase diagram topologies presented above when introducing a slight asymmetry in the diameter of the two components. The spinodal instability and the critical lines are determined for the different mixtures and give a first insight into their phase diagram. This study should be complemented by a more careful determination of the coexistence surfaces which will also asses the location of the true critical lines and critical end points. The goal is here to test our numerical approach towards non symmetric mixtures.

We consider the same HCY interaction between the two components (3.35) as for the symmetric case. The inverse screening length is kept fixed ($z = 1.8$) and we only increase the diameter of the second component d_2. In this way, the effective range of interaction between the components of kind 2 is reduced, and the critical point of the pure mixture of component 2 should move correspondingly to lower T and higher ϕ when increasing Δ. However, for the HCY with $z = 1.8$ the change in the range of the second component is almost negligible: for the highest ratio $\Delta = 1.25$ considered in this study, the location of the critical point changes by less than 0.2% with respect to $\Delta = 1$. Thus, changes to the phase behaviour of the binary mixtures observed when increasing Δ are caused essentially by the size asymmetry and not by the change in the interactions between the components.

Phase behaviour of type II-α

For subtype II-α, two interesting features appear when Δ increases and the symmetry with respect to $x = 1/2$ is broken (Fig. 3.6). First, the λ line of the demixing transition is connected to the liquid vapor critical point of the pure solution of the smallest component only, as soon as $d_1 \neq d_2$, forming a single critical line denoted by CL_2 on the panels with $\Delta \neq 1$. The critical line CL_3 of the second and bigger component ends in a critical end point at intermediate density and composition, near the locus where the λ line bifurcates into CL_2 and CL_3 at $\Delta = 1$. The determination of the exact location of this end point would require the computation of the coexistence points (for the reasons explained above). Second, as d_2 increases further, the critical line CL_3 arising from the critical point of the pure large component mixture extends towards lower densities and, at around $\Delta = 1.15$, detached from its intermediate density branch (CL_{3B}) to join the critical line that comes from the liquid vapor critical point at $x = 1/2$ and that was already present in the case of the symmetric mixture. This gives raise to a new critical line CL_{3A} as shown on the lower left panel. The small coexistence surface around CL_{3B} is present at $\Delta = 1.15$ but will disappear at larger asymmetry.

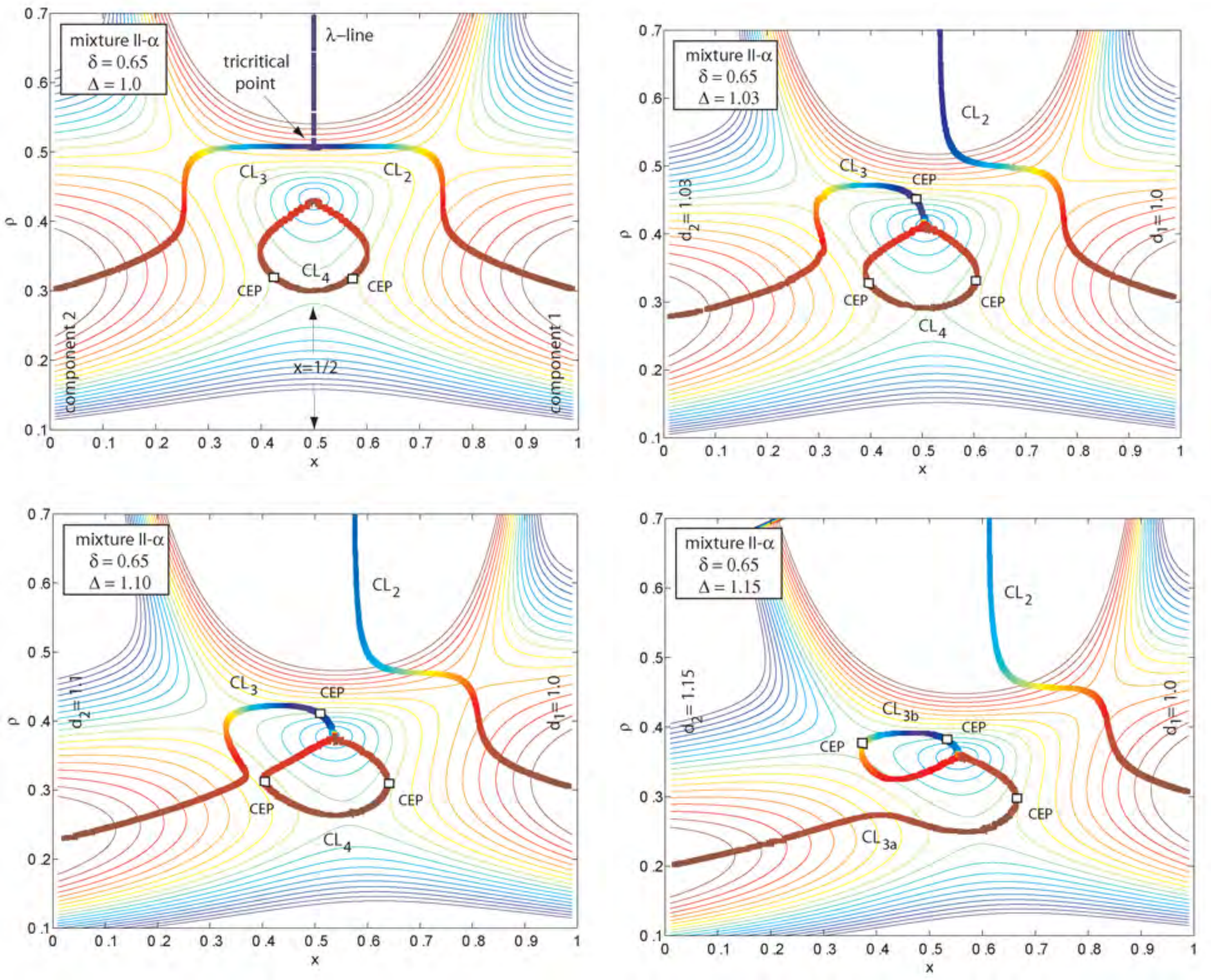

Figure 3.6: *Phase behaviour of type II-α phase diagram* ($\delta = 0.65$) *of the symmetric mixture for different* $\Delta = d_2/d_1$ *ratios. The projection of the critical lines onto the* $x - \rho$ *plane and cuts of the instability surface for different temperatures (0.8 to 1.24 by steps of 0.02) are shown for* $\Delta = 1, 1.03, 1.1, 1.15$ *as indicated on the panels. The* λ*-line of the demixing transition is connected to the LV critical point of the pure small component solution* ($x = 1$) *for* $\Delta > 1$. *The squares are estimates of the critical end points* CEP *locations.*

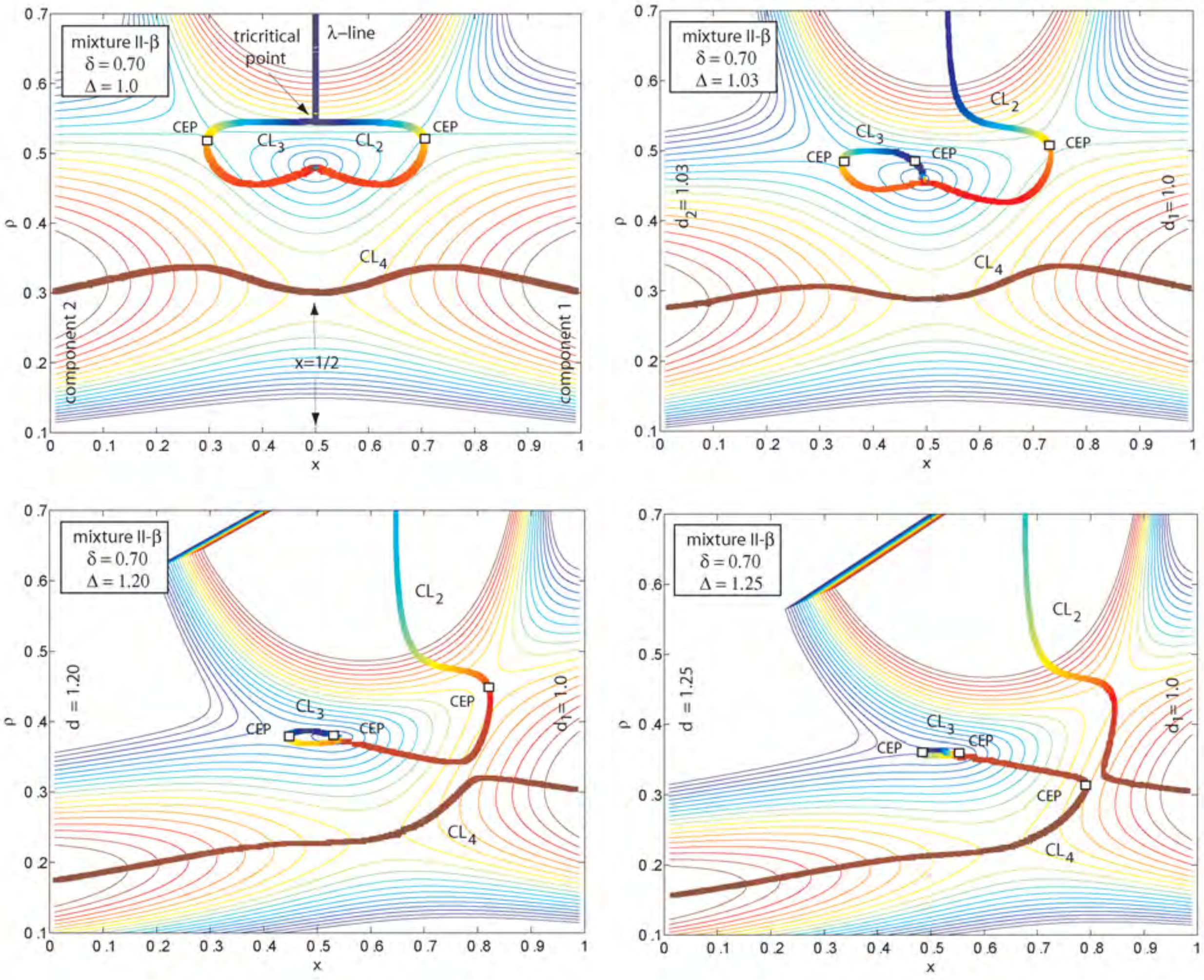

Figure 3.7: *Phase behaviour of archetype II-β phase diagram ($\delta = 0.7$) of the symmetric mixture for different $\Delta = d_2/d_1$ ratios. The projection of the critical lines onto the $x - \rho$ plane and cuts of the instability surface for different temperatures (0.8 to 1.24 by steps of 0.02) are shown for $\Delta = 1, 1.03, 1.2, 1.25$ as indicated on the panels. The squares show the critical end points (CEP). For $\Delta = 1.25$ the λ line connects the LV critical point of the pure small component solution ($x = 1$).*

Phase behaviour of type II-β

The phase behaviours for subtype II-β are depicted in Fig. 3.7. For $\Delta \neq 1$, the λ line detaches from the critical line CL_3 that crosses the coexistence surface S3 for the symmetric mixture (as defined on Fig. 3.4) and connects to CL_2 only. This critical line, called now on CL_2, expands when increasing Δ towards lower densities and larger x (i.e. towards the pure mixture of small components), coming closer and closer to CL_4 which, in turn, exhibits a strong bending (see the kink around $(x, \rho) = (0.8, 0.3)$ in the $\Delta = 1.20$ panel). Moreover, the detached CL_3 has now two critical end points. At $\Delta = 1.25$, the critical point of the pure small component mixture finally connects to CL_2 and CL_2 expands finally from the former λ line present at $\Delta = 0$ to the pure mixture of component 1, as it is found in the α subtype for $\Delta > 1$. The critical line CL_3 is still present but will disappear for larger Δ.

The phase behaviours for $\delta = 0.8$ are presented in the upper panels of Fig. 3.8. We observe qualitatively the same phase behaviour as for type II-β, as expected from the study of the symmetric mixture.

Phase behaviour of type III

The phase behaviour of type III is less rich and interesting than the previous ones (see lower panels of Fig. 3.8). The critical point of the pure solution of large particles is totally disconnected from the λ line as soon as $\Delta > 0$ and a critical end point is present. The λ line connects to the LV critical points of the pure solution of small components (CL_2 on the lower left panel).

In conclusion, we observed that for sufficiently large asymmetry (the value of Δ required depends on δ) the λ-line always connects the critical point of the smallest component pure mixture and never the critical line of the large component. Because of the attrac-

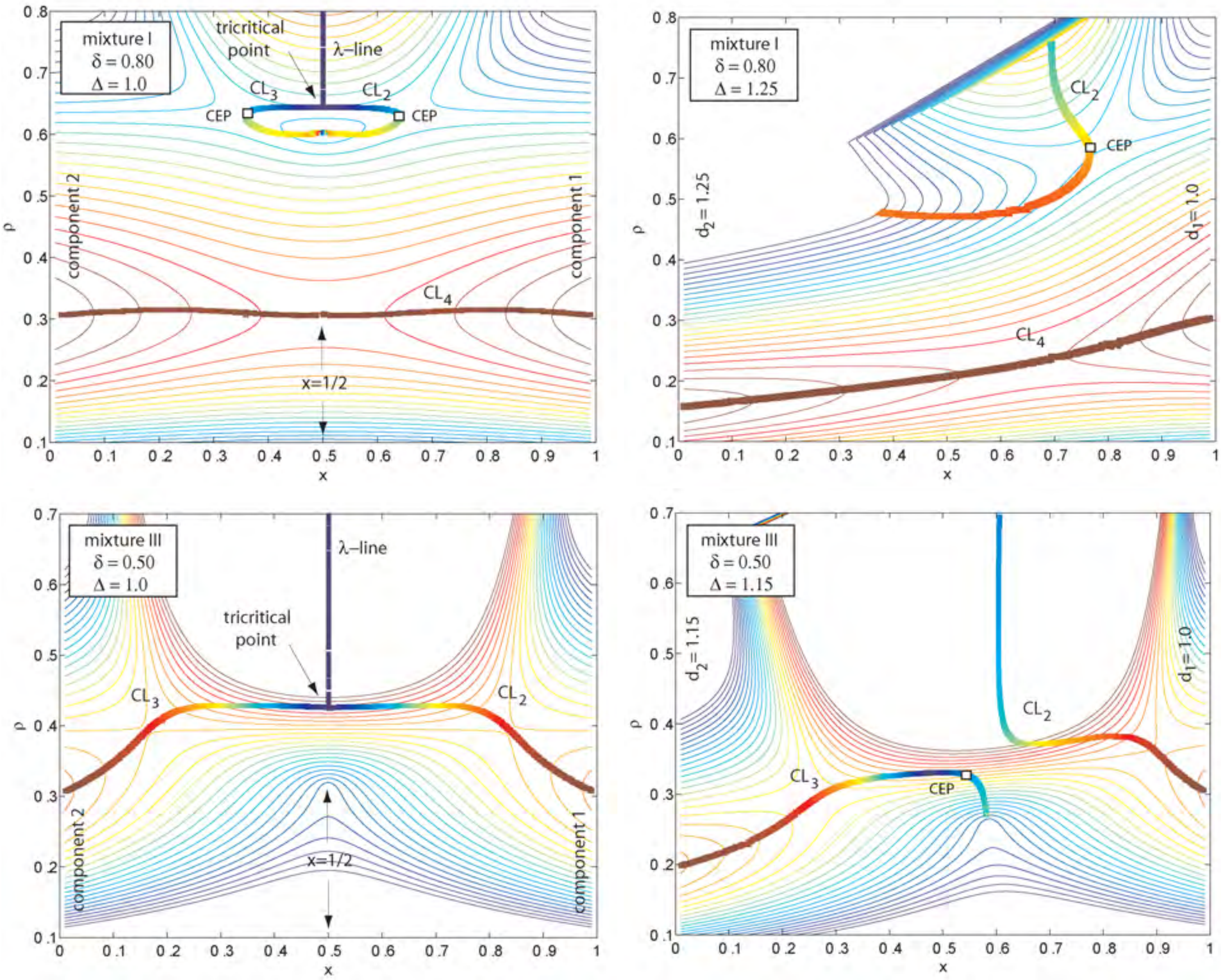

Figure 3.8: *Phase behaviour of archetype III ($\epsilon_{ij} = 0.5$) is depicted in the lower panels for $\Delta = 1, 1.15$ (left and right respectively). The $\epsilon_{ij} = 0.8$ case is shown in the upper panels ($\Delta = 1, 1.25$, left and right respectively). The projection of the critical lines onto the $x - \rho$ plane and cuts of the instability surface for different temperatures (0.6 to 1.6 by step of 0.03 for $\epsilon_{12} = 0.8$ and 0.88 to 1.24 by steps of 0.02 for type III) are drawn.*

tive interaction between the particles, the system is expected to undergo a liquid-vapor transition for suitable x, ρ and T. This happens already in the symmetric case at low or high concentration x, where one of the components do not influence the L-V transition of the other species. Moreover, since $\epsilon_{ij} < \epsilon_{ii}$, the internal energy will tend to promote demixing between the two components. At sufficiently high density, the loss of entropy induced by demixing might be overcome by the increase in the internal energy. In that case, the system undergoes a mixing-demixing transition, as we observed in all symmetric mixtures investigated. In the case of $\Delta \neq 1$, the propension for the mixture to demix while increasing the concentration of the largest component becomes stronger and stronger with increasing asymmetry, for all values of ϵ_{12}. From the same argument we just mentionned, it is clear that when $d_2 > d_1$ and $\epsilon_{12} < \epsilon_{ii}$, the loss in internal energy when adding some components-2 to a solution of components-1 is more important than for the equal size case, since more energetically favorable $1-1$ contacts are lost. Thus, the tendency of the mixture to demix is enhanced and the corresponding critical line moves to higher concentrations and lower densities. Oppositely, the mixing-demixing transition is less favored in a solution made principally of the large components (at small x) when adding small components. The situation might change for large Δ ($\Delta \sim 5$), when depletion induced interactions between the largest components might also appear [Biben and Hansen, 1991; Louis, 2001].

3.4 Conclusions

In this chapter we used thermodynamic perturbation theory to study the phase behaviour of symmetric binary mixture interacting via a hard core Yukawa potential. We showed that PT is not only suited for describing the phase diagram of one component system but it accounts also well for the phase diagram of binary mixtures. The main topologies of the symmetric binary mixtures phase diagram were correctly reproduced within PT, in agreement with advanced liquid state theories, like HRT. We discussed also the qualitative and predictive capacity of PT and demonstrated that this method provides a clear improvement with respect to standard mean field approaches.

As a first step towards the asymmetric α-γ mixture of crystallin proteins ($d_\alpha = 4.53\, d_\gamma$) we showed in the last part of the chapter that perturbation theory can be straightforwardly extended to mixtures that are not symmetric in size. Interestingly, when the energy of interaction between unlike particles is weaker than the interaction between like particles ($\delta < 1$), the propension for a solution of two components to demix becomes stronger when the asymmetry $\Delta = d_1/d_2$ increases.

CHAPTER 4

Phase behaviour of the binary α-γ mixture of eye lens proteins

Summary

In this chapter we will apply perturbation theory and all the formalism presented in Chapter 3 to study the phase behaviour of the colloidal model of eye lens proteins derived in Chapter 2. The statistical-thermodynamic perturbation theory for α-γ mixtures is devised based on the coarse-grained model developed by comparison of molecular dynamics with experiment. The instability boundaries appear very sensitive to the strength of the attraction between the two proteins: in the case of either weak or strong attractions, these eye lens mixtures are thermodynamically unstable at much higher temperatures. Interestingly, attraction strengths that correspond closely to those of proteins isolated from the living lens fall right within the stable region of the phase diagram. This non-monotonic stability suggests new molecular mechanisms for eye lens opacification in cataract. Moreover,

the determination of the tie lines shows that a decrease in the $u_{\alpha\gamma}$ attraction between the crystallins is certainly the most probable mechanism which could destabilize the binary mixture and lead to the phase separation of α-γ crystallin mixtures. The resulting demixing of the binary mixture would produce dense and almost pure phases of γs. Since there are considerable evidences that in certain forms of cataract the condensed phase is enriched in γ-crystallins, the phase separation observed here is particularly interesting.

4.1 Introduction

In Chapter 2, we have presented the derivation of a coarse-grained model of aqueous α- and γ-crystallin mixtures based on Molecular Dynamics simulations (MD) and Small Angle Neutron Scattering (SANS) experiments performed at high protein concentrations [Stradner et al., 2007]. We showed that the stability of these high concentration crystallin mixtures depends strongly and in a non monotonic manner on $u_{\alpha\gamma}$: strong or weak attraction results in a spectacular enhancement of the forward scattering intensity. The fluctuations of density and/or concentration responsible for such strong forward scattering take place on length scales comparable to the light wavelength, leading to a loss of the transparency of these eye lens protein mixtures. These strong fluctuations are usually encountered when a thermodynamic instability boundary is reached and mixtures start to phase separate. We will study now the points where these fluctuations become unbounded, i.e. the spinodal surfaces. To do so, we will use the perturbative approach described in Chapter 3 and determine first the instability boundary of the binary mixture of crystallins as a function of the strength of the mutual attraction [Dorsaz et al., 2009b]. The derivation of statistical-thermodynamic perturbation theory for α-γ mixtures will be guided by the validated coarse-grained model developed by comparison of molecular dynamics with experiments. In a second step we will determine the binodal surface of the binary α-γ

mixture and the composition of the coexisting phases as a function of $u_{\alpha\gamma}$.

4.2 Spinodal surface

The instability or spinodal surface indicates the temperature T^* below which the binary mixture cannot exist as a homogeneous phase. Indeed, when crossing the spinodal, it becomes thermodynamically more favorable for the system to split in two or more coexisting phases. The spinodal surface provides an indication of the coexistence surface (the binodal) since the latter will be located at slightly higher temperature, except for critical lines, where binodal and spinodal merge.

The scattering intensities can be used as a qualitative estimate of how distant from the unstable region of the binary mixture the experimental conditions are: the pure γ solution is already highly critical, being just above the critical point. With addition of αs, keeping the temperature constant, the scattering intensity increases first ($C_\alpha = 0.12, 0.25$) but then fluctuations are suppressed by further addition of αs (see Fig. 2.1). Quite consistent with previous findings [Thurston, 2006], these data suggest that, by increasing the α concentration, the system first gets closer to the instability boundary and subsequently moves away from it.

From the simulations it appears, however, that this behaviour depends strongly on the value of the mutual attraction (see Fig. 2.6). It is important to test whether our perturbative scheme can reproduce this behaviour. If this is achieved, we will be able to study the stability of the system in the whole parameter space, something that cannot be achieved by experiments and MD simulations.

4.2.1 3D spinodal surfaces

We shall present our results in the (ϕ_α-ϕ_γ-T) space, where ϕ_α and ϕ_γ are the partial packing fractions defined as $\phi_\mu = \frac{\pi}{6}\, d_\mu^3\, \rho\, x\ (\mu = \alpha, \gamma)$. This is the best way to graphically represent the spinodal surface due to the strong size asymmetry of the mixture under study. Fig 4.1 shows the spinodal surfaces of three different mixtures corresponding to three values of the $u_{\alpha\gamma}$ attraction, $u_{\alpha\gamma}$=$0, 1, 2$. In order to compute the instability surface according to Eq. 3.17, we determined the derivatives of the Helmholtz free energy by finite differences up to 7 points. To better visualize the shape of the spinodal surfaces, we display in Fig. 4.2 several cuts at constant ϕ_α of the full diagram of Fig. 4.1.

Let us first consider the spinodal of the pure-γ mixture, i.e. a mixture of square well particles with range $\lambda_{\gamma\gamma} = 0.25 d_\gamma$. This is represented by the open dots on Fig. 4.1. In this one component limit, the condition of stability simplifies to $(\partial^2 f/\partial v^2)_T > 0$. We determine also the coexistence curve shown in the upper left panel of Fig. 4.2. We find a critical packing fraction $\phi_\gamma^{C_{PT}} = 0.236$ and a critical temperature $T_\gamma^{c_{PT}} = 0.895$, in agreement with previous studies which have shown that perturbation theory slightly overestimates T^c and the corresponding critical density [Schöll-Paschinger et al., 2005; Vega et al., 1992]. As expected, by gradually increasing ϕ_α, the spinodal surface always develops starting from the pure-γ spinodal curve ($\phi_\alpha = 0$), but, as we shall see, its shape will strongly depend on the value of the attraction between unlike species.

The peculiarity of the spinodal for the purely repulsive ($u_{\alpha\gamma} = 0$) mixture, presented in Fig. 4.1, is the strong enhancement of T^* upon increasing, even only slightly, ϕ_α. When this happens the stability boundary moves to higher temperatures. In particular, it appears clearly from the 2D-cuts presented in Fig. 4.2 that the destabilization is much more pronounced at high ϕ_γ. This seems to support the idea that, for the repulsive case, the instability is caused, at least in part, by the depletion interaction that was first encountered

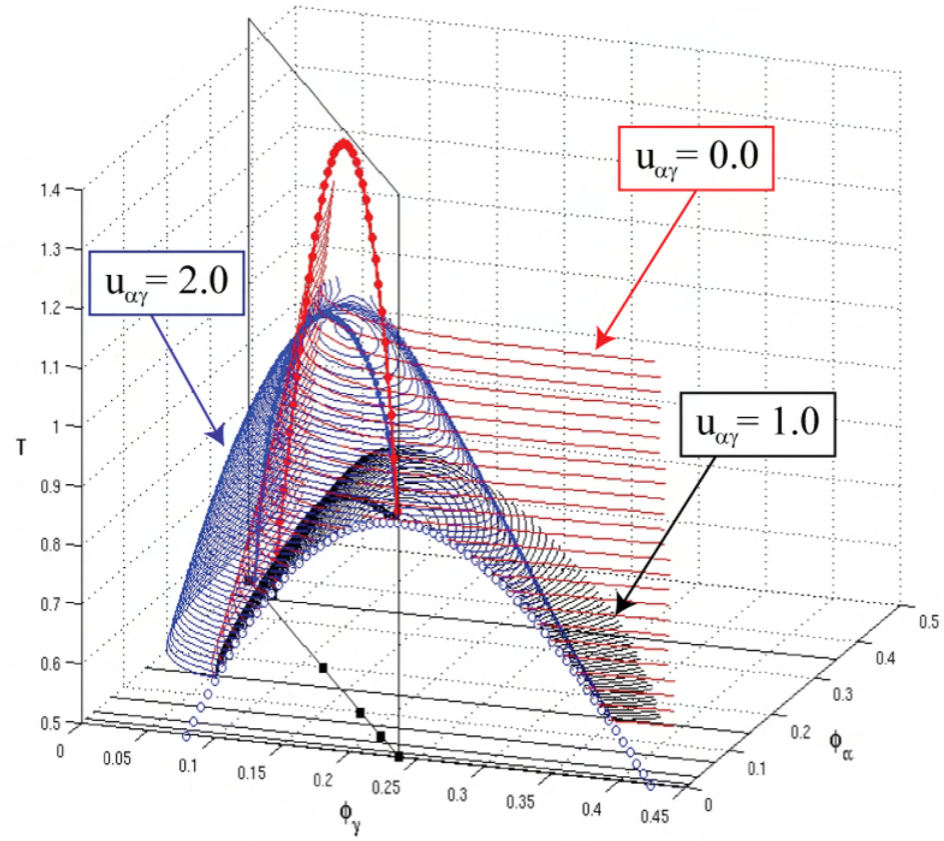

Figure 4.1: *Attraction between α and γ lens crystallins affects the thermodynamic stability of their concentrated mixtures in a non-monotonic fashion. The red surface shows the highly elevated spinodal for hard-sphere interactions between α and γ, while the black and blue surfaces show, respectively, the suppressed and then re-elevated surfaces for square-well depths* 1 *and* 2 k_BT. *The spinodal of the pure γ-mixture is also drawn (open dots). The lines at the bottom of the figure indicate ϕ_α values for the 2d-cuts of the stability boundary surface presented in Fig. 4.2. The dark squares correspond to the mixing ratios C_α of the mixtures on which the SANS experiments were performed and the experimental plane (dark rectangle) is also drawn.*

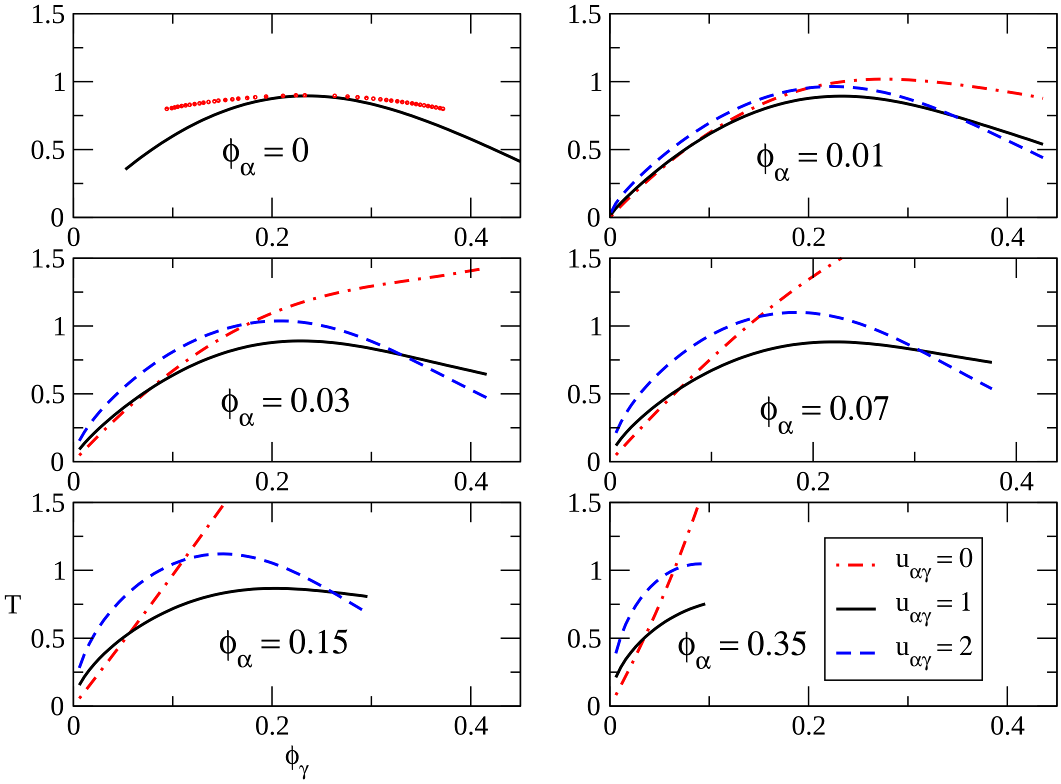

Figure 4.2: *2D-cut at constant ϕ_α of the instability surfaces for different values of the interaction $u_{\alpha\gamma} = 0, 1, 2$. The values of ϕ_α are indicated in each panel. The upper left panel shows the coexistence curve of the one component γ-mixture (dots) and the spinodal lines of the three mixtures are superimposed (dark line).*

in asymmetric hard sphere mixtures with size ratios larger than 5:1 [Biben and Hansen, 1991; Louis, 2001]. Depletion is an effective attraction of purely entropic origin between the larger components in binary mixtures with a strong size asymmetry. In particular, the strength of the attraction increases with the density of the small components and can even induce demixing between the two species. This looks very similar to the demixed configurations observed in the MD simulations in absence of interaction between α and γ crystallins (see Fig. 2.12). However, we will show in the following that the demixing is certainly enhanced by the α-γ size asymmetry, but more for energetic than entropic reasons. Moreover, we note that the $MCSL$ equation of state [Mansoori et al., 1971] used for the reference hard sphere mixture does not predict the coexistence of two fluid phases for binary hard sphere mixtures, even for size ratio larger than 1:5.

In the derivation of an effective interaction between α and γ crystallins consistent with the SANS data, we tried to stabilize the mixtures against the strong low q fluctuations observed in the MD simulations when modeling the interaction between the unlike crystallins as only repulsive, by introducing a small $u_{\alpha\gamma}$ attraction. Following the same line of reasoning as for the MD simulations, we introduce an interspecies attraction $u_{\alpha\gamma}$ with the same range as for the γ crystallins ($\lambda_{\alpha\gamma} = 0.25 d_\gamma$). The spinodal of a mixture with $u_{\alpha\gamma} = 1$ is represented in Fig. 4.1. This value of the attraction was found to be the one that most lowered the location of the stability boundary. The mixture remains stable at temperatures equivalent to the ones found for the pure γ mixture. The behaviour of the spinodal appears to be quite independent of the concentration of the larger components (see Fig. 4.2). Thus, the attraction efficiently counterbalances the propensity of the mixture to segregate and the demixing is reduced.

On further increasing the attraction, the spinodal surface moves again to higher temperatures but in a different way than for the hard sphere case. The occurrence of a very localized maximum at intermediate values of ϕ_α and ϕ_γ is observed in Fig. 4.1 for the instability surface of a mixture with $u_{\alpha\gamma} = 2$. Interestingly, the mixture is also more critical than the previous two at low ϕ_γ while no enhancement of the instability at high ϕ_γ is found (Fig. 4.2). This is not surprising since a strong interspecies attraction induces mechanical instability. In this case, the system tends to split into regions of very different density, similar to what is observed for the one component attractive case. At low density this tendency will be promoted, due to the free space available, while at high density the mixture is already highly packed and no additional effect will be observed.

4.2.2 Spinodals on the experimental plane

The SANS experiments have been performed by mixing different amounts of a pure-α solution ($\overline{\phi}_\alpha = 0.391$) and a pure-$\gamma$ solution ($\overline{\phi}_\gamma = 0.183$). The different mixing ratios $C_\alpha = 0, 0.125, 0.25, 0.5, 1$ are thus distributed along a line on the ϕ_α- ϕ_γ plane. In order to test the validity of our method, we investigate the instability with more attention to the cut of the parameter space represented by a plane in Fig. 4.1. As already discussed, perturbation theory tends to misestimate the location of the critical point. Then, to be consistent with the fact that the experiments took place near the pure-gamma critical point, we consider the pure γ solution to be at $\phi_\gamma^{C_{PT}} = 0.236$, i.e. the critical packing fraction as obtained from the theory, instead of $\overline{\phi}_\gamma$. In this way we are sure that the perturbation model for the pure γ-solution is indeed at the critical density.

The instability boundaries on this particular cut of the parameter space are presented in Fig. 4.3 for different values of the $u_{\alpha\gamma}$ attraction. A specific trend emerges. With no or low interspecies attraction, the spinodal lines move quickly to high temperature when increasing the concentration of α's. This tendency is suppressed for intermediate values of the attraction and for $u_{\alpha\gamma} = 1$ the spinodal temperatures of the mixtures are always lower than $T_\gamma^{c_{PT}}$. As expected, the spinodal lines move again to higher temperature for stronger interactions.

From these calculations, we notice that with an attraction around $u_{\alpha\gamma} = 0.5$ the best description of the experimental behaviour is obtained, i.e. a maximum of T^* between $C_\alpha = 0.125$ and 0.25 and a decrease of the spinodal temperature for the $C_\alpha = 0.5$ case, in very good agreement with the shape of the phase boundaries found previously for α-γ mixtures [Thurston, 2006]. This is also in agreement with the results from the MD simulations where an attraction $u_{\alpha\gamma} = 0.55$ gives the best agreement with the experimental data. With weaker attraction, a maximum of the instability temperature T^* is obtained

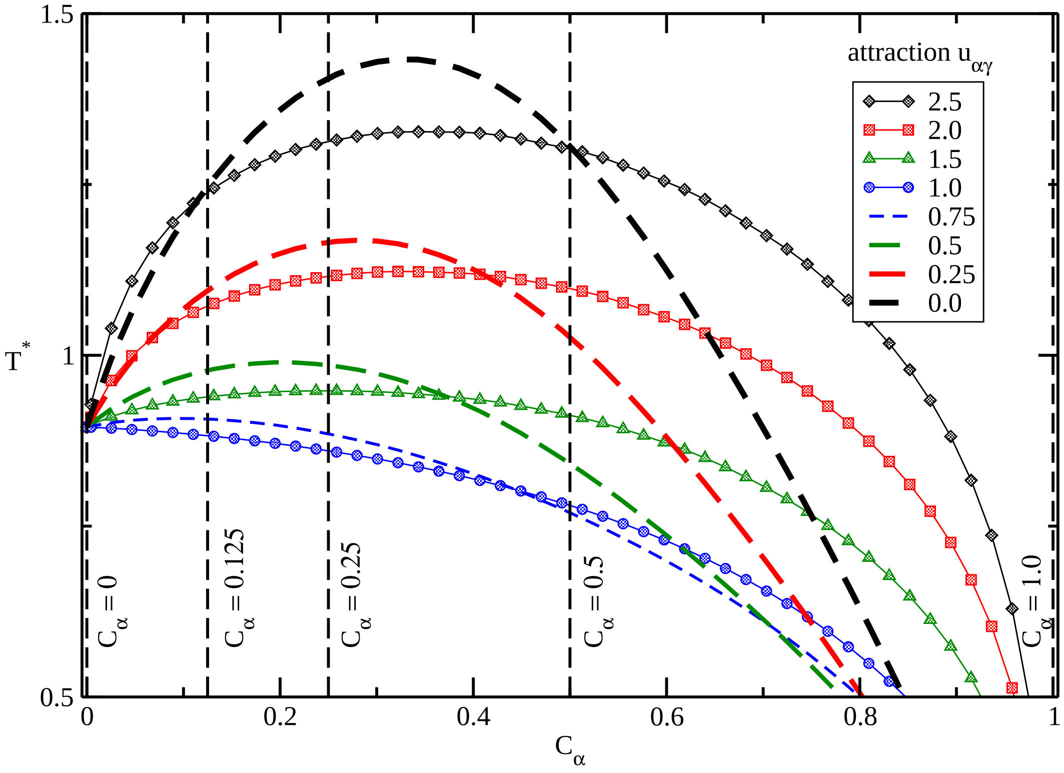

Figure 4.3: *2D-section of the instability surface on the experimental* $\overline{\phi}_\alpha$*-*$\phi_\gamma^{C_{PT}}$ *line drawn in Fig. 4.1. The temperature* T^* *at which the mixtures become unstable is presented as a function of the relative mixing ratio* C_α *for values of* $u_{\alpha\gamma}$ *ranging from the hard sphere limit up to* 2.5*.*

for $C_\alpha = 0.35$ and the mixture is still unstable for $C_\alpha = 0.5$. Increasing the interaction makes the mixture highly unstable for all $C_\alpha = 0.125, 0.25, 0.5$ and T^* is larger than T_γ^{cPT} for mixing ratios much beyond $C_\alpha = 0.5$.

With this theoretical approach we can extract the spinodal temperature T^*. Since the scattering intensity at low q will diverge approaching the instability boundary, we report T^* as a function of the $u_{\alpha\gamma}$ attraction for the different mixing ratios (Fig. 4.4) and confront it with the results of the MD simulations for the $C_\alpha = 0.5$ mixture, for which $I(q^* = 0.0467\,nm^{-1})$ as a function of $u_{\alpha\gamma}$ was plotted in Fig. 2.6. The same non monotonic behaviour as in the MD simulations is observed for all three mixtures. Moreover, the stability region that emerges from the simulations is in good correspondence with the minimum of T^* with respect to $u_{\alpha\gamma}$. From what we discussed above, it can be argued that while perturbation theory gives only a qualitative agreement for the location of the spinodal temperature and critical densities, it provides the right value of the interspecies attraction to reproduce the stabilization effect observed in the experiments and the simulations.

Now that the comparisons of the spinodals with the experimental and MD data have successfully validated the PT approach for the asymmetric α-γ mixture, we can reconsider the instability boundaries of the three mixtures previously studied ($u_{\alpha\gamma} = 0, 1$ and 2) and look at the point where the MD simulations for $C_\alpha = 0.5$ have been performed. The spinodals are represented in Fig. 4.5. For intermediate $\alpha - \gamma$ attraction strength, the simulated protein mixture is at temperatures well above the perturbation theory spinodal, consistent with the low forward scattering observed in the experiments and the MD simulations. However, as a consequence of the strong rise in the instability temperature for the mixtures with either no attraction ($u_{\alpha\gamma} = 0$) or strong attraction $u_{\alpha\gamma} = 2.0$, the simulation conditions turn out to be under the spinodal, within the unstable region[Dorsaz et al., 2009a]. Thus, with the calculation of the PT spinodals we formally assess that phase separation is responsible for the strong forward scattering measured in the simulations of the corresponding mixtures, as supposed in Chapter 2 and that a weak $u_{\alpha\gamma}$ attraction stabilizes the mixture against phase separation on the whole ρ-x plane. We note that the mixture with the lower stability boundary was presented here ($u_{\alpha\gamma} \simeq 1$), but, as we already shown, the description of the experimental behaviour is reproduced within PT with a weaker attraction ($u_{\alpha\gamma} \simeq 0.5$).

Our model gives good results for the spinodal of the binary mixtures and opens the possibility to explore the full phase diagram. In this sense, a special property of the $\alpha - \gamma$ mixture is that their phase separation process involves substantial segregation by protein

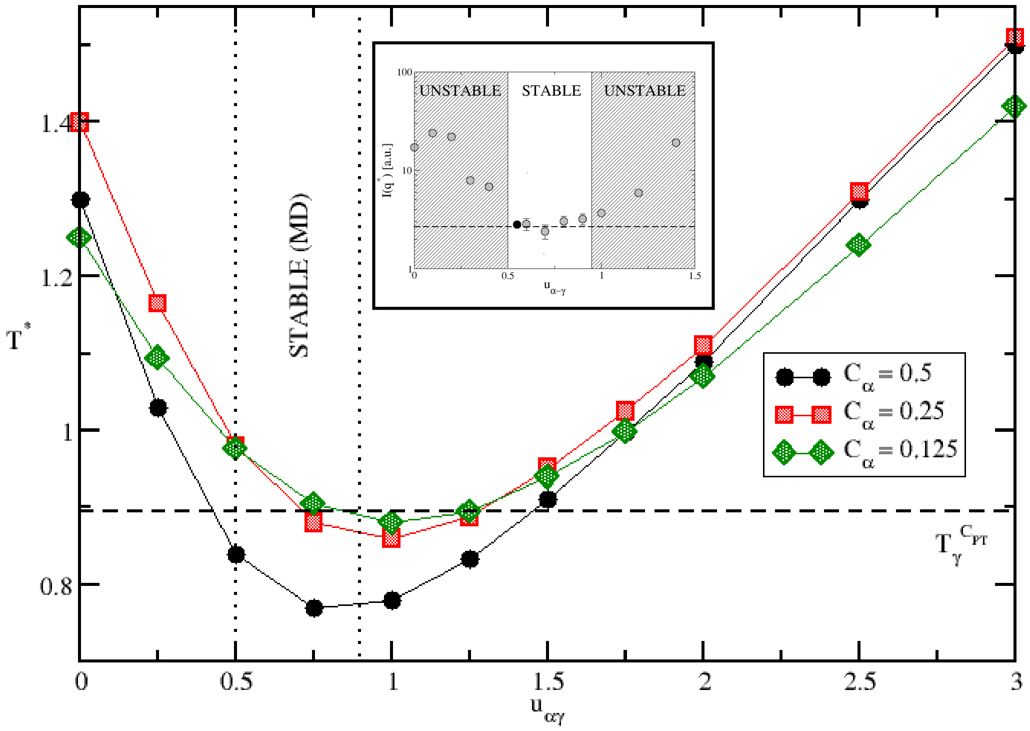

Figure 4.4: *Temperature of instability T^* as a function of the interaction strength $u_{\alpha\gamma}$ for the mixing ratios $C_\alpha = 0.125, 0.25, 0.5$ (dashed line on Fig. 4.3). The stable region obtained from the MD simulations for the $C_\alpha = 0.5$ case and the critical temperature of the pure γ-mixture (dashed line) are also drawn. Fig. 2.6 is reproduced in the inset for comparison: the dots are here the calculated scattering intensities at low q vector ($q^* = 0.0467\,nm^{-1}$) for the $C_\alpha = 0.5$ mixture.*

type, as well as by concentration [Thurston, 2006]. The experimental liquid-liquid phase separation tie lines indicate the coexistence of dilute phases, rich in α-crystallins, and dense phases with predominance of γ-crystallins. This gives rise to the tilted tie line pairs reported in Fig. 4.6 and taken from the experiments reported in Ref. [Thurston, 2006].

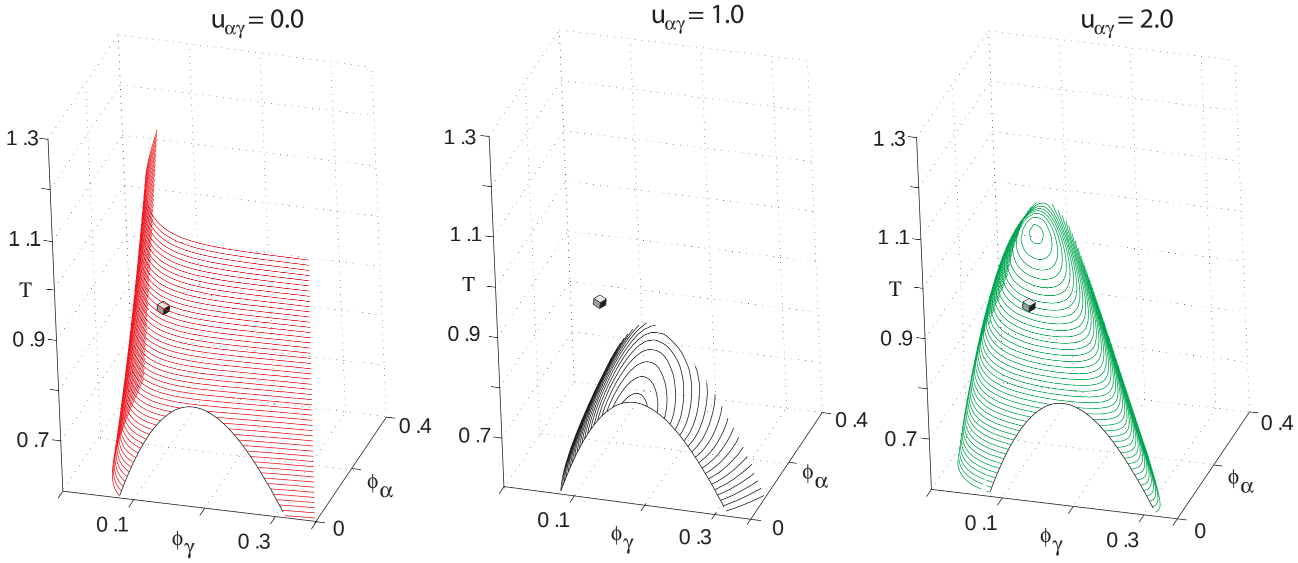

Figure 4.5: *The spinodal surface changes dramatically as the $\alpha-\gamma$ attraction strength, $u_{\alpha\gamma}$, increases. If $u_{\alpha\gamma}$ is slightly too low (left) or slightly to high (right), MD simulations (cube) that are otherwise appropriate for modeling $\alpha-\gamma$ mixtures (center) were found to be unstable. This finding is consistent with the fact that these unstable simulation conditions are indeed under the perturbation theory spinodals as shown.*

Until now we have limited our investigation to the spinodal stability of the mixtures. The spinodal is always located below the coexistence surface and can give already a valid indication of the shape of the tie lines. Cuts of the spinodal surface at a temperature slightly below the critical temperature of the pure-γ mixture are presented in Fig. 4.6. The perturbative spinodal surface with weak attraction seems compatible with the scenario of these extremely tilted experimental tie lines (see in particular the $u_{\alpha\gamma} = 0.5$ mixture). However, despite these encouraging results, the determination of the binodal surface is necessary to go a step beyond in the comparison of PT calculations with the experimental cloud point data available. It would be particularly valuable to understand how the $u_{\alpha\gamma}$ attraction affects the composition of the coexisting phases when the binary α-γ mixtures

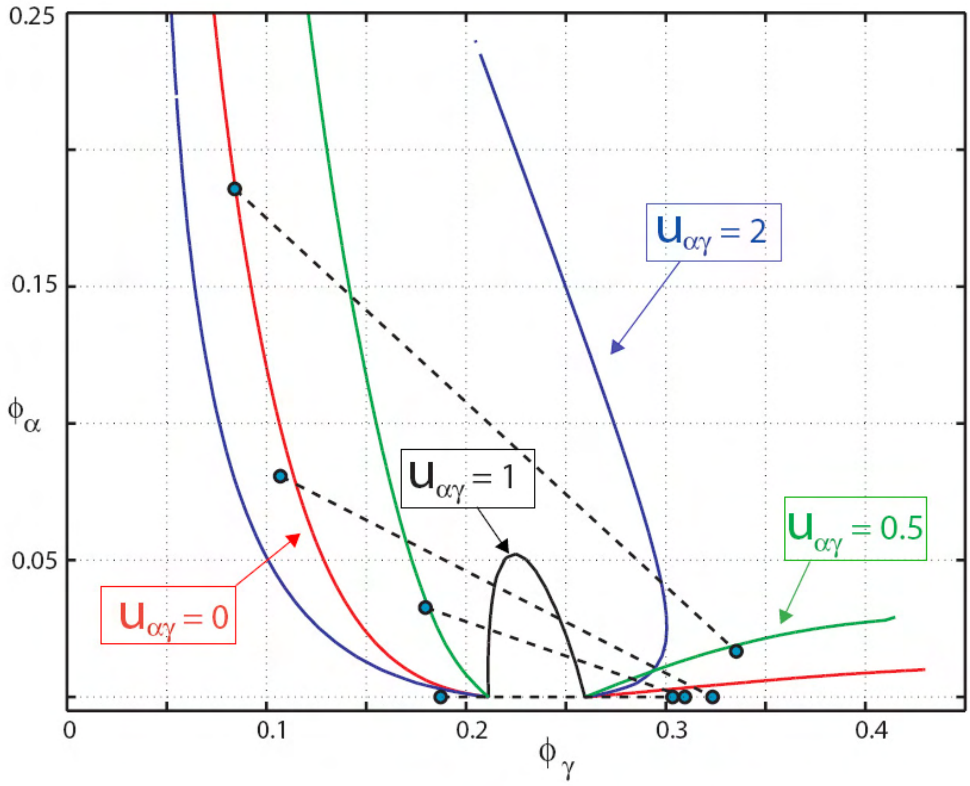

Figure 4.6: *2D-Cut of the spinodal surface at* $T = 0.98T_\gamma^{C_{PT}}$ *for* $u_{\alpha\gamma} = 0, 0.5, 1, 2$. *The experimental tie lines pairs (full circles and dashed lines) were taken from [Thurston, 2006].*

separate.

4.3 Coexistence surfaces and tie-lines

With the MD simulations presented in Chapter 2, we showed that for too weak or too strong $u_{\alpha\gamma}$ attraction, the mixtures phase separate already at high temperature, well above the critical temperature of the pure γ solution. In the last section, we demonstrated that the points in the parameter space that resulted unstable from MD are indeed located under the perturbation theory spinodals: the spinodal surface shifts from high to low temperatures depending on $u_{\alpha\gamma}$ in an extremely sensitive way. The cuts of the spinodal surface near $T_{\gamma}^{C_{PT}}$ gave us a first idea of the shape of the binodal (Fig. 4.6) but the composition of the coexisting phases has still to be determined. The latter is particularly relevant since we expect the composition to depend strongly on the attraction between αs and γs, and this could be compared with the composition of the pathological aggregates found in cataractous lenses [Lerman et al., 1966; Siezen et al., 1985].

As mentionned in Chapter 3, the conditions of coexistence have to be implemented afterwards within the perturbative scheme. The convergence of the Newton Raphson searching method that we use relies on good initial guesses for the coexisting phases, and, given the large size asymmetry of the $\alpha - \gamma$ crystallin mixture ($d_{\alpha} = 4.53 d_{\gamma}$), the initial starting point has to be really close to the solutions, especially in the limit of the pure γ solution, where the tie-lines connecting coexisting phases can be very tilted for some values of $u_{\alpha\gamma}$, as soon as ϕ_{α} increases. Moreover, the algorithm may fail to converge when approaching the critical points/lines, due to the flatness of the searching landscape and the limited numerical accuracy of the free energy and its derivatives . For these reasons, the set of critical points couldn't be calculated from Eq. 3.34 and were obtained, for a given temperature T, by extrapolation of the coexisting points at T.

We will determine now the exact shape of the coexistence surface and the composition of the coexisting states as a function of $u_{\alpha\gamma}$. To do so, we will focus on a particular set of mixtures. In the last sections, looking at the instability temperatures T^{*} of the different experimental mixing ratios C_{α} (Fig. 4.4) we found that the T^{*} were reduced for intermediate value of $u_{\alpha\gamma}$, in good agreement with the MD results which showed that the forward scattering of mixtures with weak $u_{\alpha\gamma}$ attractions is compatible with the forward scattering of the α-γ crystallin mixture. Furthermore, the calculation of the whole spinodal surface reveals that in a narrow range around $u_{\alpha\gamma} = 1$, the maximum in T^{*} is found at the critical point of the pure γ solution, the instability temperatures of the binary mixture

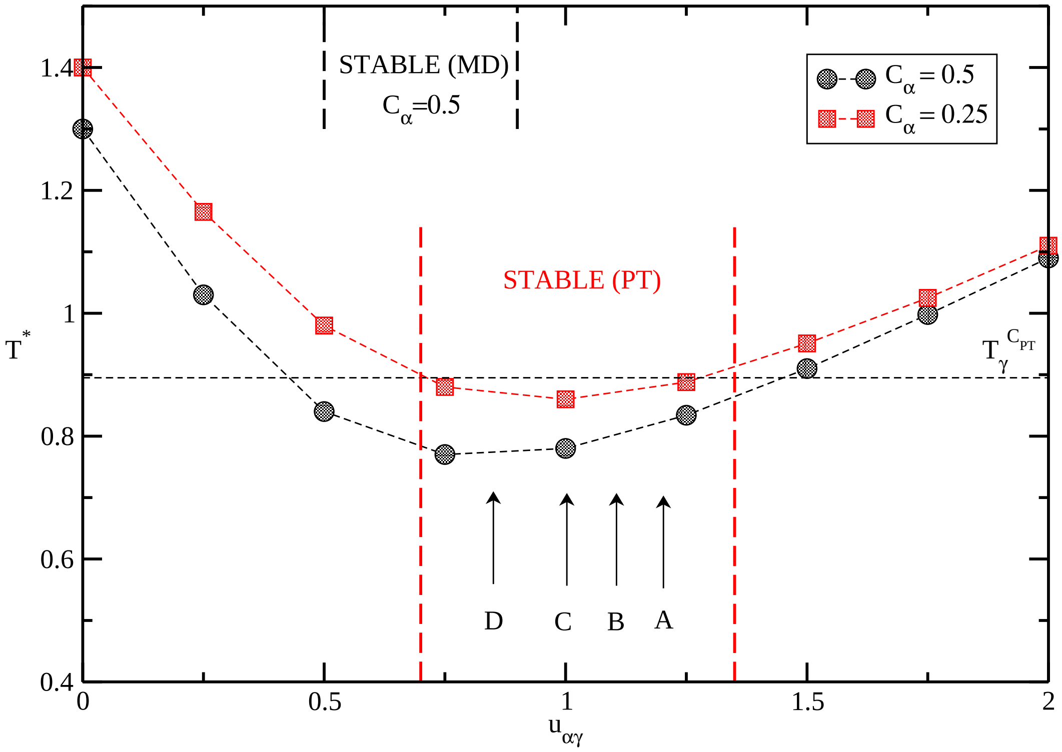

Figure 4.7: *The stability diagram presented in Fig. 4.4 is reproduced here: the instability temperature T^* as a function of the interaction strength $u_{\alpha\gamma}$ for the mixing ratios $C_\alpha = 0.25, 0.5$ (dashed line on Fig. 4.3) is shown. The stable region obtained from the MD simulations for the $C_\alpha = 0.5$ case and the critical temperature of the pure γ-mixture (dashed line) are also drawn. We investigate the coexistence surface of four different mixtures (denoted A, B, C and D with $u_{\alpha\gamma} = 1.2, 1.1, 1.0$ and 0.85 respectively). These $u_{\alpha\gamma}$ values fall in the stable region defined by the PT calculations of the spinodal surface, i.e. their instability boundary is located at very low temperature. Moreover, the spinodal of mixtures A, B and C is almost identical and the maximum spinodal temperature is found close to $T_\gamma^{C_{PT}}$ for all three mixtures.*

being always less than $T_\gamma^{C_{PT}}$.

We will consider now three of these highly stable mixtures labeled by A,B and C in Fig. 4.7, which have interaction strengths of $u_{\alpha\gamma} = 1.2, 1.1$ and 1.0 respectively. Their spinodals, presented in Fig. 4.8, are very similar and the maximum spinodal temperature is found close to $T_\gamma^{C_{PT}}$. This allows also a direct comparison of the cuts of the binodal surface since a quench performed at a particular temperature T would result at the same depth inside the instability region for all three mixtures. It will be shown that even if the difference in $u_{\alpha\gamma}$ is extremely tiny, their phase behaviour will be totally different. Cuts of the coexistence surfaces at temperature slightly below $T_\gamma^{C_{PT}} = 0.9$ for mixtures A, B and C are presented on Fig. 4.9. To facilitate the discussion, we define $(\phi_\alpha^I, \phi_\gamma^I)$ and $(\phi_\alpha^{II}, \phi_\gamma^{II})$ the composition of phases I and II, where the branch of coexisting states corresponding to phase I reaches the low density part of the pure γ spinodal (see Fig. 4.9). In a second step, the binodal of a fourth mixture, whose attraction is closer to the natural attraction between the α and γ crystallins, will also be studied (mixture D with $u_{\alpha\gamma} = 0.85$ on Fig. 4.7).

Binodal and tie lines of the stable mixtures

As presented on Fig. 4.8, mixtures A B and C have very similar spinodal surfaces. In Fig. 4.9 cuts of the coexistence surfaces at $T = 0.844$ show that the A, B and C binodals are almost identical as well. So, if for mixtures with larger differences in $u_{\alpha\gamma}$, we got a first insight into their different phase behaviour already from the spinodal calculation (as shown in the last section), for the small range of $u_{\alpha\gamma}$ we are considering now, even the determination of the binodal is not sufficient to understand what would be the composition of the three mixtures when they undergo phase separation. In order to show how the determination of the tie lines joining the different states is now essential to understand the phase separation process, let us prepare the three mixtures in the same high temperature and homogeneous state $(\phi_\gamma^0, \phi_\alpha^0) = (0.22, 0.075)$, as shown on Fig 4.9. When the A, B and C mixtures are quenched from this initial state to $T = 0.844$ (into their unstable region), they separate in totally different ways as illustrated by the corresponding TL_A, TL_B and TL_C tie lines in Fig. 4.9. The striking result is certainly the opposite tilt of TL_A and TL_C,

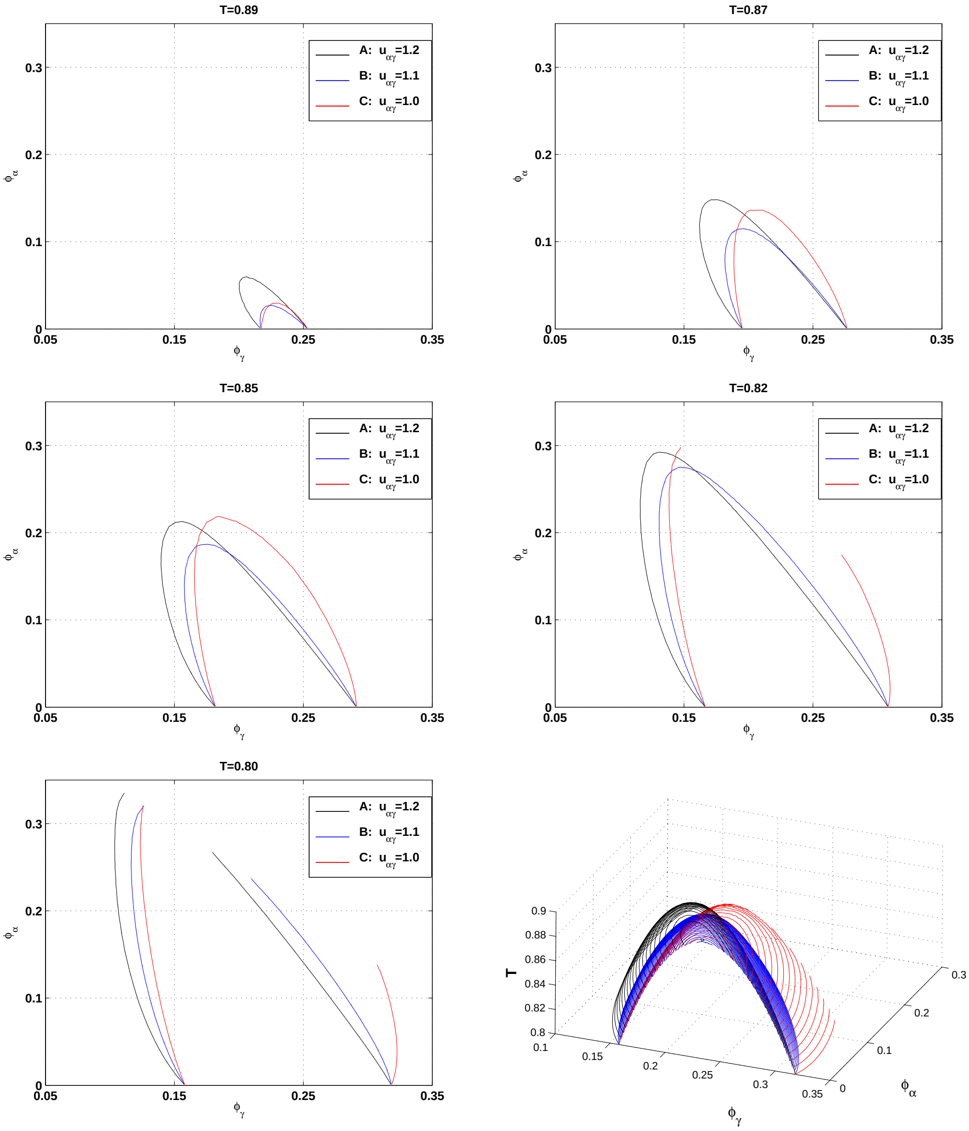

Figure 4.8: *Cuts of the spinodal surface for mixtures A-B-C defined in Fig. 4.7 (*$u_{\alpha\gamma} = 1.2, 1.1$ *and* 1.0 *respectively) at different temperatures (T=0.89, 0.87, 0.85, 0.82, 0.8). The 3D plot of the spinodals is also presented in the last panel. Closed to* $T_{\gamma}^{C_{PT}} = 0.9$ *the A-B-C spinodals are very similar and the maximum instability temperature is located close to the critical point of the pure* γ *solution for all mixtures.*

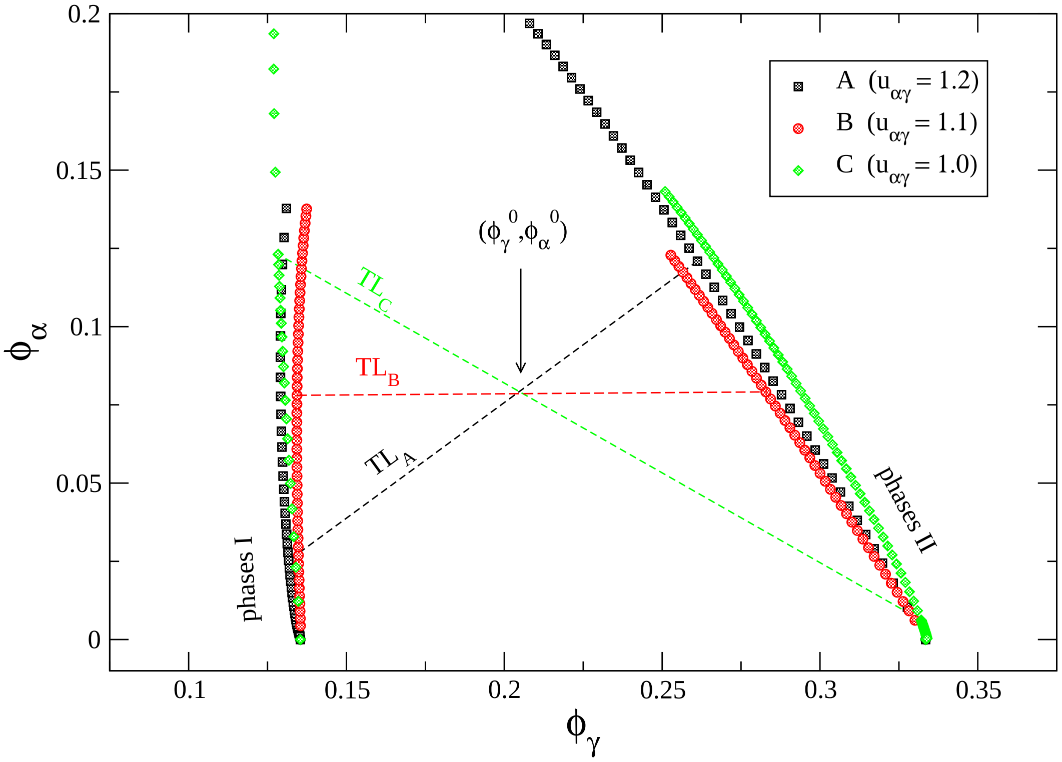

Figure 4.9: *Cut of the coexistence surface at* $T = 0.844$ *(slightly below* $T_\gamma^{C_{PT}} = 0.9$*) for mixtures A-B-C defined in Fig. 4.7. The tie lines (*TL_A*,*TL_B *and* TL_C*) obtained quenching the three mixtures from the same initial state* $(\phi_\gamma^0, \phi_\alpha^0)$ *are shown. For mixture A, high density mixed phases (phase II) coexist with low density mixed phases (phase I). For* $u_{\alpha\gamma} = 1.1$ *the tie lines are almost parallel to the* ϕ_γ *axis. By decreasing* $u_{\alpha\gamma}$ *slightly more (mixture C) tie lines with opposite tilts with respect to mixture A are found: almost pure and dense* γ *(II) coexist with mixed* α-γ *phases of lower density (I). While the phase separation process of the three mixtures is totally different, the cuts of the coexistence surface are almost indistinguishable.*

while the tie line of mixture B is almost parallel to the ϕ_γ axis. We discuss now in more details these tie lines and the underlying phase separation process that takes place in the different mixtures. To better visualize the composition of the different coexisting states, we also draw the snapshots corresponding to the different phases for each mixture.

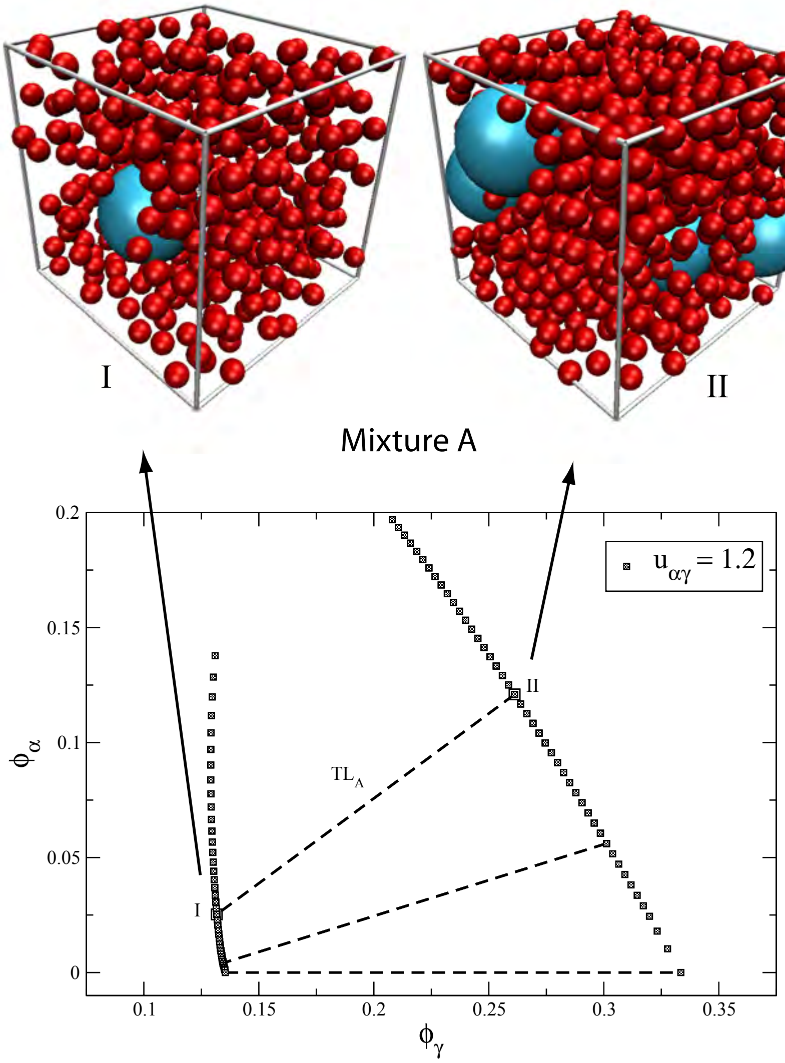

Figure 4.10: *Cut of the coexistence surface at* $T = 0.844$ *(slightly below* $T_\gamma^{C_{PT}} = 0.9$*) for mixture A defined in Fig. 4.7. High density mixed phases (phase II) coexist with low density mixed phases (phase I). The composition of phases I and II for tie line* TL_A *is represented in the snapshots. Both* α*s and* γ*s are present in the two phases.*

Mixture A ($u_{\alpha\gamma} = 1.2$)

The cut at $T = 0.844$ of mixture A binodal is presented in Fig. 4.10. As soon as ϕ_α^I raises, the packing fraction of the large α component in phase II (ϕ_α^{II}) increases strongly. Thus, dense mixed phases (of kind II) are in equilibrium with low density mixed phases (of kind I), as illustrated with the snapshots of phases I and II for tie line TL_A. In this case, both components are present in phases I and II, with the packing fraction of α crystallins larger in the high density phase than in phase I. The phase separation process involves mainly fluctuations in the total density ρ of the mixture, i.e in both ρ_α and ρ_γ. This corresponds to a condensation-like phase separation.

To complement the study of mixture A, other cuts of the binodal surface are also reproduced in Fig. 4.11. By extrapolation of the coexisting points, the location of the critical point for each temperature T is calculated (square on the figure). This forms a line of critical points which moves towards lower ϕ_γ and higher ϕ_α when lowering T. The tilt of the tie lines becomes also more pronounced (i.e. leading to a larger difference between the density of phases I and II) at lower temperature or, when increasing further $u_{\alpha\gamma}$. We found also that for larger $u_{\alpha\gamma}$, the line of critical points exhibit a maximum in temperature and the location of this maximum moves towards lower ϕ_γ and higher ϕ_α with increasing $u_{\alpha\gamma}$, in agreement with the calculation of the spinodal surface for strong $u_{\alpha\gamma}$ attractions, as presented in the previous section.

Mixture B ($u_{\alpha\gamma} = 1.1$)

Mixture B has a slightly lower attraction than case A but the small difference in $u_{\alpha\gamma}$ is sufficient to change completely the phase separation. Indeed, the important tilt of the tie lines found for mixture A totally disappears, as shown on Fig. 4.12: the packing fraction of αs in the high density and in the low density phase is almost the same ($\phi_\alpha^I \simeq \phi_\alpha^{II}$). This

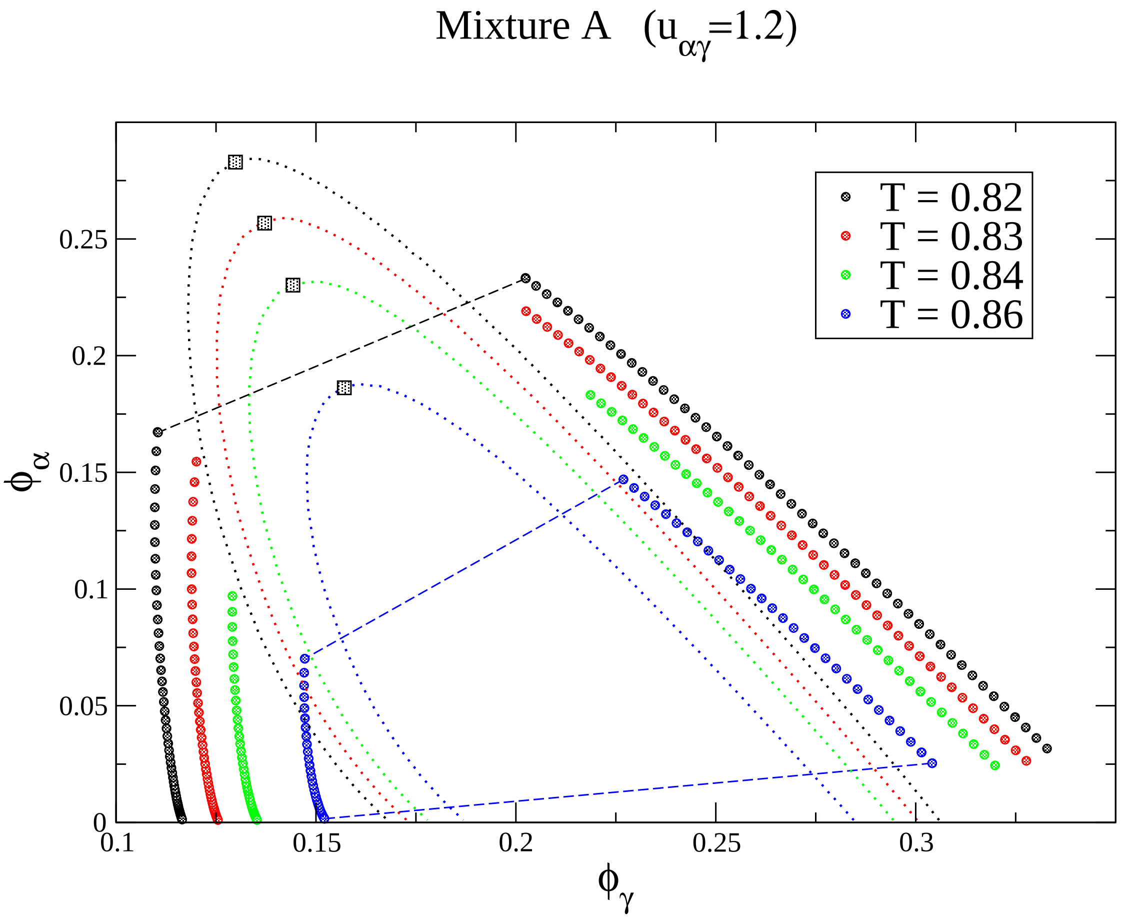

Figure 4.11: *The phase behaviour of mixture A defined in Fig. 4.7 is shown. The cuts of the coexistence surface have been performed at temperatures slightly below* $T_\gamma^{C_{PT}} = 0.9$*. The full circles represent the cuts of the binodal surface at* $T = 0.82, 0.83, 0.84, 0.86$*, and the corresponding cut of the spinodal are also drawn (small dots). Some tie lines (dashed lines) connecting coexisting states are shown. For each temperature cut, the critical point (square) is determined by extrapolation of the coexisting points and their intersection with the spinodal. This forms a line of critical points that moves towards higher* ϕ_α *and lower* ϕ_γ *when the temperature is reduced.*

means that the tie lines are almost parallel to the ϕ_γ axis. The snapshots corresponding to tie line TL_B are also depicted in Fig. 4.12. With respect to the composition of TL_A, the two coexisting phases of TL_B have almost the same ϕ_α, while ϕ_γ^{II} is slightly smaller than the corresponding ϕ_γ of the pure γ solution for the same temperature (T=0.844). This means that a condensation with an equal amount of αs crystallins in the high and in the low density phases takes place. Thinking in terms of a quench of the binary mixture from high temperature, the packing fraction of αs in the two low T phases is the same as the initial ϕ_α. Thus, for mixture B, the αs act almost as spectators of the phase separation of the γs and the transition is driven by fluctuations in the density of the γs only, as for the pure γ solution. The presence of the αs just lower ϕ_γ^{II}.

It is particularly instructive that the thermodynamically most stable binary mixture for our colloidal model of crystallin proteins (see cuts of the spinodal in Fig. 4.8) is the one whose phase separation process involves solely one of the components (the γ), while the mutual attraction is such that the second component (the α) do not influence at all the transition. Within our approach, the strength of the attraction between γs is fixed and the phase separation due to $u_{\gamma\gamma}$ will always take place. The presence of the second component can only raise the instability temperature. With a mutual attraction of $u_{\alpha\gamma} = 1.1$ the binary mixture can be stabilized up to the γ phase separation limit and mixture B is the most stable mixture that can be obtained, given the size ratio of the two components.

Mixture C ($u_{\alpha\gamma} = 1.0$)

Weaker attraction results in a clearly demixed situation as illustrated in Fig. 4.13 for tie line TL_C of mixture C: almost pure γ phases ($\phi_\alpha^{II} \simeq 0$) coexist with mixed phases that are very rich in αs. The difference in the composition of the two coexisting phases, with respect to the former mixtures, is clear on the snapshots that are also drawn on Fig. 4.13. The cut of the binodal surface is here at a temperature just below $T_\gamma^{C_{PT}}$. This demixing situation is even more pronounced if the mixture is quenched to lower temperature, or for mixtures with smaller $u_{\alpha\gamma}$.

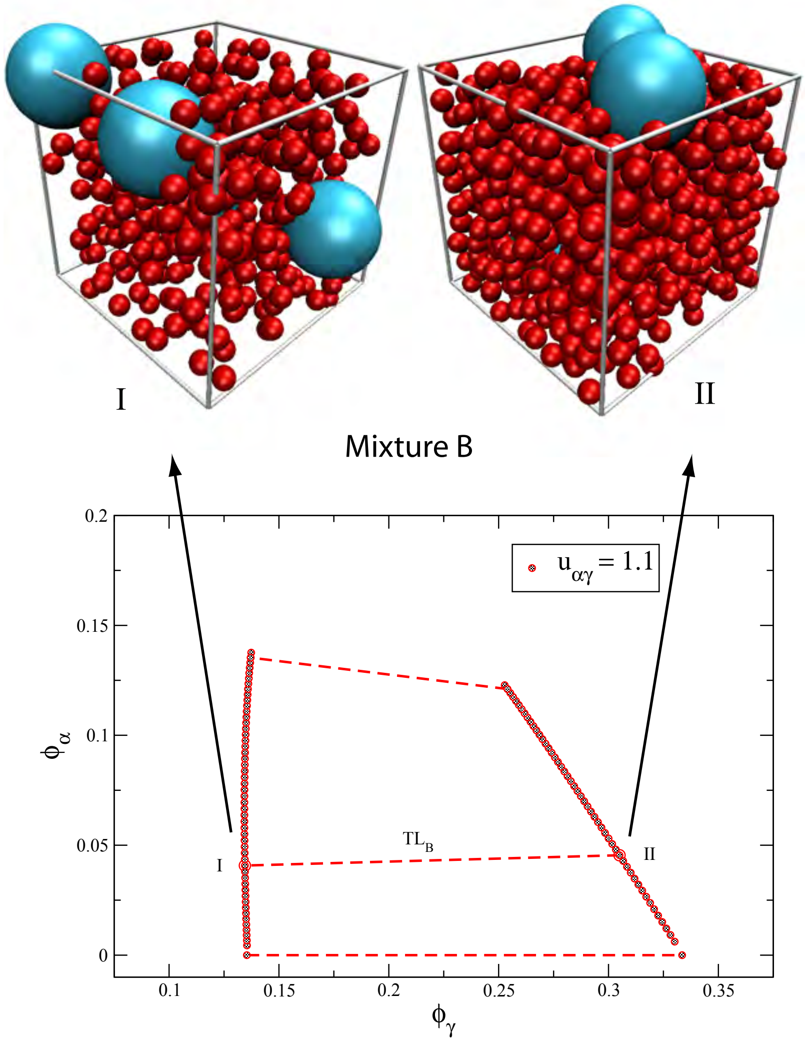

Figure 4.12: *Cut of the coexistence surface at* $T = 0.844$ *(slightly below* $T_\gamma^{C_{PT}} = 0.9$*) for mixture B defined in Fig. 4.7. The tie lines are almost parallel to the* ϕ_γ *axis. The snapshots representing the two coexisting phases of* TL_B *are drawn. Both components are present in the two phases and* $\phi_\alpha^I \simeq \phi_\alpha^{II}$*. Fluctuations in* ρ_γ *only are responsible for the phase transition.*

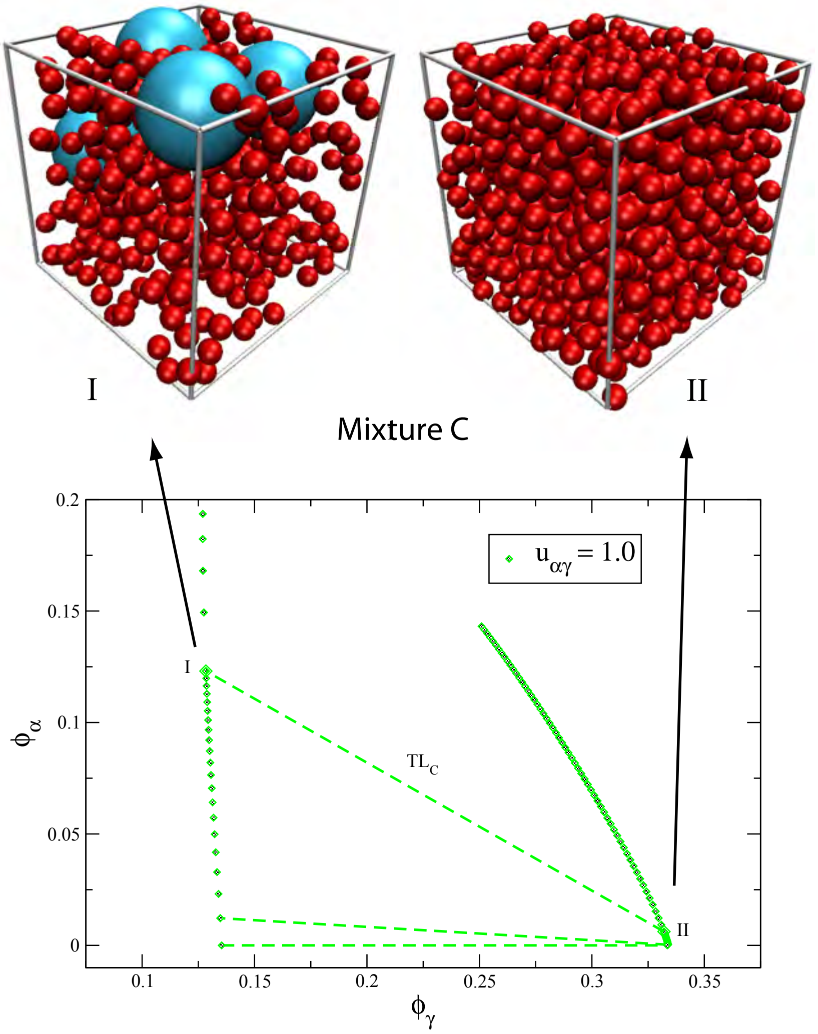

Figure 4.13: *Cut of the coexistence surface at* $T = 0.844$ *(slightly below* $T_\gamma^{CPT} = 0.9$*) for mixture C defined in Fig. 4.7. Tie lines with opposite tilts with respect to mixture A are found: almost pure and dense* γ *(type II) coexist with mixed* α-γ *phases of lower density (type I). The snapshots representing the two coexisting phases of* TL_C *are drawn.*

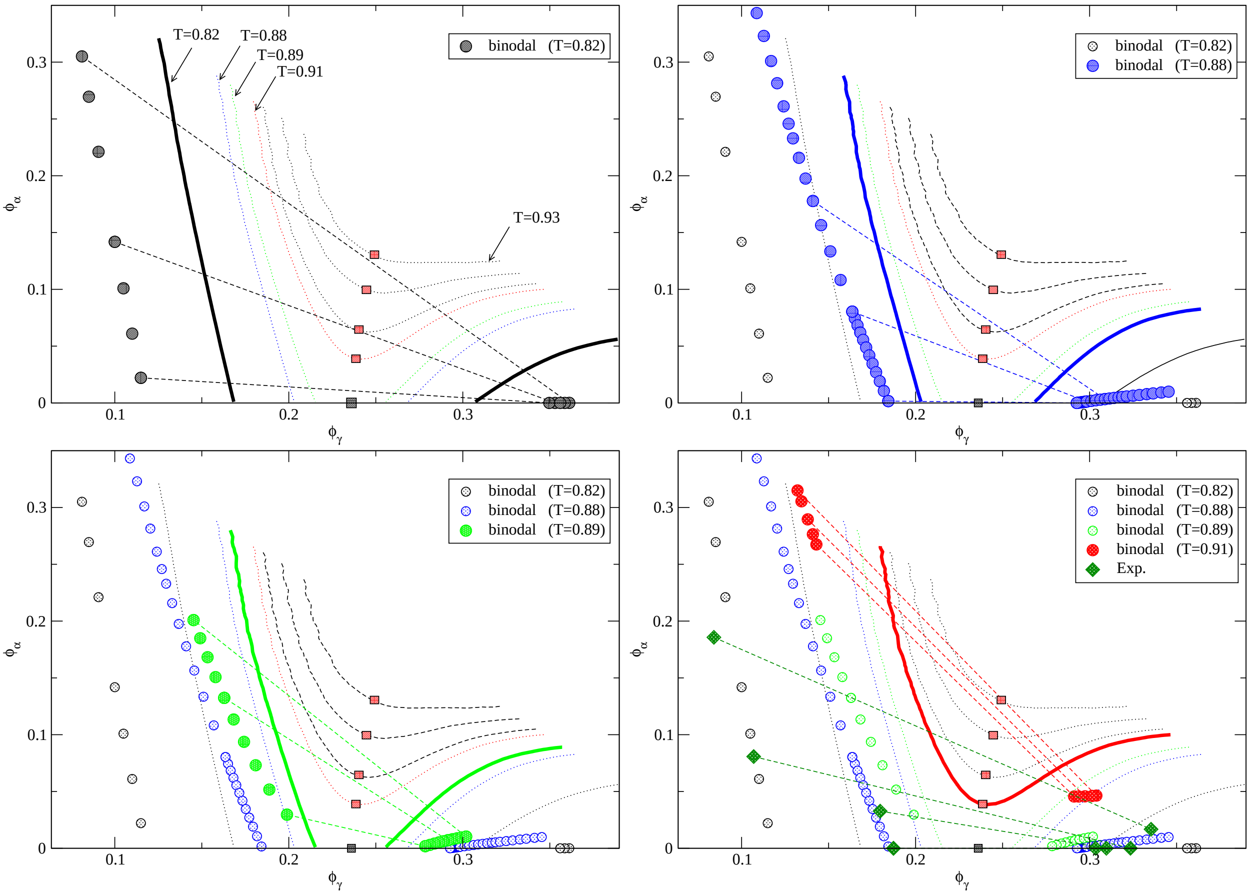

Figure 4.14: *Cuts of the coexistence surface of mixture D at temperatures T=0.82, 0.88, 0.89 and 0.91 are presented (circles) with the corresponding spinodal (full and dotted lines) and some of the tie lines (dashed lines). The spinodals for higher T (up to T=0.93) are also shown (dashed lines). The experimental tie lines pairs (full diamonds and dashed lines) were taken from [Thurston, 2006]. Estimations of the critical points (squares) are shown as well. The critical points are shifting towards higher ϕ_α and ϕ_γ with increasing temperature.*

Mixture D ($u_{\alpha\gamma} = 0.85$)

The value of $u_{\alpha\gamma}$ we derived by comparison of the MD simulations with the SANS was at the lower boundary of the stable region and, thus, the natural α-γ crystallin mixture which is by definition stable has an instability boundary that is located on average at higher temperatures with respect to the A, B and C mixtures. This is also in agreement with the cloud point determination which shows an important rise of the instability temperature when moving in the phase diagram towards high packing fractions of both α and γs [Thurston, 2006]. Thus, to make a step further towards the natural α-γ crystallin binodal, the coexistence surface of a fourth mixture with weaker $u_{\alpha\gamma}$ attraction (mixture D with $u_{\alpha\gamma} = 0.85$ defined in Fig. 4.7) was also determined. Mixture D falls indeed in the stable region, as the previous one, but its spinodal rises to higher temperatures when entering the phase diagram away from the pure γ solution and the mixture separates at temperatures above $T_{\gamma}^{C_{PT}} = 0.9$ as well. Cuts of the binodal surface at temperatures below and above $T_{\gamma}^{C_{PT}}$ are presented in Fig. 4.14 with some tie lines and the corresponding spinodals. The experimental tie lines taken from [Thurston, 2006] are also drawn in the last panel.

For temperatures below $T_{\gamma}^{C_{PT}}$ (see $T = 0.82$ in the first and $T = 0.88$ in the second panel) the propensity to demix is strong: the shape of the binodal is also different with respect to mixture C since phase II expands towards higher ϕ_{γ}^{II} and ϕ_{α}^{II} is about 0. At higher temperature, ϕ_{α}^{II} is slightly bigger, but the tie lines remain highly tilted. We note that, in the limit of no attraction between unlike proteins, coexistence of almost pure phases ($\phi_{\alpha}^{II} \simeq 0$ and $\phi_{\gamma}^{I} =\simeq 0$) is also obtained for temperatures above $T_{\gamma}^{C_{PT}}$ (consistent with the spinodal for $u_{\alpha} = 0$ presented in Fig. 4.1). For mixture D, the calculation of coexisting points above $T_{\gamma}^{C_{PT}}$ in the close vicinity of the line of critical points was not possible, but from the few points calculated and the shape of the spinodal, we found that the line of critical points expands from the critical point of the γ solution to higher ϕ_{γ} and T, as shown by the squares on Fig. 4.14.

The study of the symmetric and asymmetric mixtures in Chapter 3 gave us some interesting clues to understand the demixing situation that we observed for $u_{\alpha\gamma} < 1.1$: since the interaction between unlike particles is weaker than that between γs (even zero in the hard sphere limit), the internal energy will tend to promote demixing between the two species. The gain in internal energy is expected to overcome easily the loss in entropy implied by the demixing, especially at high density. Thus, quenching the mixture at a given ϕ_α will result in a strong (respectively weak) demixing at high (respectively low) ϕ_γ. The demixed situation that we hypothesized looking at the snapshot of the MD simulations for weak attraction (upper right panel of 2.12) is thus confirmed.

Moreover, according to the same intuitive arguments we just mentioned, demixing is clearly enhanced by the large size asymmetry between the two crystallins and, for a given (weak) attraction, the instability boundary will be located at higher temperature when the size asymmetry increases. Thus, the sensitivity of the thermodynamic stability of $\alpha\gamma$ binary mixture to their mutual attraction is also a consequence of their important size asymmetry and we expect binary mixtures of γ and β crystallins, that might be studied in the future, to be less sensitive to their mutual interaction since $d_\gamma < d_\beta < d_\alpha$. However, the size asymmetry contributes to the demixing situation for reasons that are more *energetic* than *entropic*: depletion induced interaction between the α might be present in the binary mixture of crystallins (or when the system is simulated) and, thus, might contribute to the demixing, but it is primarily the difference between $u_{\alpha\gamma}$ and $u_{\gamma\gamma}$ that is responsible for the demixing. This appears already in our investigation of the symmetric and asymmetric binary mixtures in Chapter 3. And indeed, by changing the size of the αs, keeping $u_{\alpha\gamma} = 0$, we found spinodals consistent with a very strong demixing even for $d_\alpha = d_\gamma$.

The determination of the tie lines from perturbation theory gave interesting insights when combined with the experimental tie-lines of mixture of α-γ crystallins. The α-γ mixture phase separation was found to involve substantial segregation by protein type [Thurston, 2006] as shown by the important tilt of the tie lines on Fig. 4.14. The same behaviour is obtained within perturbation theory when lowering $u_{\alpha\gamma}$ slightly below 1.1 (the value of the attraction for which the binary mixture is the most stable). From a thermodynamic point of view, a little increase in the attraction between the two crystallins would stabilize even more the mixtures against demixing. This means that the natural α-γ attraction is located at the boundary of the stable region and the unstable region towards demixing. Even if the phase diagram of the natural α-γ crystallin mixture is dominated by demixing (as we found from the comparison of the experimental and the PT tie lines), the weak $u_{\alpha\gamma}$ attraction is strong enough to keep the instability boundary to low temperatures. Thus, the stability picture obtained from MD simulations and summarized in Fig. 2.6 is now formally derived from the coexistence behaviour on the whole parameter space.

A decrease in the binding affinity of γs and αs with ageing is the scenario that involves the smallest energy change in the attraction between the crystallins and could produce sufficient inhomogeneities to lead to the opacification of the lens. Moreover, there are considerable evidences that the condensed phase present in some forms of cataract is enriched in γ-crystallins [Lerman et al., 1966; Siezen et al., 1985]. This has been the motivation for many studies of the phase separation of γ crystallin solution and has led the conclusion that γ-crystallins and the possible phase separation of γs play an essential role in the formation of many forms of cataract. Within our perturbative approach, we show that the occurrence of an almost pure gamma dense phase might result from demixing in a binary α-γ mixture when $u_{\alpha\gamma}$ is only slightly weakened. In light of our PT calculations and recent experiments on the binding affinity between α and γ crystallins [Takemoto and Ponce, 2006], we believe that a decrease of the α-γ attraction with ageing is very likely the most probable scenario.

4.4 Conclusions

This chapter was dedicated to the calculation of the stability boundary of the binary mixture in the full parameter space via a thermodynamic perturbation theory approach. Perturbation theory turns out to be well-suited to study the instability of asymmetric binary square well mixtures. All the critical behaviour expected from the SANS experiments was correctly predicted, at least qualitatively. We also obtained quantitative agreement with the results of the MD simulations for the determination of the strength of the mutual attraction. This theoretical approach allowed us to confirm the validity of the model we built for the mixture of crystallin proteins from a totally different route. The calculation of the spinodal surface in the full parameter space gave also a better insight into the different mechanisms responsible for the instability in the binary mixture.

The study of the instability boundaries of our colloidal model for crystallin mixtures recognizes two new molecular mechanisms by which altered eye lens crystallin protein interactions can potentially lead to cataract disease. First, concentrated mixtures of α and γ crystallin become unstable with respect to protein composition-type phase separation if the α-γ attraction is too weak. On the other hand, when the α-γ attraction is strong, the α-γ mixtures become unstable with respect to protein concentration-type phase separation. The determination of the binodal surfaces and the tie lines shows that, among these two scenarios, a destabilization of the α-γ mixture due to a decrease in the $u_{\alpha\gamma}$ attraction involves the smaller energy change. Moreover the composition of the coexisting phases are extremely sensitive to $u_{\alpha\gamma}$. In combination with recent work [Thurston, 2006], the present study further underlines the role of size disparity between α and γ-crystallins.

It is very important to recognize that each of these crystallin instability mechanisms can potentially contribute to cataract at temperatures well above those at which thermodynamic instability occurs. Indeed, it has been shown that near the phase separation of

γ crystallins alone [Schurtenberger et al., 1989, 1993; Fine et al., 1996; Thurston, 2006], critical density fluctuations will dramatically increase light scattering at temperatures well above phase separation, still in the single-phase region of the phase diagram. Moreover, the very reason for enhanced light scattering, namely the enhancement of spontaneous local concentration fluctuations, can also accelerate nucleation and growth of protein aggregates [ten Wolde and Frenkel, 1997]. It is clearly important to identify specific molecular factors that mediate both the strength of γ-α attraction and the size disparity between these proteins, and to identify the effects of shape and orientation-dependent interactions, not considered here, on γ-α mixture instability.

This work has explored only one out of the three principal binary crystallin mixtures. Each of them can serve as a base study for the more realistic case of γ, α and β crystallin mixtures. For this reason it represents a step to understand the specific relation between lens proteins interactions and eye lens transparency.

CHAPTER 5

Conclusions

In the present work we have developed a colloidal model for α and γ crystallins which are two among the three existing families of eye lens proteins. The properties of their mixtures were understood combining numerical simulations and experimental neutron scattering data. A weak short range attraction between the two crystallins was essential to maintain the stability of the mixture and reproduce the experimental behaviour of α-γ crystallin solutions. Indeed, slightly too strong or slightly too weak attraction resulted in a spectacular enhancement of the forward scattering intensity and, thus, would lead to the opacification of the protein solution.

We then used thermodynamic perturbation theory to study the phase behaviour of binary mixtures of simple interacting particles made of a hard core plus an attractive potential. We showed that such theory reproduces all the known phase diagram topologies of the symmetric binary mixtures and constitutes a real improvement with respect to standard

mean field approaches. Moreover, we could extend this theory to mixtures where the two components differ in size.
Finally, the instability boundaries and the coexistence surfaces of the binary α-γ mixture were determined as a function of $u_{\alpha\gamma}$ within perturbation theory and we were able to relate the high forward scattering obtained in the simulations to the location of the spinodal surface. The phase diagram of asymmetric α-γ mixtures is extremely sensitive to the $u_{\alpha\gamma}$ attraction: the mixture becoming unstable with respect to protein composition-type phase separation, for too weak α-γ attraction, or to protein concentration-type phase separation for too strong α-γ attraction. The two scenarios lead to coexisting phases of totally different composition.

From a general point of view, we have demonstrated how a colloidal approach and the application of concepts from soft matter physics to complex protein mixtures provide new insights into the stability of eye lens protein mixtures. The numerical and theoretical methods we developed could be applied in the future to other mixtures of crystallins proteins using new scattering data or cloud points measurements as inputs. Moreover, the determination of crystallin mixture phase diagrams could also help design more targeted experimental protocols and, thus, reduce significantly the needed amount of protein and the beam time for the scattering experiments.

The present findings lay also the groundwork for studying the corresponding proteins of the human lens. Until now, experiments have been only performed on calf lens proteins. However, the extreme sensitivity of the phase boundaries to apparently minor molecular changes indicates clearly that, in order to understand the basis of cataract disease in man, it is crucial to shortly investigate solutions of specific human proteins as well.

From a theoretical point of view, the determination of the coexisting phase compositions provided by perturbation theory is certainly highly useful when coupled with cloud points measurements. However, the implementation of more advanced liquid state theories, like for instance HRT, to investigate the phase behaviour of the different mixtures of crystallins proteins could push the comparison to a more quantitative level in the future.

In order to account for complex phenomena like protein aggregation or protein phase separation which involve a large number of components, it is essential to devise effective interaction potentials, as we did in this study by deriving an isotropic attraction between the proteins. However, it is well known that the crystallins and proteins in general have strong spatial variations of the interactions on their surface and that isotropic models are not always capable to address correctly phenomena like protein aggregation or self-assembly. At the same time, an appealing confluence of the chaperone and the phase transition approaches to opacification is suggested by the presence of hydrophobic spots on α-crystallins which enable them to bind to other proteins. The elaboration of such *aeolotopic* models of interaction would permit the simultaneous investigation of the physical factors that influence both the chaperone effect and phase separation.

Appendix A

Resolution Function

In order to account for the experimental smearing, we derived a general resolution function resulting from the combined effect of wavelength spread (w), finite collimation (c) and detector resolution (d). The resolution function $R(\mathbf{q}, \langle\mathbf{q}\rangle)$ describes the distribution of the radiation with scattering vector $\mathbf{q}$ contributing to the scattering for the setting $\langle\mathbf{q}\rangle$. The measured intensity at $\langle\mathbf{q}\rangle$ is then proportional to:

$$I(\langle\mathbf{q}\rangle) \quad = \quad \int R(\mathbf{q}, \langle\mathbf{q}\rangle)\frac{\mathbf{d}\sigma(\mathbf{q})}{\mathbf{d\Omega}}\mathbf{dq} \tag{5.1}$$

where $d\sigma(\mathbf{q})/\mathbf{d\Omega}$ is the scattering cross section. We followed the method proposed by Pedersen et al. [Pedersen et al., 1990] in which the different contributions to the resolution function are all approximated by Gaussian functions and are derived separately for each contribution, assuming the other ones to be negligible.

$$R(q, \langle\mathbf{q}\rangle) \quad = \quad \frac{1}{\sqrt{(2\pi\sigma^2)}}e^{-\frac{(q-\langle q\rangle)^2}{2\sigma^2}} \tag{5.2}$$

The Gaussian functions are determined by calculating the width σ of the distribution and are defined to have the same full width at half maximum ($FWHM$) value as the distribution they approximate. In the following, $\Delta\lambda$ will denote the $FWHM$ of the wavelength distribution and Δ the $FWHM$ of the distribution of $(s - \langle s\rangle)$, where $\langle s\rangle$ is the distance from the beam centre at the detector to the point on the detector with scattering angle $\langle 2\theta\rangle$. The combined resolution function due to all three contributions is then calculated assuming them to be independent and can be approximated by a Gaussian with a width σ given by $\sigma^2 = \sigma_c^2 + \sigma_d^2 + \sigma_w^2$ where

$$\begin{aligned}\sigma_c &= \langle k\rangle \cos\langle\theta\rangle \frac{\Delta\beta_1}{2(2\ln(2))^2} &(5.3)\\ \sigma_d &= \langle k\rangle \cos\langle\theta\rangle \cos^2\langle 2\theta\rangle \frac{\Delta}{2l(2\ln(2))^2} &(5.4)\\ \sigma_w &= q_0 \frac{\Delta\lambda}{\langle\lambda\rangle} \frac{1}{2(2\ln(2))^{\frac{1}{2}}} &(5.5)\end{aligned}$$

and $\theta = \arcsin(\lambda q/2\pi)$, with wavelength λ for q-vector q, with r_1 being the radius of the source aperture, r_2 the radius of the sample aperture, L the source-sample distance, l the detector-sample distance, and defining $a_1 = r_1(L + l/\cos^2(2\theta))^{-1}$, $a_2 = r_2\cos^2(2\theta)$ where:

$$\begin{aligned}\Delta\beta_1 &= 2\frac{r_1}{L} - \frac{1}{2}\frac{r_2^2}{r_1}\frac{\cos^2\langle 2\theta\rangle}{l^2 L}(L + \frac{l}{\cos\langle 2\theta\rangle})^2 & a_1 > a_2\\ \Delta\beta_1 &= 2r_2(\frac{1}{L} + \frac{\cos^2\langle 2\theta\rangle}{l})\\ &\quad -\frac{1}{2}\frac{r_1^2}{r_2}\frac{l}{L}\frac{1}{\cos^2\langle 2\theta\rangle(L + \frac{l}{\cos^2\langle 2\theta\rangle})} & a_1 < a_2\end{aligned} \qquad (5.6)$$

When the scattering pattern is circularly symmetric, the two dimensional integration involved in the convolution of the cross section and the resolution function can be replaced by a one dimensional integration:

$$I(\langle q\rangle) \quad = \quad \int_0^\infty R_{av}(q,\langle q\rangle)\frac{d\sigma(q)}{d\Omega}dq \tag{5.7}$$

with the averaged resolution function $R_{av}(q,\langle q\rangle)$:

$$\begin{aligned} R_{av}(q,\langle q\rangle) &= \int_{-\pi}^{\pi} R(q,\langle q\rangle)qd\phi \\ &= \frac{q}{\sigma^2}e^{-\frac{(q^2-\langle q\rangle^2)}{2\sigma^2}}I_0(q\langle q\rangle\sigma^{-2}) \end{aligned} \tag{5.8}$$

in which I_o is the modified Bessel function of first kind and zeroth order and $\sigma = \sqrt{\sigma_c^2+\sigma_d^2+\sigma_w^2}$.

Appendix B

Partial radial distribution function of hard spheres

Perturbation theory relies on an accurate description of the reference system, for which we have chosen a binary mixture of hard sphere particles. In particular, the partial radial distribution functions g_{ij}^0 that appears in the expression for the Helmholtz free energy must be evaluated. We compute the $g_{ij}^0(r)$ solving the Ornstein-Zernike integral equations with the Percus-Yevick (PY) closure using the partial direct correlation functions $c_{ij}(r)$ of the binary mixture obtained by Lebowitz within the Percus-Yevick (PY) approximation [Lebowitz, 1964]. In order to correct the shortcomings of the PY hard sphere distribution functions (the values at contact $g_{ij}^0(d_{ij})$ and the slopes $g_{ij}^0{}'(d_{ij})$ are both too small in magnitude) we used the Grundke-Henderson procedure, a generalization to mixtures of the Verlet-Weis modifications [Verlet and Weis, 1972; Henderson and Grundke, 1975]. We will present now the details of the calculation of the $g_{ij}^0(r)$s.

Ornstein-Zernike equations with Percus-Yevick closure for binary hard sphere mixtures

The OZ equation is an integral equation that was first introduced by L.S. Ornstein and F. Zernike in their investigation of the density fluctuations near the critical point. It relates the total correlation function $h(\mathbf{r}) = g(\mathbf{r}) - 1$ to the direct correlation function $c(\mathbf{r})$ [Hansen and McDonald, 1986]. For a one component system, homogeneous and isotropic, the OZ relation can be written as:

$$h(\mathbf{r}) = c(\mathbf{r}) + \rho \int c(\mid \mathbf{r} - \mathbf{r}' \mid)\, h(\mathbf{r}')\, d\mathbf{r}' \tag{5.9}$$

This expression, which can be solved recursively, describes the fact that the total spatial correlation is due in part to the direct correlation, but also to the indirect correlation propagated via increasingly large number of intermediate positions. From the analysis of graphical expansions [Hansen and McDonald, 1986] it is very likely that the range of $c(\mathbf{r})$ is comparable with the range of the pair potential $v(\mathbf{r})$ while, because of the effects of the indirect correlation, $h(\mathbf{r})$ can be much longer ranged, especially in the vicinity of a critical point.

The Fourier transform of the OZ equation yields:

$$h(\mathbf{k}) \quad = \quad c(\mathbf{k}) + \rho h(\mathbf{k})\, c(\mathbf{k}) \tag{5.10}$$

which gives an algebraic relation between $h(\mathbf{k})$ and $c(\mathbf{k})$:

$$h(\mathbf{k}) \quad = \quad \frac{c(\mathbf{k})}{1 - \rho c(\mathbf{k})} \tag{5.11}$$

For homogeneous and isotropic multicomponent systems, the Fourier transform of the OZ relations become:

$$h_{\alpha\beta}(\mathbf{k}) = c_{\alpha\beta}(\mathbf{k}) + \sum_{\gamma} \rho_\gamma c_{\alpha\gamma}(\mathbf{k})\, h_{\beta\gamma}(\mathbf{k}) \tag{5.12}$$

For a binary mixture of species 1 and 2, the following system must be solved:

$$\begin{aligned} h_{11}(\mathbf{k}) &= c_{11}(\mathbf{k}) + \rho_1 c_{11}(\mathbf{k})\, h_{11}(\mathbf{k}) + \rho_2 c_{12}(\mathbf{k})\, h_{21}(\mathbf{k}) \\ h_{22}(\mathbf{k}) &= c_{22}(\mathbf{k}) + \rho_1 c_{21}(\mathbf{k})\, h_{12}(\mathbf{k}) + \rho_2 c_{22}(\mathbf{k})\, h_{22}(\mathbf{k}) \\ h_{12}(\mathbf{k}) &= c_{12}(\mathbf{k}) + \rho_1 c_{11}(\mathbf{k})\, h_{12}(\mathbf{k}) + \rho_2 c_{12}(\mathbf{k})\, h_{22}(\mathbf{k}) \end{aligned} \tag{5.13}$$

with $c_{\alpha,\gamma}(\mathbf{k}) = c_{\gamma,\alpha}(\mathbf{k})$ and $h_{\alpha,\gamma}(\mathbf{k}) = h_{\gamma,\alpha}(\mathbf{k})$. In order to solve this set of linear equations we define

$$\begin{aligned} R_1(\mathbf{k}) &= \rho_1 c_{11}(\mathbf{k}) - 1 \\ R_2(\mathbf{k}) &= \rho_2 c_{12}(\mathbf{k}) \\ R_3(\mathbf{k}) &= \rho_1 c_{12}(\mathbf{k}) \\ R_4(\mathbf{k}) &= \rho_2 c_{22}(\mathbf{k}) - 1 \end{aligned} \tag{5.14}$$

and

$$\begin{aligned} S_1(\mathbf{k}) &= -c_{12}(\mathbf{k}) + \frac{R_1(\mathbf{k})}{R_3(\mathbf{k})} c_{22}(\mathbf{k}) \qquad (5.15) \\ S_2(\mathbf{k}) &= -c_{22}(\mathbf{k}) - \frac{R_3(\mathbf{k})\, R_4(\mathbf{k})}{R_2(\mathbf{k})\, R_3(\mathbf{k}) - R_1(\mathbf{k})\, R_4(\mathbf{k})}\, S_1(\mathbf{k}) \end{aligned}$$

The solution of OZ equations can be cast:

$$\begin{aligned} h_{11}(\mathbf{k}) &= \frac{1}{R_1(\mathbf{k})} [-c_{11}(\mathbf{k}) - \frac{R_2(\mathbf{k})}{R_3(\mathbf{k})} S_2(\mathbf{k})] \\ h_{12}(\mathbf{k}) &= \frac{1}{R_3(\mathbf{k})}\, S_2(\mathbf{k}) \\ h_{11}(\mathbf{k}) &= \frac{R_3(\mathbf{k})}{R_2(\mathbf{k}) - R_1(\mathbf{k})\, R_4(\mathbf{k})}\, S_1(\mathbf{k}) \end{aligned} \tag{5.16}$$

In order to calculate $h_{ij}(k)$, the partial direct correlation functions $c_{ij}(k)$ must be determined. The $c_{ij}(r)$ of binary hard sphere mixtures have been obtained analytically by Lebowitz within the PY approximation (relations 37 to 40 in [Lebowitz, 1964]) . Starting from these expressions of $c_{ij}(r)$, we calculated their Fourier Transform (FT) $c_{ij}(k)$), which are still analytical, and then solved the previous relations.

The last step for determining the radial distribution function of binary hard sphere mixtures involves the calculation of the inverse FT of the $h_{ij}(k)$. However, within the PY approximation, the $h_{ij}(r)$ show discontinuities for $r = d_{ij}$, and trying to compute the inverse FT numerically gives rise to large oscillations (*Gibbs oscillations*) at the contact value.

To overcome this defect, let's write $h_{ij}(r)$ as:

$$\begin{aligned} h_{ij}(r) &= h_{ij}(r) + \Delta_{ij}\,\Theta(R_{ij} - r) - \Delta_{ij}\,\Theta(R_{ij} - r) \\ &= h^*_{ij}(r) - \Delta_{ij}\,\Theta(R_{ij} - r) \end{aligned} \tag{5.17}$$

where $\Delta_{ij} = g_{ij}(d^+_{ij})$ (the contact value of the RDF) and Θ is the Heaviside step function. The FT of h_{ij} can be determined from the FT of $\Theta(R_{ij} - r)$:

$$h_{ij}(q) = h^*_{ij}(q) + \Delta_{ij}\,\widehat{\theta}(k) \tag{5.18}$$

with

$$\begin{aligned} \widehat{\theta}(k) &= FT\{\theta(R_{ij} - r)\} \\ &= \frac{4\pi}{k}\int_0^\infty sin(kr)\Theta(R_{ij} - r)dr \\ &= \frac{4\pi}{k^3}[\sin(R_{ij}k) - R_{ij}k\cos(R_{ij}k)] \end{aligned} \tag{5.19}$$

and the IFT of $h^*_{ij}(q)$, which now shows no discontinuity, can be computed. From $h^*_{ij}(r)$ we recover $g_{ij}(r) = h_{ij}(r) + 1$.

Grundke-Hendersen correction

The OZ relations were solved using the PY closure for binary hard sphere mixtures. However, PY hard sphere distribution functions have two major shortcomings with respect to the values at contact $g_{ij}(d_{ij})$ and the slopes $g'_{ij}(d_{ij})$, both of which are too small. Verlet and Weis gave a procedure to approximately overcome these defects in the pure fluid case, and Grundke and Hendersen generalized this procedure for mixtures [Verlet and Weis, 1972; Grundke and Henderson, 1972].

$$
\begin{aligned}
g_{ij}(\frac{r}{d_{ij}}, \eta) &= g^{PY}_{ij}(\frac{r}{d'_{ij}}) + \Delta g_{ij}(r) \\
\Delta g_{ij}(r) &= \frac{A_{ij}}{r} \exp(-b_{ij}(r - d_{ij})) \times \\
&\quad \cos(b_{ij}(r - d_{ij}))
\end{aligned}
\tag{5.20}
$$

with the packing fraction η and

$$
d'_{ij} = d_{ij}(1 + \frac{\eta}{16})^3 \tag{5.21}
$$

The slight change in sphere diameter in the argument of $g^{PY}(r)$ produces a small correction in the phase of the oscillations of the distribution function. The purpose of the A_{ij} coefficients is to raise the value of $g(r)$ at contact. Since Δg_{ij} must oscillate and the PY solution gives a good approximation for the radial distribution function at large r, a trigonometric factor which is damped by $\frac{1}{r} exp(b_{ij}(d_{ij} - r))$ is included.

According to the $MCSL$ equation of state the pressure is given by a linear combination of the pressure obtained from the PY integral equation for the RDF following the compressibility and the virial routes: $p^{MCSL} = \frac{1}{3}p_p^{PY} + \frac{2}{3}p_c^{PY}$. The PY radial distribution function at contact will give, by definition, the p_p^{PY} when used in the pressure equation. Moreover, the Scaled Particle Theory (SPT) for mixtures also reproduces p_p^{PY} via the pressure equation. The contact value of the radial distribution function can then be written as:

$$g_{ij}(d_{ij}) \;=\; \frac{1}{3}g_{ij}^{PY}(d_{ij}) + \frac{2}{3}g_{ij}^{SPT}(d_{ij})$$

This postulate determined the A_{ij} coefficients and forced the distribution functions to give p^{MCSL} when used in the pressure equation:

$$A_{ij} \;=\; [\frac{1}{3}g_{ij}^{PY}(1,\eta) + \frac{2}{3}g_{ij}^{SPT}(1,\eta) - g_{ij}^{PY}(\frac{d_{ij}}{d'_{ij}},\eta)]d_{ij}$$

The pressure consistency can also be generalized to provide the b_{ij}s [Grundke and Henderson, 1972]. Lee and Levesque gave the following approximation [Lee and Levesque, 1973], which avoids the numerically involved computation of $\frac{\partial \mu_j}{\partial \rho_i}$ from the compressibility equation:

$$b_{ij} \;\approx\; 24\frac{A_{ij}}{\eta' g_{ij}^{PY}(1,\eta')d_{ij}^2}$$

List of Figures

2.1 Small-angle neutron scattering intensity $I(q)$ vs. wavevector magnitude q for high concentration bovine γB and α crystallin mixtures, showing evolution from pure γB to α. Mixing ratios C_α of a 230 mg/ml α-crystallin ($C_\alpha = 1$) and a 260 mg/ml γ-crystallin stock solution are shown as follows: pure α-crystallin, i.e. $C_\alpha = 1$ (dots), $C_\alpha = 0.5$ (squares), $C_\alpha = 0.25$ (diamonds), $C_\alpha = 0.125$ (triangles) and pure γ-crystallins, i.e. $C_\alpha = 0$ (crosses). 15

2.2 Concentration-normalized scattered intensities of diluted α-crystallin (squares) and γ-crystallin (plus) solutions (4 mg/ml and 8 mg/ml) that were used as the experimental form factors. Also shown are the IFT fits (solid lines). . 20

2.3 Neutron scattering intensities for the concentrated, pure α crystallin solution in the present buffer are well-modeled with use of a hard-sphere potential in molecular dynamics simulations. SANS intensities (dots) and MD results (line) for hard-spheres at packing fraction $\phi_\alpha = 0.39$ are shown. The location of the peak $q^* \sim 2\pi/d_\alpha = 0.385\, nm^{-1}$ is also drawn. 23

2.4 Neutron scattering intensities for the concentrated, pure γ crystallin solutions in the present buffer can be approximated, for wave-vector magnitudes below 1 nm^{-1}, with use of a spherical square-well potential in molecular dynamics simulations. SANS measurements (dots) and results from molecular-dynamics simulations (line) for square-well particles ($\lambda_\gamma = 0.25 d_\gamma$, $u_{\gamma\gamma} = 1$, $\overline{T} = 0.7875$) at packing fraction $\phi_\gamma = 0.18$ are shown. 25

2.5 Attraction between α and γ crystallins is essential for modeling neutron scattering intensities of their high concentration mixtures [Stradner et al., 2007]. SANS intensities for the $C_\alpha = 0.5$ mixture: (dots) and results from molecular-dynamics simulations at $\overline{T} = 0.7875$ are shown for three different values of the interspecies interaction ($u_{\alpha\gamma} = 0$, $u_{\alpha\gamma} = 0.55$ $u_{\alpha\gamma} = 2$ denoted by the dashed, the full and the dotted line respectively). 27

2.6 A narrow range of the attraction strength between α and γ crystallins is compatible with avoiding high concentration phase separation instability. Dots show calculated neutron scattering intensities for $q^* = 0.0467\, nm^{-1}$, from analysis of molecular dynamics simulations, versus the α-γ attraction square well depth $u_{\alpha\gamma}$ for the $C_\alpha = 0.5$ mixture (see text). The attraction range in which the mixture remains stable against phase separation and can be equilibrated is also drawn. The dark point indicates the value of $u_{\alpha\gamma}$ we used to model the α-γ mixture and the dashed line represents the experimental $I(q^*)$ 29

2.7 The neutron scattering intensities for the $C_\alpha = 0.25$ (top) and $C_\alpha = 0.125$ (bottom) mixtures are compatible with the α-γ square-well depth determined by comparison of MD simulations with the $C_\alpha = 0.5$ SANS measurements. SANS measurements are represented by dots and results from molecular-dynamics simulations by full lines. The parameters of the simulated model are presented in Tables 2.1 and 2.2 30

2.8 Predicted partial structure factors obtained from the MD simulations of the various C_α mixtures. (upper left panel) $S_{\alpha\alpha}$; (upper right panel) $S_{\gamma\gamma}$; (lower panel) $S_{\alpha\gamma}$ 35

2.9 Partial radial distribution functions $g_{\alpha\alpha}(r)$ from MD simulations of concentrated α-γ crystallin mixtures, showing neighboring α-α protein distributions as a function of mixing ratio, C_α. Key structural arrangements of the proteins that contribute to different peaks are also depicted (see text).The $g_{\alpha\alpha}(r)$ of the $C_\alpha = 0.5$ mixture for $u_{\alpha\gamma} = 0.55$ (line) and $u_{\alpha\gamma} = 0.9$ (dark diamonds) are compared in the inset. 37

2.10 Partial radial distribution functions $g_{\gamma\gamma}(r)$ from MD simulations of concentrated α-γ crystallin mixtures, showing neighboring γ-γ protein distributions as a function of mixing ratio, C_α. Key structural arrangements of the proteins that contribute to different peaks are also depicted (see text). . . 38

2.11 Partial radial distribution functions $g_{\alpha\gamma}(r)$ from MD simulations of concentrated α-γ crystallin mixtures, showing neighboring α-γ protein distributions as a function of mixing ratio, C_α. Key structural arrangements of the proteins that contribute to different peaks are also depicted (see text). . . 39

2.12 Molecular dynamics snapshots showing the progression from segregation of α-crystallin and γ-crystallin by type ($u_{\alpha\gamma} = 0$, Upper Left), through one phase, stable mixing ($u_{\alpha\gamma} = 0.55$, Middle Left), to separation of a dense phase of both proteins ($u_{\alpha\gamma} = 2.0$, Lower Right). Simulations performed at $\overline{T} = 0.7875$. 41

3.1 Schematic view of the orthonormal vectors $\mathbf{z}_{\pm}$ and the stability indicator α. The instability will be predominantly of demixing type when α is close to 0 and of condensation type when α is close to $\pm\pi/2$ 60

3.2 PT phase diagram of the symmetric binary mixture at $x = 0.5$ representing the possible topologies of phase diagrams (I,II-α, II-β and III for $\delta = 0.8, 0.65, 0.7$ and 0.5 respectively). Beyond the λ-line, the fluid demixes in two phases of same density but with concentrations $\overline{x}$ and $1-\overline{x}$. Depending on δ, critical points (CP), critical end points (CEP), tricritical points (TCP) and triple points (TP) can occur. The tendency for the solution to demix is enhanced when lowering δ. 66

3.3 Projection of the critical lines in the $\rho-x$ plane (upper panel) and $x-T$ plane (lower panel) for $\delta = 0.5$ as obtained from perturbation theory, HRT and MF calculations. The PT critical lines lay in between MF and the more accurate HRT results in both projections. The stability indicator α is also drawn on the PT critical line ($0 < |\alpha| < \pi/2$). For $\alpha = 0$, fluctuations in concentration x are driving the phase separation and demixing is found, as observed at x=1/2. When $|\alpha| = \pi/2$, the system becomes critical because of density fluctuations and L-V transition occurs, as found in the one component limits ($x = 0$ and $x = 1$). 68

3.4 Projection of the PT phase diagram of the $\delta = 0.7$ symmetric binary mixture onto the $x - \rho$ plane. The critical lines (CL_i) are drawn in red and the 4 coexistence surfaces (S_i) are represented schematically in light blue dashed lines. In order to obtain the coexistence surface, we calculated coexisting states (two or three phases can coexist). Some tie lines joining the coexisting phases are drawn (dash thin lines). The green dots (and green line) are coexisting phases that join at CL_2 and CL_3, and the critical end points (CEP) of CL_2 and CL_3 are also drawn (blue squares). The dashed red line is the mixing-demixing λ line (CL_1). The dashed lines (L_2 and L_3) are solution of Eq. 3.34 but located below the coexistence surface. The large red dots represent the triple line. 71

3.5 The four different archetypes of phase diagrams for the symmetric binary mixture are depicted ($\delta = 0.8, 0.7, 0.65, 0.5$). The projection of the critical lines onto the $x - \rho$ plane and cuts of the instability surface for different temperatures (0.8 to 1.24 by steps of 0.02) are shown. The transition between the two subtypes of topology II ($\delta = 0.70$ and $\delta = 0.65$) is found around $\delta = 0.6694$. The critical end points are represented by small squares. The value of the stability indicator α on the critical lines is also shown (according to the scale introduced on Fig. 3.3). 73

3.6 Phase behaviour of type II-α phase diagram ($\delta = 0.65$) of the symmetric mixture for different $\Delta = d_2/d_1$ ratios. The projection of the critical lines onto the $x - \rho$ plane and cuts of the instability surface for different temperatures (0.8 to 1.24 by steps of 0.02) are shown for $\Delta = 1, 1.03, 1.1, 1.15$ as indicated on the panels. The λ-line of the demixing transition is connected to the LV critical point of the pure small component solution ($x = 1$) for $\Delta > 1$. The squares are estimates of the critical end points CEP locations. 77

3.7 Phase behaviour of archetype II-β phase diagram ($\delta = 0.7$) of the symmetric mixture for different $\Delta = d_2/d_1$ ratios. The projection of the critical lines onto the $x - \rho$ plane and cuts of the instability surface for different temperatures (0.8 to 1.24 by steps of 0.02) are shown for $\Delta = 1, 1.03, 1.2, 1.25$ as indicated on the panels. The squares show the critical end points (CEP). For $\Delta = 1.25$ the λ line connects the LV critical point of the pure small component solution ($x = 1$). 78

3.8 Phase behaviour of archetype III ($\epsilon_{ij} = 0.5$) is depicted in the lower panels for $\Delta = 1, 1.15$ (left and right respectively). The $\epsilon_{ij} = 0.8$ case is shown in the upper panels ($\Delta = 1, 1.25$, left and right respectively). The projection of the critical lines onto the $x - \rho$ plane and cuts of the instability surface for different temperatures (0.6 to 1.6 by step of 0.03 for $\epsilon_{12} = 0.8$ and 0.88 to 1.24 by steps of 0.02 for type III) are drawn. 80

4.1 Attraction between α and γ lens crystallins affects the thermodynamic stability of their concentrated mixtures in a non-monotonic fashion. The red surface shows the highly elevated spinodal for hard-sphere interactions between α and γ, while the black and blue surfaces show, respectively, the suppressed and then re-elevated surfaces for square-well depths 1 and 2 k_BT. The spinodal of the pure γ-mixture is also drawn (open dots). The lines at the bottom of the figure indicate ϕ_α values for the 2d-cuts of the stability boundary surface presented in Fig. 4.2. The dark squares correspond to the mixing ratios C_α of the mixtures on which the SANS experiments were performed and the experimental plane (dark rectangle) is also drawn. . . . 87

4.2 2D-cut at constant ϕ_α of the instability surfaces for different values of the interaction $u_{\alpha\gamma} = 0$, 1, 2. The values of ϕ_α are indicated in each panel. The upper left panel shows the coexistence curve of the one component γ-mixture (dots) and the spinodal lines of the three mixtures are superimposed (dark line). 88

4.3 2D-section of the instability surface on the experimental $\overline{\phi}_\alpha$-$\phi_\gamma^{C_{PT}}$ line drawn in Fig. 4.1. The temperature T^* at which the mixtures become unstable is presented as a function of the relative mixing ratio C_α for values of $u_{\alpha\gamma}$ ranging from the hard sphere limit up to 2.5. 91

4.4 Temperature of instability T^* as a function of the interaction strength $u_{\alpha\gamma}$ for the mixing ratios $C_\alpha = 0.125, 0.25, 0.5$ (dashed line on Fig. 4.3). The stable region obtained from the MD simulations for the $C_\alpha = 0.5$ case and the critical temperature of the pure γ-mixture (dashed line) are also drawn. Fig. 2.6 is reproduced in the inset for comparison: the dots are here the calculated scattering intensities at low q vector ($q^* = 0.0467\, nm^{-1}$) for the $C_\alpha = 0.5$ mixture. 93

4.5 The spinodal surface changes dramatically as the $\alpha - \gamma$ attraction strength, $u_{\alpha\gamma}$, increases. If $u_{\alpha\gamma}$ is slightly too low (left) or slightly to high (right), MD simulations (cube) that are otherwise appropriate for modeling $\alpha - \gamma$ mixtures (center) were found to be unstable. This finding is consistent with the fact that these unstable simulation conditions are indeed under the perturbation theory spinodals as shown. 94

4.6 2D-Cut of the spinodal surface at $T = 0.98T_\gamma^{C_{PT}}$ for $u_{\alpha\gamma} = 0, 0.5, 1, 2$. The experimental tie lines pairs (full circles and dashed lines) were taken from [Thurston, 2006]. 95

4.7 The stability diagram presented in Fig. 4.4 is reproduced here: the instability temperature T^* as a function of the interaction strength $u_{\alpha\gamma}$ for the mixing ratios $C_\alpha = 0.25, 0.5$ (dashed line on Fig. 4.3) is shown. The stable region obtained from the MD simulations for the $C_\alpha = 0.5$ case and the critical temperature of the pure γ-mixture (dashed line) are also drawn. We investigate the coexistence surface of four different mixtures (denoted A, B, C and D with $u_{\alpha\gamma} = 1.2, 1.1, 1.0$ and 0.85 respectively). These $u_{\alpha\gamma}$ values fall in the stable region defined by the PT calculations of the spinodal surface, i.e. their instability boundary is located at very low temperature. Moreover, the spinodal of mixtures A, B and C is almost identical and the maximum spinodal temperature is found close to $T_\gamma^{C_{PT}}$ for all three mixtures. 97

4.8 Cuts of the spinodal surface for mixtures A-B-C defined in Fig. 4.7 ($u_{\alpha\gamma} = 1.2, 1.1$ and 1.0 respectively) at different temperatures (T=0.89, 0.87, 0.85, 0.82, 0.8). The 3D plot of the spinodals is also presented in the last panel. Closed to $T_\gamma^{C_{PT}} = 0.9$ the A-B-C spinodals are very similar and the maximum instability temperature is located close to the critical point of the pure γ solution for all mixtures. 99

4.9 Cut of the coexistence surface at $T = 0.844$ (slightly below $T_\gamma^{C_{PT}} = 0.9$) for mixtures A-B-C defined in Fig. 4.7. The tie lines (TL_A,TL_B and TL_C) obtained quenching the three mixtures from the same initial state $(\phi_\gamma^0, \phi_\alpha^0)$ are shown. For mixture A, high density mixed phases (phase II) coexist with low density mixed phases (phase I). For $u_{\alpha\gamma} = 1.1$ the tie lines are almost parallel to the ϕ_γ axis. By decreasing $u_{\alpha\gamma}$ slightly more (mixture C) tie lines with opposite tilts with respect to mixture A are found: almost pure and dense γ (II) coexist with mixed α-γ phases of lower density (I). While the phase separation process of the three mixtures is totally different, the cuts of the coexistence surface are almost indistinguishable. 100

4.10 Cut of the coexistence surface at $T = 0.844$ (slightly below $T_\gamma^{C_{PT}} = 0.9$) for mixture A defined in Fig. 4.7. High density mixed phases (phase II) coexist with low density mixed phases (phase I). The composition of phases I and II for tie line TL_A is represented in the snapshots. Both αs and γs are present in the two phases. 101

4.11 The phase behaviour of mixture A defined in Fig. 4.7 is shown. The cuts of the coexistence surface have been performed at temperatures slightly below $T_\gamma^{C_{PT}} = 0.9$. The full circles represent the cuts of the binodal surface at $T = 0.82, 0.83, 0.84, 0.86$, and the corresponding cut of the spinodal are also drawn (small dots). Some tie lines (dashed lines) connecting coexisting states are shown. For each temperature cut, the critical point (square) is determined by extrapolation of the coexisting points and their intersection with the spinodal. This forms a line of critical points that moves towards higher ϕ_α and lower ϕ_γ when the temperature is reduced. 103

4.12 Cut of the coexistence surface at $T = 0.844$ (slightly below $T_{\gamma}^{C_{PT}} = 0.9$) for mixture B defined in Fig. 4.7. The tie lines are almost parallel to the ϕ_{γ} axis. The snapshots representing the two coexisting phases of TL_B are drawn. Both components are present in the two phases and $\phi_{\alpha}^{I} \simeq \phi_{\alpha}^{II}$. Fluctuations in ρ_{γ} only are responsible for the phase transition. 105

4.13 Cut of the coexistence surface at $T = 0.844$ (slightly below $T_{\gamma}^{C_{PT}} = 0.9$) for mixture C defined in Fig. 4.7. Tie lines with opposite tilts with respect to mixture A are found: almost pure and dense γ (type II) coexist with mixed α-γ phases of lower density (type I). The snapshots representing the two coexisting phases of TL_C are drawn. 106

4.14 Cuts of the coexistence surface of mixture D at temperatures T=0.82, 0.88, 0.89 and 0.91 are presented (circles) with the corresponding spinodal (full and dotted lines) and some of the tie lines (dashed lines). The spinodals for higher T (up to T=0.93) are also shown (dashed lines). The experimental tie lines pairs (full diamonds and dashed lines) were taken from [Thurston, 2006]. Estimations of the critical points (squares) are shown as well. The critical points are shifting towards higher ϕ_{α} and ϕ_{γ} with increasing temperature. 107

Bibliography

V. J. Anderson and H. N. W. Lekkerkerker. Insights into phase transition kinetics from colloid science. *Nature*, 416:811–815, 2002.

O. Antonevych, F. Forstmann, and E. Diaz-Herrera. Phase diagram of symmetric binary fluid mixtures: first-order or second-order demixing. *Phys Rev E Stat Nonlin Soft Matter Phys*, 65(6 Pt 1):061504, Jun 2002.

N. Asherie, J. Pande, A. Lomakin, O. Ogun, S. R. Hanson, J. B. Smith, and G. B. Benedek. Oligomerization and phase separation in globular protein solutions. *Biophys Chem*, 75 (3):213–227, Dec 1998.

J. A. Barker and D. Henderson. Perturbation theory and equation of state for fluids: The square-well potential. *The Journal of Chemical Physics*, 47(8):2856–2861, 1967. URL `http://link.aip.org/link/?JCP/47/2856/1`.

S. Bassnett. On the mechanism of organelle degradation in the vertebrate lens. *Exp*

Eye Res, Sep 2008. doi: 10.1016/j.exer.2008.08.017. URL http://dx.doi.org/10.1016/j.exer.2008.08.017.

G. B. Benedek. Theory of transparency of the eye. *Applied Optics*, 10(3):459–473, 1971.

G. B. Benedek. Cataract as a protein condensation disease: the Proctor Lecture. *Invest Ophthalmol Vis Sci*, 38(10):1911–1921, Sep 1997.

S. Bera and S. K. Ghosh. Interaction of h+-ions with [alpha]-crystallin: solvent accessibility of ionizable side chains and surface charge. *Biophysical Chemistry*, 70(2):147–160, Feb. 1998. URL http://www.sciencedirect.com/science/article/B6TFB-3SR3CN5-6/1/6f37bbb905bc1b6ca78cf71345a0d1e4.

C. R. Berland, G. M. Thurston, M. Kondo, M. L. Broide, J. Pande, O. Ogun, and G. B. Benedek. Solid-liquid phase boundaries of lens protein solutions. *Proc Natl Acad Sci U S A*, 89(4):1214–1218, Feb 1992.

F. A. Bettelheim, R. Ansari, Q.-F. Cheng, and J. S. Zigler. The mode of chaperoning of dithiothreitol-denatured [alpha]-lactalbumin by [alpha]-crystallin. *Biochemical and Biophysical Research Communications*, 261(2):292–297, Aug. 1999. URL http://www.sciencedirect.com/science/article/B6WBK-45K1D1V-1P1/2/15b1c04d6e78b92cbde8049a032ddd70.

T. Biben and J.-P. Hansen. Phase separation of asymmetric binary hard-sphere fluids. *Phys. Rev. Lett.*, 66:2215–2218, 1991.

H. Bloemendal, W. de Jong, R. Jaenicke, N. H. Lubsen, C. Slingsby, and A. Tardieu. Ageing and vision: structure, stability and function of lens crystallins. *Prog Biophys Mol Biol*, 86(3):407–485, Nov 2004. doi: 10.1016/j.pbiomolbio.2003.11.012. URL http://dx.doi.org/10.1016/j.pbiomolbio.2003.11.012.

T. Blundell, P. Lindley, L. Miller, D. Moss, C. Slingsby, I. Tickle, B. Turnell, and G. Wistow. The molecular structure and stability of the eye lens: X-ray analysis of [gamma]-crystallin ii. *Nature*, 289(5800):771–777, Feb. 1981. URL `http://dx.doi.org/10.1038/289771a0`.

M. Bostrom, D. Williams, and B. Ninham. The influence of ionic dispersion potentials on counterion condensation on polyelectrolytes. *J. Phys. Chem. B*, 106(32):7908–7912, 2002. URL `http://pubs3.acs.org/acs/journals/doilookup?in_doi=10.1021/jp0256084`.

T. Boublík. Hard-sphere equation of state. *J. Chem. Phys.*, 53:471–472, 1970.

D. Boyle, S. Gopalakrishnan, and L. Takemoto. Localization of the chaperone binding site. *Biochem Biophys Res Commun*, 192(3):1147–1154, May 1993. doi: 10.1006/bbrc.1993.1536. URL `http://dx.doi.org/10.1006/bbrc.1993.1536`.

M. L. Broide, C. R. Berland, J. Pande, O. O. Ogun, and G. B. Benedek. Binary-liquid phase separation of lens protein solutions. *Proc Natl Acad Sci U S A*, 88(13):5660–5664, Jul 1991.

C. Caccamo. Integral equation theory description of phase equilibria in classical fluids. *Phys. Rep.*, 274:1–105, 1996.

F. Cardinaux, T. Gibaud, A. Stradner, and P. Schurtenberger. Interplay between spinodal decomposition and glass formation in proteins exhibiting short-range attractions. *Phys Rev Lett*, 99(11):118301, Sep 2007.

N. Carnahan and K. Starling. Equation of state for nonattracting rigid spheres. *J. Chem. Phys.*, 51:635–636, 1969.

D. Chan, T. W. Healy, and L. R. White. Electrical double layer interactions under regulation by surface ionization equilibriaŰdissimilar amphoteric surfaces. *J. Chem. Soc. Faraday Trans. 1*, 72:2844 – 2865, 1976.

X. S. Chen and F. Forstmann. The demixing and gas–liquid instability of a binary yukawa fluid. *The Journal of Chemical Physics*, 97(5):3696–3703, 1992.

P. Csermely. Chaperone overload is a possible contributor to 'civilization diseases'. *Trends Genet*, 17(12):701–704, Dec 2001.

L. C. D. Pitts, J. Jose, S. Lorman, E. Moss, S. Varma, S. Zigler, S. Zigman, and J. Zuclich. *Optical Radiation and Visual Health.* CRC Press, Boca Raton, FL, 1986.

K. A. Dawson, G. Foffi, F. Sciortino, P. Tartaglia, and E. Zaccarelli. Mode-coupling theory of colloids with short-range attractions. *J. Phys,: Condens. Matt.*, 13:9113, 2001.

M. Delaye and A. Tardieu. Short-range order of crystallin proteins accounts for eye lens transparency. *Nature*, 302(5907):415–417, 1983.

C. DeMichele, S. Gabrielli, P. Tartaglia, and F. Sciortino. Dynamics in the presence of attractive patchy interactions. *J. Phys. Chem. B*, 110(15):8064–8079, Apr. 2006. ISSN 1520-6106. URL http://pubs3.acs.org/acs/journals/doilookup?in_doi=10.1021/jp056380y.

N. Dorsaz, G. Thurston, A. Stradner, P. Schurtenberger, and G. Foffi. Spinodal surface of a free energy model for eye lens protein mixtures: Relevance for cataracts. volume 1091, pages 246–248. AIP, 2009a. doi: 10.1063/1.3082294. URL http://link.aip.org/link/?APC/1091/246/1.

N. Dorsaz, G. M. Thurston, A. Stradner, P. Schurtenberger, and G. Foffi. Colloidal characterization and thermodynamic stability of binary eye lens protein mixtures. *The Journal* *of Physical Chemistry B*, 113(6):1693–1709, 2009b. URL http://pubs.acs.org/doi/abs/10.1021/jp807103f.

I. Ferris, Frederick L. and J. M. Tielsch. Blindness and visual impairment: A public health issue for the future as well as today. *Arch Ophthalmol*, 122(4):451–452, 2004. URL http://archopht.ama-assn.org.

B. M. Fine, A. Lomakin, O. O. Ogun, and G. B. Benedek. Static structure factor and collective diffusion of globular proteins in concentrated aqueous solution. *The Journal of Chemical Physics*, 104(1):326–335, 1996. doi: 10.1063/1.470904. URL http://link.aip.org/link/?JCP/104/326/1.

S. Finet and A. Tardieu. ?-crystallin interaction forces studied by small angle x-ray scattering and numerical simulations. *Journal of Crystal Growth*, 232(1-4):40–49, 2001.

G. Foffi, K. A. Dawson, S. V. Buldyrev, F. Sciortino, E. Zaccarelli, and P. Tartaglia. Evidence for unusual dynamical arrest scenario in short ranged colloidal systems. *Phys. Rev. E*, 65:050802(R), 2002a.

G. Foffi, G. D. McCullagh, A. Lawlor, E. Zaccarelli, K. A. Dawson, F. Sciortino, P. Tartaglia, D. Pini, and G. Stell. Phase equilibria and glass transition in colloidal systems with short-ranged attractive interactions: Application to protein crystallization. *Phys. Rev. E*, 65:31407, 2002b.

D. Frenkel. Playing tricks with designer “atoms”. *Science*, 296:65–66, 2002.

D. C. G Pellicane and C. Caccamo. Theory and simulation of short-range models of globular protein solutions. *Journal of Physics: Condensed Matter*, 16(42):S4923–S4936, 2004. URL http://stacks.iop.org/0953-8984/16/S4923.

A. P. Gast, W. B. Russell, and C. K. Hall. Polymer-induced phase separations in nonaqueous colloidal suspensions. *J. Colloid Interface Sci.*, 96:251–67, 1983.

A. Gil-Villegas, A. Galindo, P. J. Whitehead, S. J. Mills, G. Jackson, and A. N. Burgess. Statistical associating fluid theory for chain molecules with attractive potentials of variable range. *The Journal of Chemical Physics*, 106(10):4168–4186, 1997. URL `http://link.aip.org/link/?JCP/106/4168/1`.

O. Glatter. A new method for the evaluation of small-angle scattering data. *Journal of Applied Crystallography*, 10(5):415–421, Oct 1977. doi: 10.1107/S0021889877013879. URL `http://dx.doi.org/10.1107/S0021889877013879`.

J. N. Goldman and G. B. Benedek. The relationship between morphology and transparency in the nonswelling corneal stroma of the shark. *Invest Ophthalmol*, 6(6):574–600, Dec 1967.

E. W. Grundke and D. Henderson. Distribution functions of multi-component fluid mixtures of hard spheres. *Molecular Physics*, 24(2):269–281, 1972. URL `http://www.informaworld.com/10.1080/00268977200101431`.

F. G. Guinier A. *Small-angle sctattering of X-rays.* New York: Wiley, 1955.

J.-P. Hansen and I. R. McDonald. *Theory of Simple Liquids.* Academic Press, London, 2nd edition, 1986.

D. Henderson and E. W. Grundke. Direct correlation function: Hard sphere fluid. *J. Chem. Phys.*, 63:601–607, 1975.

J. Horwitz. Alpha-crystallin can function as a molecular chaperone. *Proc Natl Acad Sci U S A*, 89(21):10449–10453, Nov 1992.

J. G. Kirkwood and J. B. Shumaker. The influence of dipole moment fluctuations on the dielectric increment of proteins in solution. *Proceedings of the National Academy of Sciences*, 38(10):855–862, 1952. URL `http://www.pnas.org`.

R. Klein. Neutrons, x-rays and light: Scattering methods applied to soft condensed matter, 2002.

V. S. Kumaraswamy, P. F. Lindley, C. Slingsby, and I. D. Glover. An Eye Lens Protein–Water Structure: 1.2 Å Resolution Structure of γB-Crystallin at 150 K. *Acta Crystallographica Section D*, 52(4):611–622, Jul 1996. doi: 10.1107/S0907444995014302. URL `http://dx.doi.org/10.1107/S0907444995014302`.

J. Köfinger, N. B. Wilding, and G. Kahl. Phase behavior of a symmetrical binary fluid mixture. *J Chem Phys*, 125(23):234503, Dec 2006. doi: 10.1063/1.2393241. URL `http://dx.doi.org/10.1063/1.2393241`.

J. L. Lebowitz. Exact solution of generalized percus-yevick equation for a mixture of hard spheres. *Phys. Rev.*, 133:A895–A899, 1964.

B. P. Lee and M. E. Fisher. Density fluctuations in an electrolyte from generalized debye-h&uuml;ckel theory. *Phys. Rev. Lett.*, 76(16):2906–, Apr. 1996. URL `http://link.aps.org/abstract/PRL/v76/p2906`.

L. L. Lee and D. Levesque. Perturbation theory for mixtures of simple liquids. *Molecular Physics*, 26(6):1351–1370, 1973. URL `http://www.informaworld.com/10.1080/00268977300102531`.

S. Lerman, S. Zigman, and W. F. Forbes. Properties of a cryoprotein in the ocular lens. *Biochem Biophys Res Commun*, 22(1):57–61, Jan 1966.

M. E. Leunissen, C. G. Christova, A.-P. Hynninen, C. P. Royall, A. I. Campbell, A. Imhof, M. Dijkstra, R. van Roij, and A. van Blaaderen. Ionic colloidal crystals of oppositely charged particles. *Nature*, 437(7056):235–240, Sept. 2005. ISSN 0028-0836. URL `http://dx.doi.org/10.1038/nature03946`.

J. N. Liang and X. Y. Li. Interaction and aggregation of lens crystallins. *Exp Eye Res*, 53 (1):61–66, Jul 1991.

C. N. Likos. Effective interactions in soft condensed matter physics. *Physics Reports*, 348: 267–439, 2001.

C. Liu, N. Asherie, A. Lomakin, J. Pande, O. Ogun, and G. B. Benedek. Phase separation in aqueous solutions of lens gamma-crystallins: special role of gamma s. *Proc Natl Acad Sci U S A*, 93(1):377–382, Jan 1996.

C. Liu, J. Pande, A. Lomakin, O. Ogun, and G. B. Benedek. Aggregation in aqueous solutions of bovine lens gamma-crystallins: special role of gamma(s). *Invest Ophthalmol Vis Sci*, 39(9):1609–1619, Aug 1998.

J. Liu, N. B. Wilding, and E. Luijten. Simulation of phase transitions in highly asymmetric fluid mixtures. *Physical Review Letters*, 97(11):115705, 2006. doi: 10.1103/PhysRevLett.97.115705. URL `http://link.aps.org/abstract/PRL/v97/e115705`.

A. Lomakin, N. Asherie, and G. B. Benedek. Monte carlo study of phase separation in aqueous protein solutions. *The Journal of Chemical Physics*, 104(4):1646–1656, 1996. URL `http://link.aip.org/link/?JCP/104/1646/1`.

A. Lomakin, N. Asherie, and G. B. Benedek. Aeolotopic interactions of globular proteins. *Proc Natl Acad Sci U S A*, 96(17):9465–9468, Aug 1999.

A. A. Louis. Effective potentials for polymers and colloids: beyond the van der waals picture of fluids? *Phil. Trans. R. Soc. A*, 359(1782):939–960, May 2001. URL `http://dx.doi.org/10.1098/rsta.2000.0804`.

M. Malfois, F. BonnetÃĺ, L. Belloni, and A. Tardieu. A model of attractive interactions to account for fluid-fluid phase separation of protein solutions. *Journal of Chemical Physics*, 105(8):3290–3300, 1996.

G. A. Mansoori, N. F. Carnahan, K. E. Starling, and J. T. W. Leland. Equilibrium thermodynamic properties of the mixture of hard spheres. *The Journal of Chemical Physics*, 54(4):1523–1525, 1971. URL `http://link.aip.org/link/?JCP/54/1523/1`.

D. Maurice. *J. Physiol.*, 136:263, 1957.

D. A. McQuarrie. *Statistical Mechanics*. Number Sec. 15-1. 1976.

M. Muschol and F. Rosenberger. Liquid–liquid phase separation in supersaturated lysozyme solutions and associated precipitate formation/crystallization. *The Journal of Chemical Physics*, 107(6):1953–1962, 1997. doi: 10.1063/1.474547. URL `http://link.aip.org/link/?JCP/107/1953/1`.

S. Najmudin, V. Nalini, H. P. Driessen, C. Slingsby, T. L. Blundell, D. S. Moss, and P. F. Lindley. Structure of the bovine eye lens protein gammab(gammaii)-crystallin at 1.47 a. *Acta Crystallogr D Biol Crystallogr*, 49(Pt 2):223–233, Mar 1993. doi: 10.1107/S0907444992007601. URL `http://dx.doi.org/10.1107/S0907444992007601`.

M. Noro and D. Frenkel. Extended corresponding-states behavior for particles with variable range attractions. *J.Chem.Phys.*, 113:2941, 2000.

P. Paricaud. A general perturbation approach for equation of state development: applications to simple fluids, ab initio potentials, and fullerenes. *J Chem Phys*, 124(15):

154505, Apr 2006. doi: 10.1063/1.2181979. URL http://dx.doi.org/10.1063/1.2181979.

Parola and Reatto. Hierarchical reference theory of fluids and the critical point. *Phys Rev A*, 31(5):3309–3322, May 1985.

Parola and Reatto. Microscopic approach to critical phenomena in binary fluids. *Phys Rev A*, 44(10):6600–6615, Nov 1991.

A. Parola and L. Reatto. Liquid state theories and critical phenomena. *Advances in Physics*, 44:211, 1995.

J. S. Pedersen, D. Posselt, and K. Mortensen. Analytical treatment of the resolution function for small-angle scattering. *Journal of Applied Crystallography*, 23(4):321–333, Aug 1990. doi: 10.1107/S0021889890003946. URL http://dx.doi.org/10.1107/S0021889890003946.

R. Piazza. Interactions and phase transitions in protein solutions. *Current Opinion in Colloid and Interface Science*, 5(1-2):38–43, 2000.

R. Piazza. Protein interactions and association: An open challenge for colloid science. *Current Opinion in Colloid and Interface Science*, 8(6):515–522, 2004.

V. Pigaga and R. A. Quinlan. Lenticular chaperones suppress the aggregation of the cataract-causing mutant t5p gamma c-crystallin. *Exp Cell Res*, 312(1):51–62, Jan 2006. doi: 10.1016/j.yexcr.2005.09.014. URL http://dx.doi.org/10.1016/j.yexcr.2005.09.014.

D. Pini, G. Stell, and N. B. Wilding. A liquid-state theory that remains successful in the critical region. *Mol. Phys.*, 95:483–494, 1998b.

D. Pini, M. Tau, A. Parola, and L. Reatto. Phase diagram of symmetric binary mixtures at equimolar and nonequimolar concentrations: a systematic investigation. *Phys Rev E Stat Nonlin Soft Matter Phys*, 67(4 Pt 2):046116, Apr 2003.

A. Ponce, C. Sorensen, and L. Takemoto. Role of short-range protein interactions in lens opacifications. *Mol Vis*, 12:879–884, 2006.

W. Poon. PHYSICS: Colloids as Big Atoms. *Science*, 304(5672):830–831, 2004. doi: 10.1126/science.1097964. URL `http://www.sciencemag.org`.

T. Putilina, F. Skouri-Panet, K. Prat, N. H. Lubsen, and A. Tardieu. Subunit exchange demonstrates a differential chaperone activity of calf alpha-crystallin toward beta LOW- and individual gamma-crystallins. *J Biol Chem*, 278(16):13747–13756, Apr 2003. doi: 10.1074/jbc.M208157200. URL `http://dx.doi.org/10.1074/jbc.M208157200`.

D. C. Rapaport. *The Art of Molecular Dynamic Simulation*. Cambridge University Press, 1995.

E. Scholl-Paschinger and G. Kahl. Self-consistent ornstein–zernike approximation for a binary symmetric fluid mixture. *The Journal of Chemical Physics*, 118(16):7414–7424, 2003. URL `http://link.aip.org/link/?JCP/118/7414/1`.

Schurtenberger, Chamberlin, Thurston, Thomson, and Benedek. Observation of critical phenomena in a protein-water solution. *Phys Rev Lett*, 63(19):2064–2067, Nov 1989.

P. Schurtenberger, R. A. Chamberlin, G. M. Thurston, J. A. Thomson, and G. B. Benedek. Observation of critical phenomena in a protein-water solution. *Phys. Rev. Lett.*, 71(20): 3395–, Nov. 1993. URL `http://link.aps.org/abstract/PRL/v71/p3395`.

E. Schöll-Paschinger, A. L. Benavides, and R. Castañeda-Priego. Vapor-liquid equilibrium and critical behavior of the square-well fluid of variable range: a theoretical study. *J*

Chem Phys, 123(23):234513, Dec 2005. doi: 10.1063/1.2137713. URL http://dx.doi.org/10.1063/1.2137713.

R. P. Sear. Phase behavior of a simple model of globular proteins. *J. Chem. Phys*, 111: 4800–4806, 1999.

I. Shand-Kovach. PhD thesis, M.I.T., 1992.

R. J. Siezen, M. R. Fisch, C. Slingsby, and G. B. Benedek. Opacification of gamma-crystallin solutions from calf lens in relation to cold cataract formation. *Proc Natl Acad Sci U S A*, 82(6):1701–1705, Mar 1985.

A. Spector, T. Freund, L. K. Li, and R. C. Augusteyn. Age-dependent changes in the structure of alpha crystallin. *Invest Ophthalmol*, 10(9):677–686, Sep 1971.

A. Stradner, V. Lobaskin, P. Schurtenberger, and G. Thurston. *Structure and interactions of lens proteins in dilute and concentrated solutions*. 2004a. URL http://dx.doi.org/10.1007/b93990.

A. Stradner, H. Sedgwick, F. Cardinaux, W. C. K. Poon, S. U. Egelhaaf, and P. Schurtenbergerpiazza. Equilibrium cluster formation in concentrated protein solutions and colloids. *Nature*, 432(7016):492–495, Nov 2004b. doi: 10.1038/nature03109. URL http://dx.doi.org/10.1038/nature03109.

A. Stradner, G. Foffi, N. Dorsaz, G. Thurston, and P. Schurtenberger. New insight into cataract formation: enhanced stability through mutual attraction. *Phys Rev Lett*, 99 (19):198103, Nov 2007.

L. J. Takemoto and A. A. Ponce. Decreased association of aged alpha crystallins with gamma crystallins. *Exp Eye Res*, 83(4):793–797, Oct 2006. doi: 10.1016/j.exer.2006.03.020. URL http://dx.doi.org/10.1016/j.exer.2006.03.020.

T. Tanaka and G. B. Benedek. Observation of protein diffusivity in intact human and bovine lenses with application to cataract. *Invest Ophthalmol*, 14(6):449–456, Jun 1975.

P. R. ten Wolde and D. Frenkel. Enhancement of protein crystal nucleation by critical density fluctuations. *Science*, 277:1975–1978, 1997.

J. A. Thomson, P. Schurtenberger, G. M. Thurston, and G. B. Benedek. Binary liquid phase separation and critical phenomena in a protein/water solution. *Proc Natl Acad Sci U S A*, 84(20):7079–7083, Oct 1987.

G. M. Thurston. Liquid-liquid phase separation and static light scattering of concentrated ternary mixtures of bovine alpha and gamma b crystallins. *The Journal of Chemical Physics*, 124(13):134909, 2006. URL `http://link.aip.org/link/?JCP/124/134909/1`.

G. M. Thurston, D. L. Hayden, P. Burrows, J. I. Clark, V. G. Taret, J. Kandel, M. Courogen, J. A. Peetermans, M. S. Bowen, D. Miller, K. M. Sullivan, R. Storb, H. Stern, and G. B. Benedek. Quasielastic light scattering study of the living human lens as a function of age. *Curr Eye Res*, 16(3):197–207, Mar 1997.

L. Tisza. *Generalized Thermodynamics.* Cambridge, MIT, MA, 1966.

C. P. Ursenbach and G. N. Patey. Stability of binary mixtures: Supersaturation limits of aqueous alkali halide solutions. *The Journal of Chemical Physics*, 100(5):3827–3842, 1994.

P. van Konynenburg and R. Scott. Critical lines and phase equilibria in binary van der waals mixtures. *Royal Society of London Philosophical Transactions Series A*, 298:495–540, 1980.

L. Vega, E. de Miguel, and L. F. Rull. Phase equilibria and critical behavior of square-well fluids of variable width by gibbs ensemble monte carlo simulation. *J. Chem. Phys.*, 96 (3):2296–2305, 1992.

F. Vérétout and A. Tardieu. The protein concentration gradient within eye lens might originate from constant osmotic pressure coupled to differential interactive properties of crystallins. *Eur Biophys J*, 17(2):61–68, 1989.

F. Veretout, M. Delaye, and A. Tardieu. Molecular basis of eye lens transparency. Osmotic pressure and X-ray analysis of alpha-crystallin solutions. *J Mol Biol*, 205(4):713–728, Feb 1989.

L. Verlet and J.-J. Weis. Equilibrium theory of simple liquids. *Phys. Rev. A*, 5:939–952, 1972.

E. J. W. Verwey and J. T. G. Overbeek. Theory of the stability of lyophobic colloids. the interaction of particles having an electric double layer. *Journal of Polymer Science*, 4: 413–414, 1949.

WHO. Global initiative for the elimination of avoidable blindness : action plan 2006-2011. WHO Library Cataloguing-in-Publication Data, 2007.

B. Widom. Some topics in the theory of fluids. *The Journal of Chemical Physics*, 39 (11):2808–2812, 1963. doi: 10.1063/1.1734110. URL `http://link.aip.org/link/?JCP/39/2808/1`.

N. B. Wilding, F. Schmid, and P. Nielaba. Liquid-vapor phase behavior of a symmetrical binary fluid mixture. *Phys. Rev. E*, 58(2):2201–, Aug. 1998. URL `http://link.aps.org/abstract/PRE/v58/p2201`.

E. Zaccarelli. Colloidal gels: equilibrium and non-equilibrium routes. *Journal of Physics: Condensed Matter*, 19(32):323101 (50pp), 2007. URL `http://stacks.iop.org/0953-8984/19/323101`.

S. Zigman and S. Lerman. A cold precipitable protein in the lens. *Nature*, 203(4945): 662–663, Aug. 1964. URL `http://dx.doi.org/10.1038/203662a0`.

B. Zoetekouw and R. van Roij. Nonlinear screening and gas-liquid separation in suspensions of charged colloids. *Physical Review Letters*, 97(25):258302, 2006. doi: 10.1103/PhysRevLett.97.258302. URL `http://link.aps.org/abstract/PRL/v97/e258302`.

R. Zwanzig. High-temperature equation of state by a perturbation method. i. nonpolar gases. *The Journal of Chemical Physics*, 22(8):1420–1426, 1954. doi: 10.1063/1.1740409. URL `http://link.aip.org/link/?JCP/22/1420/1`.

Acknowledgments

Above all, I would like to thank prof. Baldereschi and prof. Giuseppe Foffi who gave me the opportunity to do research at IRRMA during the last five years. I am also very grateful to both of them to allow me to participate to so many conferences and summerchools around Europe that have contributed to my scientific and personal development. I thank Giuseppe for the great work together: I really learned a lot and enjoyed that period, from both a personal and a professional point of view. I would also thank Prof. Baldereschi for his support during this thesis.

Thanks also to Anna Stradner and Prof. Peter Schurtenberger for the continuous and fruitful collaboration and lots of interesting discussions in the coffee room of their department in Fribourg. I would also thank Prof. George Thurston for interesting and always enthousiastic discussions, and also for its careful re-reading of a quite long draft.

I thank Prof. Paolo de Los Rios and Francesco Piazza for an interesting collaboration, motivating discussions and enjoyable lunches or coffe breaks on the seventh floor. It was also a pleasure to work with Cristiano de Michele at IRRMA for few months and visit him in Rome. I thank also prof. Kahl for hosting me in Vienna to learn more on the phase diagram of binary mixtures.

A special thanks also to all the people I met at IRRMA in the last four year (Fabien, Julien G., Audrius, Peter, Zeljko, Feliciano, Vincenzo, Costas, Andreas and Prof. Pasquarello) who made the atmosphere of the quite dark PPH more lively, with a special thanks to Vladan with whom I shared the office in the old PPH. I also thank for their help our secretary Noemi Porta and Florence Hagen, our system administrator. I would like to thank the last arrived in the GR-FO, Francesco and Davide, who made the writing period of this thesis more lively and cheerful, and also Carlo, Andy, Julien for enjoyable breaks in the 7 floor after our relocation to the BSP. Finally, I thank the *Maggica* for some great games at lunch time.

Curriculum Vitae

Nicolas Dorsaz

17/05/1981
Swiss and Italian

EPFL SB IRRMA-GE
BSP 124 (Bat. Sc. Phys. UNIL)
CH-1015 Lausanne
Switzerland

nicolas.dorsaz@epfl.ch
+41 (0)79 372 96 17

ACADEMIC FORMATION

2005 - 2009	***PhD in Computational Statistical Physics*** at the Institut Romand de Recherche Numérique en Physique des Matériaux (IRRMA), École Polytechnique fédérale de Lausanne (EPFL)
2000 - 2005	Master of Science in Physics, EPFL
1996 - 2000	High School, Maturité scientifique, Collège de Saussure, Geneva

RESEARCH EXPERIENCE

2005 - 2009	**PhD studies:** *A colloidal approach to Eye Lens protein mixtures: Relevance for cataract formation*
2005 - 2006	Experimental research in weightlessness: *Cavitation studies in Microgravity*, European Space Agency (ESA)
2004 - 2005	Master Thesis in Statistical Biophysics: *Simplified Model of Water on Lattice* Institute of Theoretical Physics [ITP], EPFL
2003	Summer project of two months: Analysis of radio-astronomic data, Max Planck Institt fur Radioastronomie, Bonn (D)

CONTRIBUTED and INVITED TALKS

- CECAM Workshop 2009, *New Trends in Simulating Colloids: from Models to Applications* (Lausanne, July 15-18, 2009)
- 10th Granada Seminar on Computational and Statistical Physics, *Modeling and Simulation of New Materials* (Granada, Sept. 15-19 2008)
- XII Sitges Conference on Statistical Mechanics, *Statistical Mechanics of Molecular Biophysics* (Sitges, June 2-6 2008)
- Annual meeting of the Swiss Physical Society (SPS) (Zurich, Feb. 2007)

SCHOOLS AND CONFERENCES

- Bombannes school on *Scattering Methods applied to Soft Condensed Matter* (Bombannes, June 7-14 2008)
- 21st Conference of the European Colloid and Interface society, Ecis 2007 (Geneva, Sept. 10-14 2007)
- XXIII IUPAP International Conference on Statistical Physics, Stat. Phys. 23 (Genova, July 9-13 2007)
- Satellite conference of Stat. Phys. 23, *Statics and Dynamics of Granular Media and Colloidal Suspensions* (Napoli, July 4-6 2007)
- V^{me} Séminaire Transalpin de Physique: *Dynamics and Statistics in Complex Systems* (Torino, February 26-March 2, 2007)
- Workshop on Dynamical Arrest of Soft Matter and Colloids (Lugano, April 6-8 2006)
- IV^{me} Séminaire Transalpin de Physique: *Nonequilibrium Statistical Mechanics* (Champex , March 5-11, 2006)
- Advanced Marie Curie course: *Understanding Molecular Simulations* (University of Amsterdam , October 24 - November 4, 2005)
- Summerschool : *Ageing and the Glass Transition* (University of Luxembourg, September 18-24, 2005)

PUBLICATIONS

1. N. Dorsaz, G. Thurston, A. Stradner, P. Schurtenberger and G.Foffi, ***Colloidal characterization and thermodynamic stability of binary eye lens protein mixtures*** , J. Phys. Chem. B, 113, 1693 (2009) See also JPCB Cover (Vol.113, Iss.6)

2. N. Dorsaz, G. Thurston, A. Stradner, P. Schurtenberger and G.Foffi, ***Spinodal surface of a free energy model for eye lens protein mixtures: Relevance for cataract***, AIP Conf. Proc., Volume 1091, pp. 246-248 (2009)
3. P. Kobel, D. Obreschkow, A. de Bosset, N. Dorsaz and M. Farhat, ***Techniques for generating centimetric drops in microgravity and application to cavitation studies***, Exp. in Fluids, 4151403 (2009)
4. A. Stradner, G.Foffi, N. Dorsaz, G. Thurston and P. Schurtenberger, ***New insight into cataract formation: Enhanced stability through mutual attraction***, Phys. Rev. Lett. 99, 198103 (2007) See also Physical Review Focus

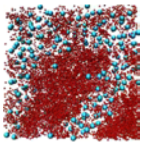

5. D. Obreschkow, P. Kobel, N. Dorsaz, A. de Bosset, C. Nicollier, and M. Farhat, ***Cavitation Bubble Dynamics inside Liquid Drops in Microgravity***, Phys. Rev. Lett. 97, 094502 (2006). See also Cavitation in Microgravity (Movie)
6. G. Foffi, N. Dorsaz and C. De Michele, ***Gel and Glass Transitions in Short-range Attractive Colloidal Systems***, in Food Colloids: Self-Assembly and Material Science, E.Dickinson and M. Leser, RSC publishing (2006)

IN PREPARATION

1. N. Dorsaz, C. de Michele, F. Piazza, P. de Los Rios and G.Foffi, ***Crowding effects in diffusion limited reaction***, to be submitted
2. N. Dorsaz, G.Foffi et al., ***Phase coexistence of binary mixtures of eye lens proteins*** in preparation

ACADEMIC VISITS

- Prof. Kahl, Soft Matter Theory Group, ITP, Vienna University of Technology (Vienna, 30 Oct. - 5 Nov. 2008)
- Dr. De Michele, Group. Prof. Sciortino, Dipartimento di Fisica, Univ. La Sapienza (Roma, 28 May - 4 June 2007)

LANGUAGES

French	native
Italian	bilingual
English	fluent
German	high school level

COMPUTER SKILLS

- Languages: C, C++, Fortran
- Operating systems: Unix/Linux, Windows
- Software: Mathematica, Matlab